UNIVERSITÄT PADERBORN
Die Universität der Informationsgesellschaft

Faculty of Science
Department of Chemistry

Dissertation

Dr. rer. nat.

Studies of the adsorption of organic acids and nanoparticles on modified metal surfaces by means of the QCM technique

---

Author:

MSc. Agata Pomorska

Supervisor:

Prof. Dr. -Ing. Guido Grundmeier

June 12, 2013

Submitted: 12 April 2013

Defense: 29 May 2013

First Referee: Prof. Dr. -Ing. Guido Grundmeier

Second Referee: Prof. Dr. Claudia Schmidt

Commission Member: PD Dr. Hans Egold

Chairman: Prof. Dr. -Ing. Hans-Joachim Warnecke

Abstract

The main scope of this thesis is in-situ investigation of reaction mechanism at the liquid/solid interfaces, where self-organization of adsorbed species takes place, by means of Quartz Crystal Microbalance (QCM).

Polyelectrolyte covered TiO_2 nanocontainers (NCs) were adsorbed on functional thiol self-assembled monolayers on a quartz crystal gold electrode. Colloids self-location was strongly influenced by surface chemistry of particles and substrates as well as bulk conditions like pH and ionic strength. Electric Double Layer and Van der Waals interactions within the system are fundamental for NCs implementation into polymer coatings with perspective self-healing and anti-corrosion properties. The results were in agreement with DLVO theory.

Moreover, a new phenomenon of positive frequency shift was observed along adsorption of those particles. It could be explained by formation of a coupled resonator between NCs and a quartz crystal. Thus, QCM probed the contact strength, rather than the particle mass, when adsorbate agglomerates were larger than 1 μm.

Furthermore, QCM was employed to examine self-assembly of alkylphosphonic acids on nanorod and continuous nanocrystalline ZnO films. Proper functionalization is crucial for their performance and selectivity as biosensors and adhesion promoters on engineering metals. It is believed that phosphonic acid partially dissolves ZnO crystals. Released metal ions appeared to form complexes with organic molecules and cover substrate with adsorbate layer. The interfacial processes could be controlled via addition of metal ions into bulk solution, variation of molecules alkyl chain length as well as solvent polarity.

QCM data were verified by means of FT-IR spectroscopy, FE-SE microscopy and static water contact angle (WCA) measurements of quartz crystal electrode surfaces after in-situ experiments.

Overall results gave a deep insight into interfacial phenomena delivering requirements for the best performance of the used materials according to their application.

Zusammenfassung

Das Hauptziel dieser Arbeit ist die in-situ - Untersuchung von Reaktionsmechanismen der Adsorption von selbstorganisierten Spezies an füssig/ fest Grenzflächen mittels Quarzkristall-Mikrowägung (QCM). Es wurden polyelektrolytummantelte TiO_2 - Nanocontainer (NCs) auf die mit Thiol funktionalisierte selbstorganisierende Monoschicht (engl. Self-assembled monolayer, SAM) einer Quarzkristall-Goldelektrode adsorbiert. Die Kolloidverteilung wurde hierbei stark durch die Oberflächenchemie der Partikel und der Oberflächen, sowie durch die Eigenschaften des Bulks wie pH-Wert und Ionenstärke bestimmt. Die Wechselwirkungen zwischen der elektrischen Doppelschicht und Van-der-Waals-Kräften innerhalb dieses Systems sind grundlegende Bedingungen für die Implementation von NCs in Polymerbeschichtungen, welche hinsichtlich Selbstheilungs-und Anti-Korrosions-Eigenschaften von besonderer Bedeutung sind. Die Resultate stimmen hierbei gut mit der DLVO - Theorie überein. Ferner wurde hier zum ersten Mal eine positive Frequenzverschiebung während der Adsorption solcher Partikel beobachtet. Diese ist durch die Bildung eines gekoppelten Resonators zwischen den NCs und dem Quarzkristall zu erklären. Demnach erfasst die QCM bei Adsorbat-Agglomeraten größer als 1 μm vielmehr die Bindungsstärke als die Partikelmasse. Des Weiteren wurde die QCM zur Verfolgung der Selbstorganisation von Alkylphosphonsäuren auf Stäbchen oder auf kontinuierlichen, nanokristallinen ZnO-Schichten genutzt. Entscheidend für deren Anwendung und deren Selektivität als Biosensoren oder Haftvermittler technischer Metallwerkstoffe ist eine geeignete Funktionalisierung. Es wird angenommen, dass ZnO teilweise von der Phosphonsäure gelöst wird. Folglich bilden die freigesetzten Ionen Komplexe mit den organischen Molekülen, welche als Adsorbatschicht das Substrat bedecken. Dieser Grenzflächenprozess konnte auf verschiedene Weise gesteuert werden: durch Zugabe weiterer Metallionen in die Bulklösung, durch Variation der Alkylkettenlänge sowie durch die Polarität des Lösungsmittels. Die ermittelten Daten der QCM konnten überdies durch folgende Methoden verifiziert werden: FT-IR Spektroskopie, FE-SE-Mikroskopie und Messungen des statischen

Kontaktwinkels von Wasser (engl. Water contact angle, WCA) auf der Elektrodenoberfläche der Quarzkristalle nach den in-situ Experimenten. Die gewonnenen Ergebnisse liefern einen tiefen Einblick in die Grenzflächenthematik und geben Aufschluss über die nötigen Anforderungen, um die beste Leistung der untersuchten Materialien hinsichtlich deren Einsatzart zu erhalten.

Paderborn, 11 April 2013

Ich versichere, dass ich die Dissertation selbständig verfasst und alle benutzten Quellen und Hilfsmittel vollständig angegeben habe.

(*Agata Pomorska*)

Acknowledgement

This work was completed in the Faculty of Science, Chemical Engineering and Macromolecular Chemistry Division at the University of Paderborn.

First of all, I would like to express my special gratitude to Prof. Dr. Ing. Guido Grundmeier for his support, guidance and patience. During my doctoral studies I have had the opportunity to face challenges in experimental work and management of very fundamental European and rather applied industrial funded projects, that gave me a unique experience, crucial for my future career.

Prof. Dr. Claudia Schmidt is gratefully acknowledged for the detailed refereeing of my thesis.

My particular thanks go also to Prof. Dr. Diethelm Johannsmann for his invaluable help by Quartz Crystal Microbalance data evaluation as well as many practical advices.

Special appreciation goes to the whole AK Grundmeier group for cooperation and assistance on the daily basis. This collaboration led in many cases to long term friendships, that I cherish and appreciate.

Last but not least I would like to thank my Parents, my Family and Friends for constant encouragement and patience especially during the last phase of my Ph.D. time.

Contents

Chapter 1

Introduction

Modern surface coating technologies on engineering metals consist of complex and time consuming processes. Furthermore, the waste formation due to the use of non-environmentally friendly compounds should be avoided. Hence new strategies are needed to simplify and improve the anti-corrosion protection of the substrates.

In the frame of this work two approaches of solving the addressed issues were investigated: (i) development of organic polymer coating matrix with self- repair properties, (ii) surface pre-treatment to obtain excellent adhesion at the border between novel layer and engineering material via stabilisation of interface chemistry with self-assembled monolayer on homogeneous nanocrystalline zinc oxide thin films.

Environmentally friendly methods of anti-corrosion protection can be introduced on the level of organic coating matrix. It is designed to provide superior properties like self-healing and self-sealing [1, 2]. The simplest solution would be implementation of corrosion inhibitor and sealing agents directly into matrix. Unfortunately, these substances are known to decrease overall layer adhesion and deteriorate its barrier properties. Thus, they need to be segregated via encapsulation in small nanoreservoirs, distributed uniformly within polymer multilayers. Active agent release can be controlled via polyelectrolyte shell covering nanoparticles and the substance is spread only on demand, triggered by mechanical damage and pH rise due to corrosion.

Application of adhesion promoting and corrosion resistant monomolecular layers is a "green" solution for pre-treatment of metals for further anti-corrosion protection with organic coatings. Classical conversion treatment can be replaced by organic bi-functional monolayers adsorbed on oxide covered metal surfaces via self-assembly mechanism. Organo-phosphonates and -silanes have already been applied as environmentally friendly ultra-thin films on oxide/hydroxide covered aluminium alloys, zinc coated and bare steel surfaces [3–5]. These self-organised structures enable uniform surface functionalization leading to excellent coating adhesion. What is more, introduction of those monolayers on engineering metals covered with homogeneous ZnO nanocrystalline thin films ensures even better stability in comparison to porous oxide coating naturally formed on top of metal alloy surfaces.

Nanocontainers interactions with polymer matrix as well as with functionalised substrate are crucial for the development and performance of those layers. Compatibility among all components is necessary for a fast and successful coating deposition. Therefore, materials have to be specifically selected for each configuration of the used substances. A complex surface protection based on two presented approaches at the level of organic film matrix and coating/ substrate interface is able to deliver long term self-repair effect to metal engineering substrates without major impact on the environment.

Chapter 2

State of Research

In the scope of this dissertation, studies on the development of smart complex nanoparticle-polymer anti-corrosion coatings were conducted. Furthermore, experiments on functionalization via self assembled monolayers were performed on ZnO nanocrystalline films (used to homogenise and additionally protect surface of engineering materials for better adhesion of novel polymer layers). The research addresses the problem of simple, fast and "green" metal protection as an alternative to classical conversion methods. Experiments were designed according to two approaches, namely: nanoparticle-polyelectrolyte interactions within complex layer matrix as well as molecular organisation of polymer adhesion promoting molecules on nanocrystalline zinc oxide surfaces.

Thin polymer film with nanoparticles (NPs) embedded within organic matrix is a new complex material used for application specific tuning of surface properties. Particular features can be achieved by selection of NPs core, its functionalization and polymer type. Polymer-nanoparticle materials were used as electrochemical biosensors in medical diagnostic devices [6–8] or to build up a mechanically stable material for artificial human bone [9]. Interface forces between NPs and polymer multilayers are essential for performance of such materials. A complex layer made of polyelectrolytes and mesoporous nanoparticles can be used as anti-corrosion self-repair coating [1]. Embedded particles deliver self-healing and self-sealing properties

8

due to the loaded active agents like: corrosion inhibitors, sealing agents or lubricants. Polyelectrolyte shell around nanocontainers possesses controlled release feature triggered by local pH changes or mechanical stress. Tailored shell chemistry determines NPs compatibility with the coating matrix and proper choice of adhesion promoter ensures coating stability at the metallic surface [3–5]. The driving forces controlling the durability of such complex systems have mainly electrostatic origin [10]. The chemical variety of polymers enables tuning of the charge distribution within the nanoparticle/ organic matrix phase border. Charges are applied to the system via polar groups of polyelectrolytes. Screening effects of added salts are known to play the major role in controlling the conformation and internal interactions. Polymer adsorption is promoted by increasing the attractive energy between the charged monomers and the oppositely charged NPs. If those bonds are strong enough, particle agglomeration can be attenuated. Despite long-term research, there is no full understanding of the adsorption mechanism and distribution process of the nanocontainers within polymer matrix. Since these reactions determine the anti-corrosion properties and performance of the film, there is a clear need for studies involving both experimental and theoretical approaches. In-situ adsorption studies were conducted as a function of nanoparticles shell charge adjusted by pH and ionic strength on functionalised metal surfaces. Gold substrates were modified with self- assembled monolayers possessing the same head groups as the ones of matrix polyelectrolytes. The experiments were carried on by means of Quartz Crystal Microbalance (QCM). The basic task of the device is measuring frequency shift of a quartz resonator upon mass change. In order to solve the established problems (concerning NCs adsorption mechanism and distribution process within polymer matrix) advance QCM instrument was employed. It determines frequency shifts as well as energy dissipation on a number of various harmonics. Therefore, in-situ adsorption studies could be combined with detailed detection of adsorbate structural changes like particle agglomeration caused by alteration of liquid bulk conditions. The results were supported by subsequent substrate microscope examination and FT-IR spectroscopy. The ex-

perimental data were in agreement with DLVO theory giving the exact deposition mechanism and recipe for synthesis of the coatings.

In the second approach, functionalization of the nanocrystalline ZnO surface was achieved as environmentally friendly pre-treatment of engineering metals as well as for bio-sensing application. The ZnO nanocrystalline films have attracted much attention within the research community due to wide spectrum of possible functions as adhesion promoter, gas- and bio-sensors [11, 15, 155]. Those films homogenise engineering metal surfaces, since natural composition of substrate oxide layers depends on bulk metal alloy and oxide formation kinetics. Resulted heterogeneity (bimetallic and grains of different orientations) leads to lower surface stability [12]. Nanocrystalline films are inert in corrosive media [13] and therefore are a promising material for industrial application as well as for selective bio-sensing with increased active surface area [14]. Uniformity of a substrate surface chemistry is crucial for the adhesion and sensing ability since bonded and organised molecular layer improves durability at the metal oxide surface. ZnO forms highly anisotropic nanocrystals, such as nanorods (NR), as those species grow along the c-axis direction of the hexagonal wurtzite structure [15]. Tailoring the chemistry of the zinc oxide crystalline film surface can be achieved via bi-functional alkylmolecules [16]. This type of molecule contains two functional groups bonded to the ends of an alkylchain. One group provides strong adhesion by high affinity to the substrate, while the second one bonds to polymer coatings or tunes surface chemistry for perspective bio-sensing. The QCM set-up was further employed to investigate surface modification of ZnO nanocrystalline thin films via organic alkylphosphonic acids under various experimental conditions. The results were evaluated in terms of molecular alkyl chain length, solvent polarity and crystal morphology impact on kinetics of self-organisation at the phase border. Nanocrystalline surface seemed to be very sensitive to strong phosphonic acid functional group, which appeared to govern ZnO dissolution as well as Zn^{2+} ion complexation along deposition. As a result, a thick adsorbate layer was formed and substrate topography was visibly changed. The obtained data suggested that

assembly of homogeneous molecular films was possible under certain experimental conditions, which provided limited reactivity of phosphonic acidic group and proper interactions between hydrophobic chains. It could be deduced that non polar medium and employment of long alkyl chain molecules (more than 10 methyl groups) were the most appriopriate parameters.

QCM proved to be a versatile tool to investigate interface phenomena giving a deep insight into mechanism of polyelectrolyte covered nanoparticles adsorption on functionalised metal surfaces and self-organisation of alkyl phosphonic acids on nanocrystalline zinc oxide films.

Chapter 3

State of Literature / Theory

3.1 Fundamentals of QCM

3.1.1 Sauerbrey equation

3.1.1.1 Converse piezoeffect in quartz crystal QCM basics

Jacques and Pierre Curie discovered the piezoelectric effect in 1880. The word piezo-electric originates from the Greek word *piezein* ($\pi\iota\varepsilon\zeta\varepsilon\iota\nu$) which means 'to press'. Stress applied to certain faces of specific crystals (e.g. quartz, tourmaline) gives electrical potential across the material. Potential magnitude is proportional to the strain. Piezoelectric crystals are acentric which means that they crystallise in non-centrosymmetric space groups [17].If a force is applied across an appropriate direction, the resulting atomic displacement will give proportional change in the net dipole moment in the crystal lattice. The degree and direction of this change depends on the relative orientation of the dipoles and crystal faces.

Quartz Crystal Microbalance (QCM) [18] is a device based on the converse piezo-electric effect, where application of an alternating voltage across the crystal (via gold electrodes evaporated on both sides of the resonator) produces a mechanical movement (Fig. 3.1). The mechanical strain is correlated to the frequency of alternating field. A suitable frequency causes an oscillation of the material at its resonance fre-

quency. It is a natural frequency of vibration determined by the physical parameters of a vibrating object.
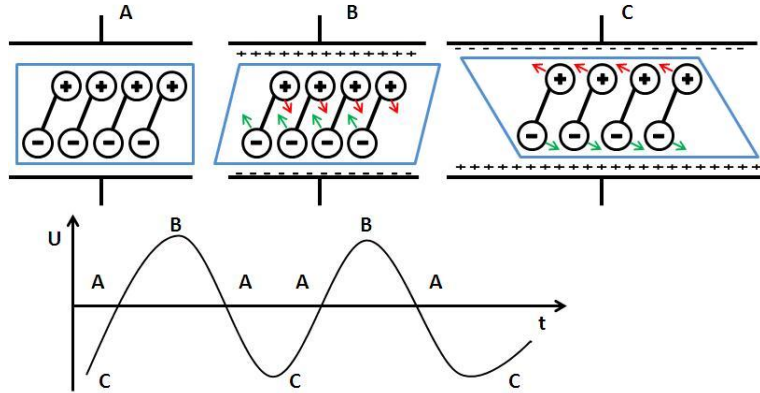

Figure 3.1: Thickness shear motion of AT-cut quartz crystal – results of an applied external alternating electrical field caused by an alternating voltage U variable with time t at electrodes on the crystal surface.

Application of an electric field across the crystal produces a shear strain proportional to the applied potential. In the case of quartz crystal this deformation is elastic. The opposite polarity forms an identical strain, but in the opposite direction. As the result an alternating potential across the crystal causes a vibrational motion in the quartz crystal with amplitude parallel to the surface of the crystal. That is why, the electromechanical coupling and resulting stresses depend on crystal symmetry, configuration and orientation of the electric field, as well as the on angle of crystal cut with respect to its crystallographic axes. Thus, only certain crystals exhibit shear displacements.

The quartz crystal is formed of nearly regular SiO_4 tetrahedral lattice with Si–O distances of 1.61 Å. The mode of vibration depends on the crystal cut. Cut: AT (35° off the y axis - Fig. 3.2) is highly sensitive to mass change as well as its vibration is stable at room temperature. It vibrates in the thickness shear mode.

A vibrating quartz crystal is an acoustic sensor. A shear standing wave is generated on the sample surface by application of an alternating current to the electrodes
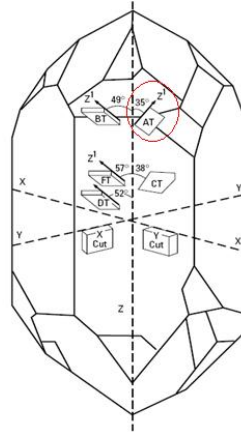
Figure 3.2: Quartz Crystal Cuts.

and crystals mechanical movement. The sensor probes the response of a thin layer to the mechanical displacement associated with an acoustic wave. The principle of acoustic measurements is that the propagation of the standing acoustic wave through the solid medium of the sensor is influenced by changes in the surrounding medium that contains the adsorbate of interest [19].

The crystal thickness (l_Q, including thin gold electrodes) equals one half of the acoustic wavelength (λ): $l_Q = \lambda/2$ (Fig. 3.3).
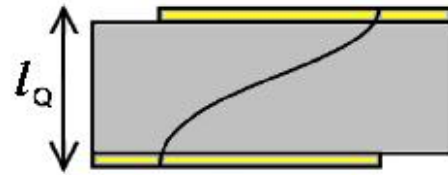
Figure 3.3: Resonance conditions: thickness of the resonator equals half of the wave.

The propagation velocity (v_Q) of the wave front in the quartz crystal has a known value of 3340 m/s. Its correlation with resonance frequency (f_0) is as follows:

$$v_Q = \lambda \times f_0 = 3340 \frac{\text{m}}{\text{s}} \,. \tag{3.1}$$

This gives:

$$f_0 = \frac{v_Q}{2 \times \rho_Q} \,, \qquad \rho_Q \text{ —quartz density} \,. \tag{3.2}$$

For a certain frequency there is a typical crystal thickness (Table 3.1). A 5 MHz quartz crystal is usually used in the QCM, since the ones with higher fundamental frequency are very thin and therefore very brittle.

l_Q /μm	f_0 /MHz
334	5
167	10

Table 3.1: Crystal thicknesses and corresponding resonance frequencies.

The resonance frequency is a function of the crystal thickness. The resonator can be made to oscillate at higher harmonics. The lowest one is called 'the fundamental' (resonance frequency). Harmonics and overtones are integer multiplies of a certain fundamental frequency. The term 'overtone' does not include the fundamental. Thus, the first overtone is the second harmonic. The fundamental and its odd harmonics are the most easily excited frequencies when piezo-electric plates are set into oscillation [20]. A resonance can be excited electrically, if there is a difference between the displacements of the two electrodes, which is a result of opposite charges at the two crystal surfaces [21].

3.1.1.2 Sauerbrey equation and assumptions for a perfect monolayer adsorption.

Sauerbrey recognized a very high sensitivity of the thickness-shear mode resonators to their mass change upon metal adsorption in 1959 [18]. The sensitivity is so high that even molecular monolayers can be easily detected. These thickness-shear mode resonators are used in QCM. Crystal vibration frequency decreases due to the additional mass load. The decrease of frequency is directly proportional to the mass change.

$$\Delta m = -\frac{\rho_Q \, l_Q}{f_0} \frac{\Delta f}{n} \tag{3.3}$$

Sauerbrey equation: where Δm is the mass change, Δf frequency change, f_0 is the resonant frequency, n the number of overtone, ρ_Q and l_Q are the specific density and thickness of the quartz crystal, respectively.

The QCM measures frequency change, not the mass change itself. Frequency shifts can be directly correlated to mass shift when [17, 22]:

- the adsorbate consists of a thin film, with a density similar to quartz,

- its mass does not exceed 2% of the resonators mass,

- it shifts the resonance frequency due to its inertia and moves synchronously with the oscillating surface of the device.

With those conditions, the added load slows down the oscillation, with the almost absolute value of the resonance frequency change, proportional to the adsorbed mass (3.3). What is more, the set-up respond does not depend on parameter sensitivity and frequency shift is the same on every harmonics.

Viscous fluids will not move synchronously with the oscillating device, due to the dissipation of the acoustic wave as it penetrates into the fluid layer [22]. A perfect 'Sauerbrey load' is homogeneous, rigidly coupled to the resonator and its outer interface is sharp. If any deviation from these conditions occurs, the adsorbed layer has viscoelastic properties.

3.1.2 Deviation from the Sauerbrey equation

In case of: soft media, rough objects or other nonlinear species, the basic QCM principle does not apply. Shifts in frequency can come about by various interactions with the sample, giving a non classical response of the QCM [22]. All these interaction can be monitored by passive determination of the resonance frequency by means of a network analyzer. In QCM, the crystal is made to oscillate via electricity (alternating voltage). Both the amplitude of oscillation and the current through the electrodes become large at the acoustic resonance frequency. The resonance can

therefore be found with electrical instrumentation as a sharp peak in the impedance spectra (Fig. 3.4). The network analyzer measures the electrical impedance of the device as a function of frequency. Such spectra can be fitted with resonance curves and two main parameters can be derivered.
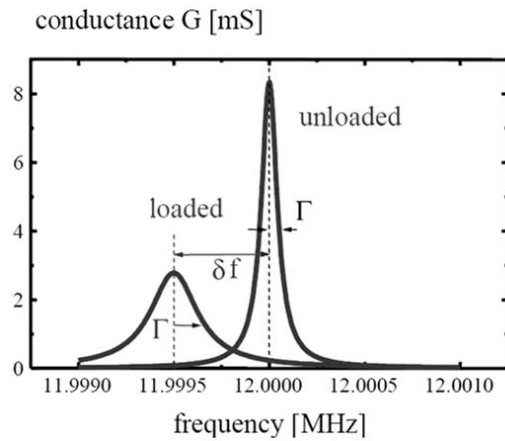

Figure 3.4: Quartz crystal impedance spectra with indicated.

The central parameters of the measurements are the resonance frequency (Δf – top of the peak) and the half band half width (the bandwidth, $\Delta\Gamma$ - half width of the peak at half height). Passive mapping of the resonance curves enables to compare data on numerous overtones, which is necessary by evaluating results (especially after experiments with large objects, e.g. colloids). A non-monolayer adsorption shift of parameters depends on overtone order [23, 24]. Moreover, quality of the crystals can be easily verified by the shape of the spectra. Another advantage of this method is the ability to monitor the second main derived parameter - the bandwidth or so called Energy Dissipation Factor ($\Delta\Gamma$). The shift in bandwidth is proportional to the amount of energy transferred from the crystal to the sample per unit time (converse of quality Q-factor). The dissipation factor (ΔD) is a measure of the extent of viscoelastic damping induced by the structural mobility of the particles coupled to the vibrating crystal. The damping is related to the interfacial particle conformation. When the dissipation increases, more energy is dissipated as particle

adsorption take place.

$$\Delta D = \frac{E_d}{f 2\pi E_s} \,,$$ (3.4)

where E_d is the energy dissipated during one oscillation and E_s is the energy stored in the oscillating system.

The bandwidth is used to quantify dissipation processes. The results are often displayed in terms of frequency and dissipation, D. The bandwidth is practically equal to dissipation:

$$D = \frac{2\Delta\Gamma}{f} \,.$$ (3.5)

$\Delta\Gamma$ carries essential information which can be used to determine viscoelastic properties [25]. Changes in the dissipation are related to the shear viscous losses induced by the adsorbed layers, and thus provide information that has the potential to identify structural differences between e.g. the same type of molecule during the adsorption process.

What is more, this parameter is less sensitive to temperature fluctuations and mechanical stress than the frequency and is often used by scientists to display their results. One has to remember that no significant energy dissipation occurs during monolayer adsorption on a flat substrate (no viscoelastic effects during the process).

3.1.2.1 Coupled-resonance model

An important benefit of the QCM is its simplicity in operation and data analysis. It is especially important by experiments with complex samples (such as colloids).

The crystal surface undergoes a tangential shear motion and the frequency shift is proportional to the area-averaged stress-speed ratio at the crystal surface despite of the sample complexity [22]. Sauerbrey equation including complex frequency shift can be written as follows:

$$\frac{\Delta f^*}{f_F} = -\frac{2f}{Z_q} m_f \,.$$ (3.6)

$\Delta f^* = \Delta f + i\Delta\Gamma$ is the complex frequency shift (Fig. 3.4), $\Delta\Gamma$ is the half bandwidth at half maximum, f_F is the frequency of the fundamental, f is the resonance

frequency, $Z_q = 8.8 \times 10^6$ kgm^{-2}s^{-1} is the acoustic impedance of AT-cut quartz, and m_f is the mass per unit area of the deposited material. For the Sauerbrey case, the frequency shift is purely real. There is no shift in the bandwidth.

The QCM easily reaches monolayer sensitivity because of the resonance sharpness. It can be seen in the impedance spectra as a high peak for certain overtone (the sharpness decreases with overtone order-more peaks in the spectra around higher overtones). However, monolayer sensitivity often is insufficient for studying the affinity of certain target molecules to particular surfaces. The coverage can be in the sub-monolayer regime due to low concentration of the adsorbate or the lateral density of receptors. Moreover, the initial binding kinetics may contain valuable information [26], hence sub-monolayer sensitivity is very important. The signal enhancement can be achieved via e.g. attachment of target molecules to larger objects (such as bulky molecules or small colloidal spheres), which are more likely to be detected than the target molecules itself [27]. This approach has been demonstrated to increase the signal observed for DNA hybridization using DNA-conjugated nanoparticles captured by surface-bound single-stranded templates.

During set of experiments with larger diameter particles (1 micron sized agglomerates of TiO$_2$ nanocontainer, covered with polyelectrolytes - SEM Fig. 3.5), positive frequency shifts upon adsorption were observed [23].

A positive Δf clearly is incompatible with the Sauerbrey equation. Within the Sauerbrey model, the mass of the composite resonator increases (by deposition of thin rigid films), thereby slowing down its movement. It is hard to understand how added mass can speed up the oscillation. As has been reported by Dybwad [28], the positive frequency shifts occur when the crystal is put into contact with a sufficiently large sphere. Such experiments have been carried out numerous times in the dry state [29, 30]. The frequency shift is positive because of the composite resonator effective stiffness increase, rather than its mass. If the sphere is connected to the crystal via a small bridge (a 'point contact') the forces exerted by the crystal do not actually move the sphere around in space. The sphere is 'clamped' by inertia.
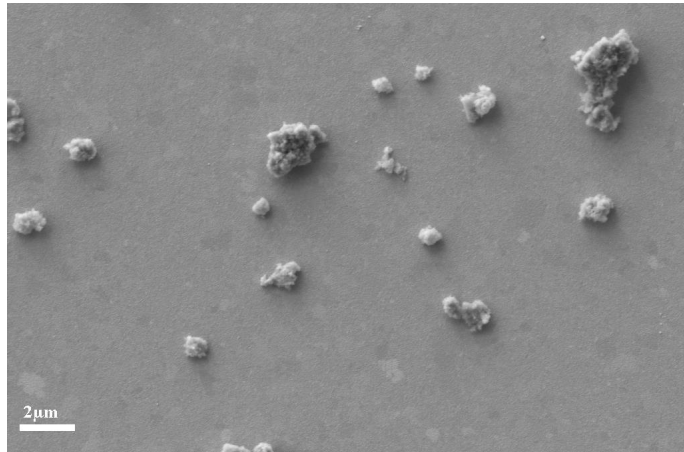
Figure 3.5: FE-SEM image of the colloidal aggregates used in the first set of experiments (Figs. 5.6). This specific sample consisted of PSS-terminated TiO_2 nanocontainers on a gold substrate functionalised with an aminothiol SAM.

However, since the sphere is connected to the crystal, it does exert a restoring force if the crystal is tangentially displaced. This restoring force adds to the internal stiffness of the crystal and thereby speeds up the oscillation.

Dybwad has put this model (termed 'coupled-resonance model') into quantitative terms [28]. It was concluded that the sphere in contact with the plate forms a second resonator with its own resonance frequency, ω_S. The sketch at the top of Fig. 3.6 shows the geometry and a mechanical representation. For a small mass tightly attached to the crystal, ω_S is much larger than the resonance frequency of the crystal, ω. Such a situation is, for instance, encountered with individual molecules physisorbed to the crystal surface. Further calculations have shown [23] that the Sauerbrey model applies as long as $\omega_S \gg \omega$. This situation is termed 'inertial loading' Δf is negative as long as the adsorbed objects are small enough. However, for large (micron-sized) spheres attached to the crystal via weak bridges, ω_S which is smaller than ω. In this limit, one arrives at a positive Δf, proportional to the stiffness of the contact and independent of the spheres mass. This situation is termed 'elastic loading'.
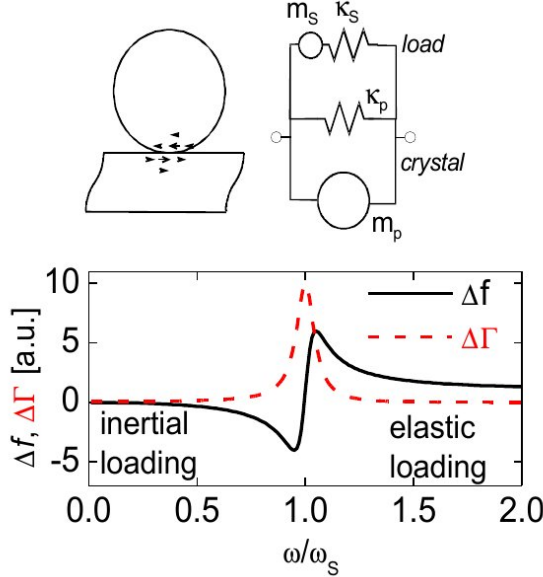
Figure 3.6: Top left: Sketch of a sphere adsorbed to the surface of a quartz crystal microbalance. Top right: Mechanical representation. The crystal and the sample form a system of coupled resonators with two resonance frequencies ω (crystal) and ω_S (sphere). The bottom plot shows the solution of Eq. (3.8).

More quantitatively, the coupled-resonance model predicts [28, 31]:

$$
\begin{aligned}
\frac{\Delta f + i\Delta\Gamma}{f_F} &= \frac{N_S m_S \omega}{\pi Z_q} \frac{\omega_S^2 + i\omega\gamma}{\omega^2 - \omega_S^2 - i\omega\gamma} = \frac{-N_S m_S \omega}{\pi Z_q} \frac{1}{1 - \frac{\omega^2}{\omega_S^2 + i\,\omega\gamma}} \\
&\approx \frac{-N_S m_S \omega}{\pi Z_q} \frac{1}{1 - \omega^2/\omega_S^2}.
\end{aligned}
\tag{3.7}
$$

N_S is the number density of the spheres. The resonance frequency of the sphere-plate system was also considered to be complex, where the imaginary part was termed $\omega\gamma$. γ quantifies dissipative components of the sphere-plate interaction. The bottom part of Fig. 3.6 shows the solution of the equation (3.8). Further insight is obtained from Taylor expansions for large and small ω. For $\omega \ll \omega_S$, one finds:

$$
\frac{\Delta f + i\Delta\Gamma}{f_F} \approx \frac{-N_S m_S \omega}{\pi Z_q} \frac{1}{1 - \omega^2/\omega_S^2} \approx \frac{-N_S m_S \omega}{\pi Z_q} = \frac{-2f N_S m_S}{Z_q}
\tag{3.8}
$$

that is the Sauerbrey equation with $N_S m_S$ inserted for the mass per unit area. In

the opposite limit of $\omega_S \ll \omega$, one finds:

$$\frac{\Delta f + i\Delta\Gamma}{f_F} \approx \frac{-N_S m_S \omega}{\pi Z_q} \frac{1}{1 - \omega^2/\omega_S^2} \approx \frac{N_S m_S \omega_S^2}{\pi Z_q \omega} = \frac{1}{\pi Z_q} \frac{N_S \kappa_S}{\omega} . \qquad (3.9)$$

The last identity on the right-hand side made use of $\omega_S = (\kappa_S/m_S)^{1/2}$, where κ_S is the stiffness of the sphere-plate contact. The frequency shift is positive, it is proportional to the stiffness, and it scales inversely with ω, that is, it scales inversely with overtone order n.

The above consideration applies to spheres in the dry state. Whether or not a similar situation can occur in liquids is not easily answered. Firstly, spheres in liquids are moved around by the liquid if they are located inside the evanescent acoustic wave. Secondly, the liquid in-between the sphere and the plate strongly contribute to the sphere-plate interaction, making any link rather strong. The liquid transports a substantial amount of stress across the gap both because of the high frequency. Viscous stress is proportional to the product of viscosity and frequency. Also there are gradients in hydrostatic pressure generated by the movement of the particles. Simple-minded diagrams such the one shown on the upper right in Fig. 3.6 do not apply in a liquid environment.

In the work [23] (Ch. 5.1), an example (1 micron sized agglomerates of TiO_2 nanocontainer, covered with polyelectrolytes) of positive frequency shifts occurring for colloidal adsorbates was reported. Finding of positive frequency shifts was surprising. In the experiment, an instrument which determines frequency shifts as well as bandwidths on a number of different overtones was employed in Sec. 5.1. For a simple Sauerbrey situation, positive Δf along the adsorption process is useless. However, for the question of whether or not the coupled-resonance model applies, the comparison of data from different harmonics is the key to the answer. The comparison shows that the coupled-resonance model can indeed explain the positive Δf.

3.2   Particle adsorption on surface

3.2.1   Particle-surface interactions

3.2.1.1   Interfacial forces

<u>Van der Waals forces:</u>

Van der Waals forces describe interactions between particles and surface. In the microscopic approach the potential energy between two molecules A and B (the minus arises since it is an attractive force) can be calculated as follows:

$$W_{AB} = -\frac{C_{AB}}{D^6} \; ,$$
(3.10)

where D is the distance between molecules and C_{AB} includes contributions of three dipole-dipole interactions:

A) Freely rotating dipoles influence position of surrounding molecules. The dipoles preferentially orient themselves with the opposite charges facing each other. The interactions between such two randomly orientated dipoles are referred as the Keesom energy:

$$W = -\frac{C_{\text{orient}}}{D^6} = -\frac{\mu_1^2 \mu_2^2}{3(4\pi\varepsilon_0)^2 k_B T D^6} \; .$$
(3.11)
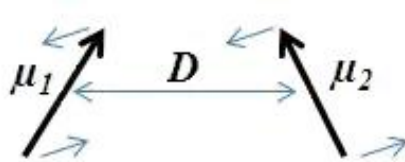
Figure 3.7: Interaction between two randomly orientated dipoles.

The equation gives Helmholtz free energy of interaction since it was derived under constant volume conditions. In this case, free energy is equal to internal. The ordering of one dipole by other ones field contributes to the free energy for the randomly oriented interactions between the dipoles. If one dipole approaches

another, half of the internal energy is taken up in decreasing the rotational freedom of the dipoles as they become progressively more aligned (decrease of entropy). That is why, the free energy W in the previous equation is only half of the internal energy.

In the case when a charge approaches a neutral molecule, attraction appears due to the induced dipole moment inside the molecule. An induced dipole arises, which interacts with the charge. The Helmholtz free energy equals:

$$W = -\frac{Q^2 \, \alpha}{2(4\pi\varepsilon_0)^2 \, D^4} \, , \tag{3.12}$$

were α is the polarizability in $C^2m^2J^{-1}$. The polarizability is defined by $\mu_{\text{ind}} = \alpha E$, where E is the electric field strength. Often it is given as $\alpha/4\pi\varepsilon_0$ in units of $Å^{-3}$.

B) When a molecule with a static moment interacts with a polarizable molecule it creates a system of randomly oriented induced dipoles. For such freely rotating dipoles the Helmholtz free energy is equal:

$$W = -\frac{C_{\text{ind}}}{D^6} = -\frac{\mu^2 \, \alpha}{(4\pi\varepsilon_0)^2 \, D^6} \, . \tag{3.13}$$

The interaction between two randomly oriented induced dipoles is called Debye interaction.

C) An attraction force exists also between two non-polar molecules. It is called London or dispersion force. In order to calculate it, quantum mechanical perturbation theory has to be applied. The origin of London force lies at atom level. Electrons circulate around nucleus with a high frequency (10^{15} - 10^{16} Hz). Therefore, atom has an instant polarity, which direction changes with a high frequency. Two such oscillators influence each other, when they are in a close distance. Attractive orientations are more probable then repulsive ones, thus average force between two molecules is attractive. The Helmholtz free energy with ionisation energies of $h\nu_1$ and $h\nu_2$ can be approximated for this case as follows:

$$W = -\frac{C_{\text{disp}}}{D^6} = -\frac{3}{2}\frac{\alpha_1\alpha_2}{(4\pi\varepsilon_0)^2 D^6}\frac{h\nu_1\nu_2}{(\nu_1 + \nu_2)} \, . \tag{3.14}$$

In the overall equation for the van der Waals force between macroscopic solids (3.15) C_{AB} is equal to C_{total} and sums up contributions of all three dipole-dipole

24

interactions:

$$C_{\text{total}} = C_{\text{orient}} + C_{\text{ind}} + D_{\text{disp}} . \tag{3.15}$$

They are given in units of 10^{-79} Jm^6. The van der Waals forces are a sum of Keesom, Debye and London forces. All three of them contain the same distance dependency: the potential energy decreases with $1/D^6$. The London dispersion term usually dominates.

Determination of the interactions between macroscopic solids requires calculations of van der Waals (vdW) energy between a molecule A and an infinitely extended body with a planar surface made of molecules B. VdW energy is summed up between molecule A and all molecules in the solid B via an integration of the molecular density ρ_B over the entire volume of solid:

$$W_{\frac{Mol}{plane}} = -C_{AB} \int \int \int \frac{\rho_B}{D^6} \, dV = -C_{AB}\rho_B \int_0^\infty \int_0^\infty \frac{2\pi \, r dr \, dx}{[(D+x)^2 + r^2]^3} . \tag{3.16}$$

To solve the equation the cylindrical coordinates (Fig. 3.8) were used and the constant density of molecules B was assumed. With $2r \, dr = d(r^2)$ the vdW energy between those to objects is equal:

$$W_{\frac{Mol}{plane}} = -\pi\rho_B C_{AB} \int_0^\infty \int_0^\infty \frac{d(r^2)}{[(D+x)^2 + r^2]^3} \, dx = \frac{\pi\rho_B C_{AB}}{6D^3} . \tag{3.17}$$
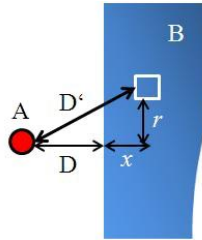

Figure 3.8: Calculation the vdW force between a macroscopic body and a molecule.

The energy between a molecule and a macroscopic body decreases less steeply than the energy among two molecules. The former interaction is proportional to

D^{-3} instead of the D^{-6}. VdW energy between two infinitely extended solids as well as between solids having different geometries can be calculated.

Previous equation can be used for the two infinitely extended solids which are separated by a parallel gap of thickness D with integration over all molecules in the solid A:

$$W = -\frac{\pi \rho_B C_{AB}}{6} \int \int \int \frac{\rho_A}{(D+x)^3} dV = -\frac{\pi \rho_B C_{AB}}{6} \int\limits_0^\infty \int\limits_{-\infty}^\infty \int\limits_{-\infty}^\infty \frac{\rho_A dz dy dx}{(D+x)^3} \ , \quad (3.18)$$

y and z are the coordinates parallel to the gap. The integral is infinite because the solids and infinitely large.

The vdW energy has to be divided by area:

$$\omega = \frac{W}{A} = -\frac{\pi \rho_A \rho_B C_{AB}}{6} \int\limits_0^\infty \frac{dx}{(D+x)^3} = -\frac{\pi \rho_A \rho_B \, C_{AB}}{12 D^2} \ . \quad (3.19)$$

With the definition of so called Hamaker constant:

$$A_H = \pi C_{AB} \, \rho_A \rho_B \ . \quad (3.20)$$

The vdW energy per area then is equal:

$$\omega = -\frac{A_H}{12 D^2} \ . \quad (3.21)$$

The force per area unit is equal to the negative derivative of ω versus distance:

$$f = -\frac{A_H}{6 \pi D^3} \ . \quad (3.22)$$

The vdW energy between solids with different geometries can be calculated in the same way. An important case is the interaction between two spheres with radii R_1 and R_2. The vdW energy is then equal [32]:

$$W = -\frac{A_H}{6} \left[\frac{2 R_1 R_2}{d^2 - (R_1 + R_2)^2} + \frac{2 R_1 R_2}{d^2 - (R_1 - R_2)^2} + \ln \left(\frac{d^2 - (R_1 + R_2)^2}{d^2 - (R_1 + R_2)^2} \right) \right] ,$$
$$(3.23)$$

where d is the distance between the centres of the spheres. The distance between the surfaces is $D = d - R_1 - R_2$.

In the last equation only attractive vdW forces were taken into account. The molecules repel each other since at very short range the electron orbitals start to overlap. Henderson considered this short range repulsion and modified the equation [33].

If the radii of the spheres are substantially larger than the distance ($D \ll R_1, R_2$) last equation can be simplified to:

$$W = -\frac{A_H}{6D} \frac{R_1 R_2}{R_1 - R_2} \ . \tag{3.24}$$

The vdW force is the negative derivative of W over D:

$$F = -\frac{A_H}{6D^2} \frac{R_1 R_2}{R_1 - R_2} \ . \tag{3.25}$$

For a sphere and a flat, planar surface the energy and force can be obtained by letting R_2 go to infinity:

$$W = -\frac{A_H R}{6D} \tag{3.26}$$

and

$$F = -\frac{A_H R}{6D^2} \ . \tag{3.27}$$

In the reality, interaction between any two molecules depends on the presence of a third one. Neighbouring molecules influence vdW forces inside a pair of molecules by e.g. changing their polarizability. Such a problem is avoided in the macroscopic theory developed by Lifshitz [34, 35]. The solids are treated as continuous materials with bulk properties (e.g. dielectric permittivity). Such a simplified way turns out to be sufficient in order to obtain e.g. correct distance dependencies. Only Hamaker constant is calculated in a different way.

Based on Lifshitz theory, further investigation of vdW interactions were performed in Refs. [36, 37]. In a macroscopic treatment, bulk properties like molecular polarizability and ionization frequency are replaced by the static and frequency dependent dielectric permittivity. The Hamaker constant is a sum over many frequencies, which can be converted into an integral. For a material 1 interacting with

material 2 in the environment of material 3, the non-retarded Hamaker [35] constant is:

$$A_H = \frac{3}{4}k_B T \left(\frac{\varepsilon_1 - \varepsilon_3}{\varepsilon_1 + \varepsilon_3}\right)\left(\frac{\varepsilon_2 - \varepsilon_3}{\varepsilon_2 + \varepsilon_3}\right) \tag{3.28}$$

$$+ \quad \frac{3h}{4\pi}\int\limits_{\nu_1}^{\infty}\left(\frac{\varepsilon_1(i\nu) - \varepsilon_3(i\nu)}{\varepsilon_1(i\nu) + \varepsilon_3(i\nu)}\right)\left(\frac{\varepsilon_2(i\nu) - \varepsilon_3(i\nu)}{\varepsilon_2(i\nu) + \varepsilon_3(i\nu)}\right)d\nu \ .$$

The first term contains the static dielectric permittivity of the three media: ε_1, ε_2 and ε_3. It represents the sum of Keesom and Debye energy. The term is especially significant when the third medium is water since water molecules have strong dipole moment. Usually the second term dominates. The dielectric permittivity is not constant but it depends on frequency of the electric field. The static dielectric permittivities are the values of this dielectric function at zero frequency. $\varepsilon_1(i\nu)$, $\varepsilon_2(i\nu)$ and $\varepsilon_3(i\nu)$) are the dielectric permittivities at imaginary frequencies $i\nu$, $\nu = 2\pi\,k_B T/h = 3.9\times 10^{13}$Hz at $T = 25^oC$. This corresponds to a wavelength of 760 nm (optical regime of the spectrum). The energy is in the order of electronic states of outer electrons. The dielectric properties of all three materials should be known in order to calculate the Hamaker constant. For frequencies in the visible range of spectrum the dielectric permittivity can be calculated as follows:

$$\varepsilon(i\nu) = 1 + \frac{n^2 - 1}{1 + \nu^2/\nu_e^2} \ , \tag{3.29}$$

where n is the refractive index, ν_e the mean ionization frequency of the material ($\sim 3\times 10^{15}$ Hz). If an assumption is taken, that all three materials are the same, the non-retarded Hamaker constant can be approximated as follows:

$$A_H \approx \frac{3}{4}k_B T \left(\frac{\varepsilon_1 - \varepsilon_3}{\varepsilon_1 + \varepsilon_3}\right)\left(\frac{\varepsilon_2 - \varepsilon_3}{\varepsilon_2 + \varepsilon_3}\right) \tag{3.30}$$

$$\cdot \quad \frac{3h\nu_e}{8\sqrt{2}}\frac{(n_1^2 - n_3^2)(n_2^2 - n_3^2)}{\sqrt{(n_1^2 + n_3^2)(n_2^2 + n_3^2)}\left(\sqrt{n_1^2 + n_3^2} + \sqrt{n_2^2 + n_3^2}\right)} \ .$$

Here, frequencies in the visible or UV spectrum contribute the most to the Hamaker constant. Factors: $n_{1,2,3}$ are the refractive indexes of the materials.

Hamaker constant easily allows prediction of interactions (attraction, repulsion) between material 1 and 2 in the environment of 3. An attractive vdW force corresponds to positive sign of the Hamaker constant, negative sign to the repulsive force. VdW forces are attractive between similar materials (for $\varepsilon_1 = \varepsilon_2$ and $n_1 = n_2$, $A_H > 0$). If two different substances are in vacuum ($\varepsilon_3 = n_3 = 1$) or a gas, the vdW force is also attractive. The interactions can be repulsive in a condensed medium. Moreover, A_H is negative when material 1 interacts stronger with material 3 then with medium 2. Repulsive vdW forces can also occur across thin films on solid surfaces. Repulsive force between a solid particle and an air bubble in water is used in the flotation. In this process air bubbles extract minerals from aqueous dispersion.

The previous analysis applies to insulating materials. The dielectric constant is infinitive for electrically conductive materials and the last equation does not apply. In such a case the dielectric permittivity has to approximate:

$$\varepsilon(i\,\nu) = 1 + \frac{\nu_e^2}{\nu^2} \, , \tag{3.31}$$

where ν_e is the plasma frequency of electron gas that equals around 5×10^{15} Hz. Inserting the last equation to Eq. (3.29) leads to the approximate Hamaker constant of 4×10^{-19} J for metals interacting across a vacuum. That is why, A_H of metals and metal oxides can be higher of up to an order of magnitude then those of non-conductive media.

The most popular bulk material 3 is water that is why the effect of dissolved ions has to be considered. Ions slow down the water molecules in their hydration shell from orienting in an external electric field and first term in the equation for the Hamaker constant is affected. Moreover, the salt concentration can be much higher on surfaces than in the bulk phase, so that the dielectric constant can be higher in the bulk phase.

From Eq. (3.29) a useful approximation can be derived:

$$A_{123} \approx \sqrt{A_{131} \times A_{232}} \, . \tag{3.32}$$

If the Hamaker constant of material 1 interacting across medium 3 with itself A_{131} and the Hamaker constant of material 2 interacting across medium 3 with itself A_{232} are known, then A_H for the interaction between material 1 with material 2 across medium 3, A_{132} can be estimated.

Electric Double Layer Forces:

Water is a good solvent for ions due to its high dielectric constant. Therefore, most of the surfaces bear an electric charge in aqueous environment. Adsorption or desorption of ions from a surface leads to charging. This surface charge creates an electric field, which attracts counter ions. The layer of surface charges and counter ions is called Electric Double Layer (EDL). Its theoretical most common used structure was described by Otto Stern (Figs. 3.9, 3.10). He based his idea on previous EDL models, proposed by: Herman von Helmholtz, Louis George Gouy and David Chapman. The combined Gouy-Chapman-Stern model divides EDL into two parts: an inner part - the Stern layer, and outer part, the Gouy diffuse layer. The immobile inner layer consists of ions which are directly adsorbed to the surface, whereas the second one includes mobile ions that obey Poisson-Boltzmann statistic. Potential between static and mobile layers is called the zeta-potential. What is more, a third so called outer Helmholtz plane separates inner and outer layer. The outer Helmholtz plane (OHP) is formed by counter ions with their hydration shells. The ions which are specifically adsorbed to the surface (with no hydration layer in between) determine the inner Helmholtz plane (IHP) [38].

Energy of EDL has a crucial importance in colloid science. In most application Gibbs free energy of diffuse layer is relevant. In order to calculate the chemical energy, one has to consider that the dissociation or binding of ions does not last forever, since the larger amount of dissociated ions the higher the electric potential. This potential prevents further ions from dissociation. The process stops when the chemical energy is equal to the electrostatic energy.

The electrostatic energy of one ion with Q charge equals: $Q\Psi_0$, where Ψ_0' is the
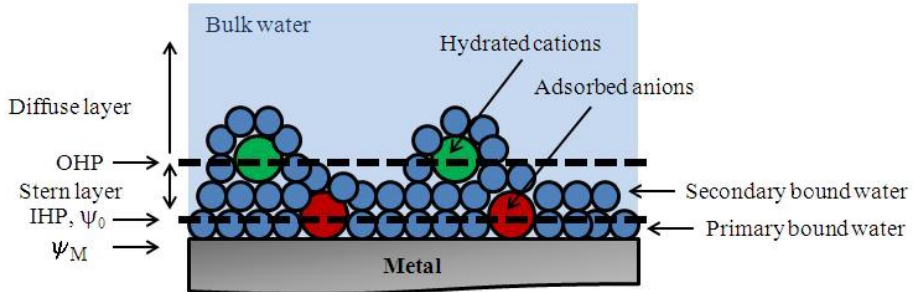
Figure 3.9: Schematic representation of EDL structure on metal in aqueous medium.
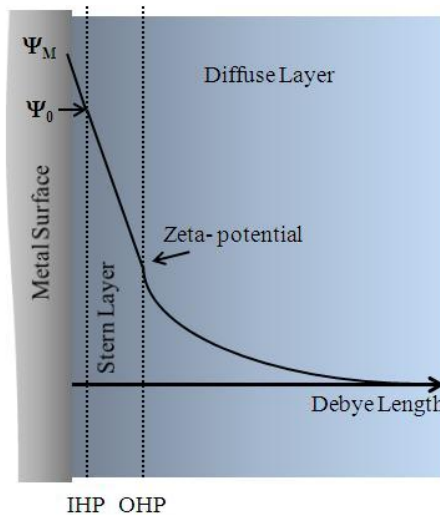
Figure 3.10: Schematic representation of EDL surface potential as a function of the distance.

surface potential at a certain time of charging-discharging process. The chemical energy of this ion is: $-Q\Psi_0$ (Fig. 3.10). That is why, the Gibbs free energy per unit area for the formation of an EDL is: $-\sigma\Psi_0$. Secondly, the counter ions should go directly to the surface at $x = 0$. The number of counter ions is equal to number of ions in the diffuse double layer. At the beginning of EDL formation, counter ions are attracted by the full surface potential. Thereafter, their presence reduces the surface potential and the following counterions are attracted by smaller potential. The work $dG = \Psi_0' d\sigma$ has to be performed in order to bring counterions to the

surface. The total gained energy (lost by EDL) is:

$$W_{\text{EDL}} = \int\limits_0^\sigma \Psi_0' \, d\sigma' \qquad (3.33)$$

In the third step of calculating the Gibbs free energy of EDL is releasing the counterions from the surface. Their motion is simulated by thermal fluctuations. The entropy and energy increase. These both terms compensate, that is why no contribution to the Gibbs free energy results from the third step.

The Gibbs free energy of an EDL is negative since it is formed spontaneously. It increases roughly in proportion to the square of the surface potential. For low potentials a simpler relation can be used:

$$g = -\kappa\varepsilon\varepsilon_0 \cdot \int\limits_0^{\Psi_0} \Psi_0' \, d\Psi_0' = -\frac{\kappa\varepsilon\varepsilon_0}{2}\,\Psi_0^2 = -\frac{1}{2}\,\sigma\,\Psi_0 \; . \qquad (3.34)$$

Poisson-Boltzmann Theory:

In general the electric potential Ψ near a charged planar interface depends on the distance x normal to the surface. Therefore, a following assumption is made in calculations: surface is solid and planar with homogeneously distributed electric surface charge density σ, which is in contact with a liquid. Charge of such a surface generates a surface potential of: $\Psi_0 = \Psi(x = 0)$.

The charge density and electric potential are related by the Poisson equation:

$$\nabla^2\Psi = \frac{\partial^2\Psi}{\partial x^2} + \frac{\partial^2\Psi}{\partial y^2} + \frac{\partial^2\Psi}{\partial z^2} = -\frac{\rho_e}{\varepsilon\varepsilon_0} \; , \qquad (3.35)$$

where, ρ_e is the local electric density in C/m^3. The potential distribution can be calculated with the Poisson equation, when the exact distribution is known. Ions are free to move in a solution. That is why, their distribution needs to be included to the Poisson equation via Boltzmann statistic. Equation for the local ion density is given by Boltzmann statistic:

$$c_i = c_i^0 \cdot e^{-\frac{W_i}{k_B T}} \; , \qquad (3.36)$$

where, W_i is the work required to bring an ion in a solution from infinite distance to a certain position closer to the surface. This equation gives information about the correlation between local ion concentration c_i of the ith species and electric potential at a certain position. If the potential at a certain position in a solution is positive, the possibility of finding an anion at this position is increased, while the cation concentration is decreased.

For further calculations of electric potential near a charged planar surface a following assumption must be taken: only electric work has to be done (work needed to displace other molecules is neglected). Moreover, it is assumed that only 1:1 salt is dissolved in the liquid. The electric work required for localising a charged cation in a place with potential Ψ equals: $W^+ = e\Psi$. In case of localising an anion it is: $W^- = -e\Psi$. The local cation and anion concentration c^+ and c^- are related with the local potential Ψ by Boltzmann factor:

$$c^+ = c_0 \cdot \exp\left(-\frac{e\Psi}{k_B T}\right) \;, \qquad c^- = c_0 \cdot \exp\left(+\frac{e\Psi}{k_B T}\right) \;, \qquad (3.37)$$

where c_0 is the bulk concentration of salt. The local charge density is equal:

$$\rho_e = e\left(c^+ - c^-\right) = e\,c_0 \cdot \left[\exp\left(-\frac{e\Psi}{k_B T}\right) - \exp\left(+\frac{e\Psi}{k_B T}\right)\right] . \qquad (3.38)$$

In the equation it is indicated that the potential Ψ depends on the position. Substituting the charge density into Poisson equation one obtains

$$\nabla^2 \Psi = \frac{ec_0}{\varepsilon\varepsilon_0} \cdot \left[\exp\left(+\frac{e\Psi}{k_B T}\right) - \exp\left(-\frac{e\Psi}{k_B T}\right)\right] . \qquad (3.39)$$

This equation is referred to as the Poisson-Boltzmann equation.

Planar surfaces:

Potential of planar infinitely extended surface Ψ cannot change in y and z directions. That is why the Poisson-Boltzmann equation in this case is:

$$\nabla^2 \Psi = \frac{e\,c_0}{\varepsilon\varepsilon_0} \cdot \left[\exp\left(+\frac{e\Psi(x)}{k_B T}\right) - \exp\left(-\frac{e\Psi(x)}{k_B T}\right)\right] . \qquad (3.40)$$

For low potentials ($e|\Psi| \ll k_B T$, at room T: $\Psi \leq 25$ mV) the exponential function can be expand into a series and just the first, linear term can be taken for further

calculations:

$$\nabla^2 \Psi = \frac{ec_0}{\varepsilon\varepsilon_0} \cdot \left(1 + \frac{e\Psi(x)}{k_B T} + \ldots - 1 + \frac{e\Psi(x)}{k_B T} + \ldots \right) = \frac{2c_0\,e^2}{\varepsilon\varepsilon_0\,k_B T} \Psi \,. \qquad (3.41)$$

Derivered equation is called the linearised Poisson-Boltzmann equation and its general solution is:

$$\Psi(x) = C_1 e^{-\kappa x} + C_2 e^{\kappa x} \,, \qquad (3.42)$$

where, κ stands for:

$$\kappa = \sqrt{\frac{2c_0 e^2}{\varepsilon\varepsilon_0\,k_B T}} \,. \qquad (3.43)$$

The boundary conditions define constants C_1 and C_2. These conditions require that the potential is equal to the surface potential at the surface ($\Psi(x = 0) = \Psi_0$) and Ψ disappears at the large distances from the surface: $\Psi(x \to \infty) = 0$.

The second boundary condition states that the potential becomes zero at very large distances. Such a statement gives directly $C_2 = 0$. $C_1 = \Psi_0$ due to the first boundary condition. Thus, the potential in general equals:

$$\Psi(x) = \Psi_0 \cdot e^{-\kappa x} \,. \qquad (3.44)$$

The potential decreases exponentially. The decay is given by $\lambda_D = \kappa^{-1}$ and it is called the Debye length. It decreases with increasing salt concentration, since the more ions are in a solution, the more effective is the screening of the surface charge. For a monovalent salt in water at T=25°C, the Debye length is equal:

$$\lambda_D = \frac{3.04 \text{ Å}}{\sqrt{c_0 \frac{\text{L}}{\text{mol}}}} \,. \qquad (3.45)$$

λ_D cannot be longer then 680 nm in water. The ion concentration cannot decrease below 2×10^{-7} mol/L due to the dissociation of water ($2H_2O \longrightarrow H_3O^+ + OH^-$). In reality, λ_D equals few 100 nm even in distilled water because of ionic impurities or a pH$\neq$7.

The Graham Equation:

Correlation between σ and Ψ_0 was derivered by Graham based on Gouy-Chapman theory. Electro neutrality condition requires that the total charge (sum of surface

charge and charge of ions in the whole EDL) must be equal zero. The total charge in the EDL is $\int_0^\infty \rho_e dx$, therefore:

$$\sigma = -\int_0^\infty \rho_e dx \,. \tag{3.46}$$

For one-dimensional Poisson equation and the boundary conditions: potential and its gradient at large distance are equal zero:

$$\sigma = \varepsilon\varepsilon_0 \int_0^\infty \nabla^2 \Psi dx = -\varepsilon\varepsilon_0 \frac{d\Psi}{dx}\big|_{x=0} \,. \tag{3.47}$$

With $dy/dx = -2\kappa \sinh(y/2)$ and:

$$\frac{dy}{dx} = \frac{d}{dx}\left(\frac{e\,\Psi}{k_B T}\right) = \frac{e}{k_B T} \cdot \frac{d\Psi}{dx} \,. \tag{3.48}$$

The Graham equation can be derivered:

$$\sigma = \sqrt{8c_0\,\varepsilon\varepsilon_0\,k_B T} \cdot \sinh\left(\frac{e\,\Psi}{2k_B T}\right) \,. \tag{3.49}$$

For low potentials a simplified relationship can be used:

$$\sigma = \frac{\varepsilon\varepsilon_0\,\Psi_0}{\lambda_D} \,. \tag{3.50}$$

The EDL capacity:

Capacitance of a plate capacitor is equal: $\varepsilon\varepsilon_0 A/d$, where A is the cross-sectional area and d is the separation distance between the two plates. In case of EDL, the capacitance is calculated in the Gouy-Chapman model:

$$C_{GC}^A = \frac{\varepsilon\varepsilon_0}{\lambda_D} \,. \tag{3.51}$$

EDL behaves like a plate capacitor, where the distance between the plates is given by the Debye length. The EDL capacity, so the ability to store a charge, rises with increasing salt concentration since λ_D decreases in such situation.

EDL Forces:

EDL of various particles or surfaces overlaps when they approach to each other. Formed force is called double layer force. It occurs naturally and is important e.g. in stabilisation of dispersions or emulsions.

In order to derive general equations to describe such force the Gibbs free energy per unit area ($w(x)$) has to be calculated. It can be done via calculating the change in $w(x)$ of two EDLs during the approach (A), or by determination of disjoining pressure in the gap (B). Both approaches give the same result.

(A) In the first method $w(x)$ for two approaching EDLs is calculated. The Gibbs free energy of one isolated EDL per unit area is:

$$g = - \int_0^{\Psi_0} \sigma' d\Psi_0' \,. \tag{3.52}$$

In case of two homogeneous EDLs, which are infinitely separated, the $w(x)$ is twice this value:

$$g^\infty = -2 \int_0^{\Psi_0} \sigma' d\Psi_0' \,. \tag{3.53}$$

If the distance between those two surfaces decreases up to x, the Gibbs free energy changes as well. Surface charge and potential depend on the distance:

$$g(x) = -2 \int_0^{\Psi_0(x)} \sigma'(x) d\Psi_0' \,. \tag{3.54}$$

The Gibbs free interaction energy per unit area can be presented as:

$$w(x) = \Delta g = g(x) - g^\infty \,. \tag{3.55}$$

Whereas the force per unit area is equal:

$$\Pi = -\frac{d\Delta g}{dx} \,. \tag{3.56}$$

According to these equations a following scenario of how two surfaces (with constant potential) interact with each other when they are brought closer can be derivered. Surface charge is related to surface potential by:

$$\sigma = -\varepsilon\varepsilon_0 \frac{d\Psi}{d\xi}\big|_{\xi=0} \,. \tag{3.57}$$

Every inconstant surface charge is equal to the potential gradient at the surface: $|d\Psi/d\xi|$.

The potential gradient decreases when two surface approach each other and the surface charge density decreases accordingly. Such reduction of the surface charge increases Gibbs free energy of molecules on the surface in order to form an EDL. This phenomenon leads to repulsion of those surfaces.
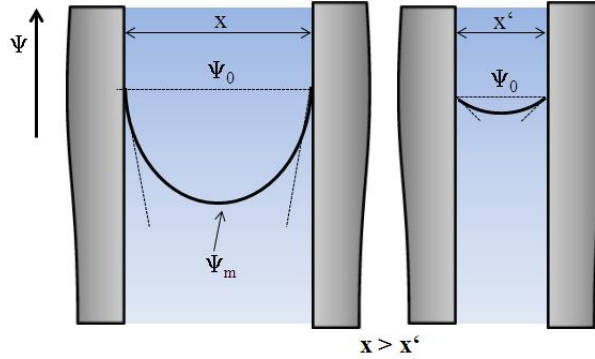

Figure 3.11: Potential gradient between two approaching surfaces. Symbols: at a given gap thickness x, the potential changes with ξ. D is the distance between finite, macroscopic bodies.

(B) The second method to describe change in Gibbs free energy is calculation of disjoining pressure, using Poisson-Boltzmann theory:

$$w(x) = -\int_{\infty}^{x} \Pi(x')\,dx'\,. \tag{3.58}$$

In case on low potential (linear dependence) and monovalent salt, the one-dimensional Poisson-Boltzmann equation is:

$$e\,c_0 \left[\exp\left(\frac{e\Psi}{k_B T}\right) - \exp\left(-\frac{e\Psi}{k_B T}\right) \right] - \varepsilon\varepsilon_0 \frac{d^2\Psi}{dx^2} = 0\,. \tag{3.59}$$

Integration leads to:

$$c_0\,k_B T \left[\exp\left(\frac{e\Psi}{k_B T}\right) + \exp\left(-\frac{e\Psi}{k_B T}\right) \right] - \frac{\varepsilon\varepsilon_0}{2} \left(\frac{d\Psi}{dx}\right)^2 = P\,. \tag{3.60}$$

The integration constant P has a physical meaning. It states for the pressure in the gap between two surfaces. The first term of the equation describes the osmotic

pressure, which is created due to the presence of increased number of ions in the gap. The second term (Maxwell stress term) refers to electrostatic force caused by interactions between two electric fields of neighbouring surfaces.

In order to obtain the disjoining pressure we have to put into contact the infinitely extended gap with an infinitely large reservoir. Only the difference of the pressure between the gap interior and the reservoir is effective since the force per unit area is Π. That is why, the osmotic pressure in the reservoir: $2k_B T c_0$ must be subtracted from P to get the disjoining pressure: $\Pi = P - 2k_B T c_0$.

By means of Poisson-Boltzmann equation with boundary conditions (of constant potential and constant charge) one can calculate potential distribution in the gap. These boundary conditions lead to identical force in case of a gap, larger than Debye thickness ($x \gg \lambda_D$). At small distances constant charge density cause more repulsive forces than the constant potential conditions [39].

In case of two identical surfaces, the surface potential is of course equal. The potential decreases in between them (Fig. 3.11). The gradient in the middle must be zero since the symmetry: $d\Psi(\xi = x/2)/d\xi = 0$. That is why, the osmotic pressure gives the disjoining pressure in the centre. The osmotic pressure rises towards the two surfaces. This increase is compensated by decrease in the Maxwell stress term, because the pressure must be everywhere the same in equilibrium:

$$\Pi(x) = c_0 \, k_B T \left[\exp \left(\frac{e\Psi_m}{k_B T} \right) + \exp \left(-\frac{e\Psi_m}{k_B T} \right) - 2 \right], \qquad (3.61)$$

where Ψ_m is the electric potential in the middle.

Π depends on the gap thickness, since Ψ_m changes with x. That is why the force can be determined by the potential in the middle. For low potentials this expression can be simplified. When the exponential functions are written in a series, all the terms higher that the quadratic can be neglected and at the end force per unit area for low potential is equal:

$$\Pi = \frac{\varepsilon \varepsilon_0}{\lambda_D} \cdot \Psi_m^2 . \qquad (3.62)$$

In order to determine Ψ_m a following assumption can be made: if the EDLs of two

neighbouring surfaces overlap only slightly (because of a large distance: $x \gg \lambda_D$), Ψ_m equals:

$$\Psi_m = 2\Psi'\left(\frac{x}{2}\right), \qquad (3.63)$$

where Ψ' is the potential of an isolated EDL. Various exact functions can be used for Ψ'.

For low potentials: $\Psi(\xi) = \Psi_0 \exp(-\xi/\lambda_D)$ it leads to a repulsive force per area of:

$$\Pi(x) = \frac{\varepsilon\varepsilon_0}{\lambda_D^2} \cdot \Psi_0^2 \cdot e^{-x/\lambda_D}. \qquad (3.64)$$

In order to calculate the Gibbs free interaction energy per unit area an integration is necessary:

$$w(x) = -\int_\infty^x \Pi(x')\,dx' = -\frac{2\varepsilon\varepsilon_0\,\Psi_0^2}{\lambda_D^2}\int_\infty^x e^{-x'/\lambda_D}\,dx' = \frac{2\varepsilon\varepsilon_0\,\Psi_0^2}{\lambda_D}e^{-x/\lambda_D}. \qquad (3.65)$$

3.2.1.2 DLVO theory

The first comprehensive model framework for the stability of colloidal dispersion was given by the linear combination of the dispersion force contribution and electrostatic repulsion to the pair potential. The work was done by Derjaguin and Landau [40] as well as independently by Verwey and Overbeek [41]. The theories were put together into one, named after the four authors: DLVO.

The total interaction energy between two objects is a sum of van der Waals-attractive and electrostatic-double layer repulsive forces: $V_T = V_A + V_R$. Since V_A and V_R have different dependencies on particle separation, the combined curve has a complicated structure (a typical example graph on the Fig. 3.12).

The general features of such curve are as follows [42]:

1) Primary minimum (V_{pmin}) - the attractive interactions are much larger than the repulsive term. The molecular structures of surface and adsorbed ions have scale similar to their separation. VdW force between identical media is always attractive despite of the medium in the gap.

2) The primary maximum (V_{max}) - is observable at slightly large distances, where
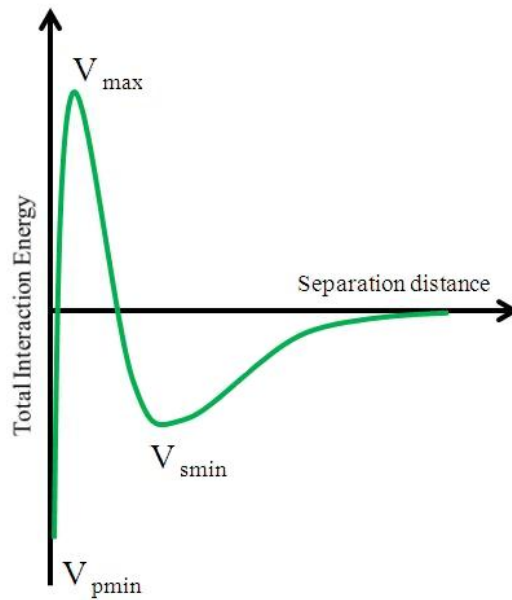
Figure 3.12: Interaction energy between a sphere and a surface, as a function of the distance.

the electrostatic interactions are dominant.

3) Thereafter, the total interaction energy decreases to the secondary minimum (V_{smin}), since the attractive interactions become again slightly larger than the repulsive one. It can lead to a weak, reversible coagulation without leading to direct molecular contact between the particles. It indicates the perfect energy level for particles inside an emulsion.

The aggregated state has the lowest energy condition as indicated by the primary minimum. That is why, it is a favourable position for the particles to reside. The primary maximum opposes colloids to approach and it creates an energy barrier that must be exceeded for aggregation to occur.

The thermal energy governs the particle motion, thus the energy distribution can be described by the Boltzmann equation. The rate of aggregation is proportional to $\exp(-V_T/k_BT)$. The particles will be in a colloidally stable state for $V_T \gg k_BT$. In case of strong attraction: $-V_T \gg k_BT$, strong aggregation of the particles occurs.

Summing up vdW forces promote coagulation whereas EDL forces stabilise dis-

persions. The energy per area between two infinitely extended solids (x - separation gap) can be approximated as follows:

$$w(x) = 64\, c_0\, k_B T\, \lambda_D \cdot \left[\frac{\exp\left(\frac{e\Psi_0}{2k_B T}\right) - 1}{\exp\left(\frac{e\Psi_0}{2k_B T}\right) + 1} \right]^2 \cdot e^{-x/\lambda_D} - \frac{A_h}{12\pi x^2}\,. \qquad (3.66)$$

Previously described regimes (V_{pmin}, V_{max}, V_{smin}) are more or less pronounced (and sometimes completely gone) at different salt concentration. The repulsive electrostatic energy barrier prevents particle aggregation at low ionic strength. In these conditions particles cannot gain enough energy to overcome it. Whereas, attractive vdW forces considerably reduce the energy barrier at high salt concentration and precipitation occurs. Moreover, the surface potential decreases with increasing ionic strength, causing the phenomenon to be even stronger.

3.2.1.3 Beyond DLVO theory

Understanding and prediction of the interaction force between colloidal particles is one of the most important problems in colloidal science. Four types of forces can be distinguished [43]: van der Waals forces, double layer repulsion forces, solvation (or adsorption) forces and steric forces due to adsorbed polymers. Continuum theories such as vdW and EDL fail at the surface separation close to molecular dimensions, where exactly the discrete molecular nature of the molecules has to be considered. **A)** Solvation forces are still not very well understood because of solvent adsorption onto colloidal particles. In is known that liquid structure at the interface is often different from the bulk. Some forces measurements [43] in polymer free system revealed that there are forces other then EDL and vdW operating at small surface to surface separation.

Solvation forces depend not only on the properties of the surrounding medium but also on the chemical and physical properties of the surfaces. The solvation or structuring of the solvent molecules at a surface is determined mostly by the geometry of molecules and by their self-organisation around a constraining boundary.

A solvation force arises once a change in the liquid density occurs at the surfaces of two approaching particles or larger solids (Fig. 3.13). The solvent density profile (normal to a solid surface) oscillates the bulk density with a periodicity of about one molecular diameter. Molecules are ordered in layers in this range. These layers are squeezed out of the closing gap (during approaching of those surfaces). Density fluctuations and specific interactions cause an exponentially decaying periodic force. The periodic length indicates the molecular layer thickness. Such forces were named solvation forces due to their origin which is adsorption of solvent molecules to solid surface [44].
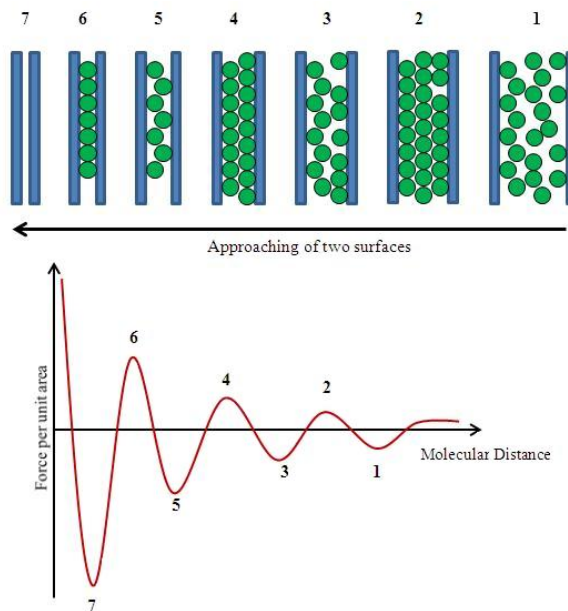
Figure 3.13: Solvation forces as a function of the distance between two surfaces.

Solvation forces are often described by an exponentially decaying cosine function:

$$f(x) = f_0 \cos\left(\frac{2\pi x}{d_0}\right) \cdot e^{-\frac{x}{x_0}}, \tag{3.67}$$

where, f is the force per unit area, f_0 is the force extrapolated to $x = 0$, d_0 states for the layer thickness, (equal to molecular diameter in case of simple liquids), and x_0 is the characteristic decay length.

B) Steric force is the main interaction in dispersions, where the system is stabilised by polymers. These forces are mainly determined by two factors: quality of the solvent (a good one should bring on repulsive interaction and cause polymer to remain in a solution rather than on the surface) as well as amount and structure of polymer on the surface.

These forces are very difficult to describe. Various components contribute to the force and dominate the total force depending upon the situation. Repulsive and entropic ones are the most important relations. The origins are as follows: the reduced configuration entropy of polymer chains, the thermal movement of a polymer chain at the surface (limited by the approach of another surface) causing the individual polymer chain entropy to decrease.

A simple model of polymer 'ideal freely joined segment chain' is needed for further description of such forces. Here, the polymer consists of a chain with n links (so called 'subunit', Fig. 3.14). Each of such subunit has a length of l (it corresponds to the monomer length, but it can be shorter or longer). The angle between neighbouring chain links is assumed as random.
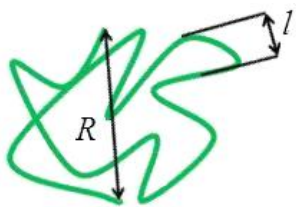
Figure 3.14: Polyelectrolyte coil.

A random coil is made of a chain. In order to characterise the size and volume of such coil, the mean square of the end to end distance $\overline{R^2}$ has to be established. The size of polymer (the square-root of this value) is given by:

$$R_0 = \sqrt{\overline{R^2}} = l\sqrt{n}. \tag{3.68}$$

In an ideal solvent, the interaction between subunits is equal to the interaction of a subunit with the solvent. In reality, a 'good' solvent is referred to the one that

cause repulsive forces between the monomers, whereas in a 'bad' one the monomers attract each other. In the first case the polymer swells and R_0 increases, in the latter the polymer shrinks and R_0 decreases. Such system can also be influenced by bulk temperature. A solvent enables monomer attraction or repulsion in various temperatures.

3.2.2   Particle modification

3.2.2.1   Polyelectrolyte shell

Polyelectrolytes (PE) are long chain macromolecules. They form charged domains after immersion in an aqueous medium [45]. Examples of natural polyelectrolytes are DNA and RNA strips. Their synthetic equivalents have wide range of applications. These macromolecules can be divided into two groups strong and weak PE, based on their ionisable groups interactions. The ionisation of strong polyelectrolytes does not depend on bulk pH variation [46, 47], whereas in the case of the weak ones the ionisation is strongly influenced by the pH of environment. Polystyrene sulfonate (PSS) is an example of a strong PE. Poly (acrylic) acid (PAA) or poly (allylamine) hydrochloride (PAH) belongs to the group of weak PE (Fig. 3.15). These structures are biologically compatible and environmentally friendly in aqueous solutions.
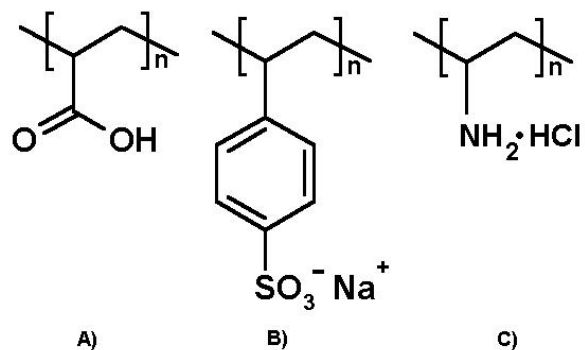
Figure 3.15: Structure of polyelectrolytes: A) Poly(acrylic) acid (PAA), B) Polystyrene sulfonate (PSS), C) Poly (allylamine) hydrochloride (PAH).

Layer by layer technique:

Every object interacts with environment through its surface. That is why, properties of any particles can be adjusted by surface modification according to application. The so called layer-by-layer polyelectrolyte deposition (LbL) technique onto particles or surfaces is a rather fast and easy method to tailor surface functionality [48]. The basic idea of this method is the deposition sequence of various materials on top of each other. Every layer contributes to multilayer structure as well as particle surface functionality (Fig. 3.16).

Various procedures were adjusted in order to achieve the best interaction between the layers so that the overall multilayer behaves according to the application [49]. They can be used for example as an ultra filtration membrane, flocculation agents [50]. Following interactions can be introduced between layers within multilayer structure: hydrogen and covalent bonding as well as electrostatic and donor/ acceptor forces. The most popular strategy is using the electrostatic interactions.
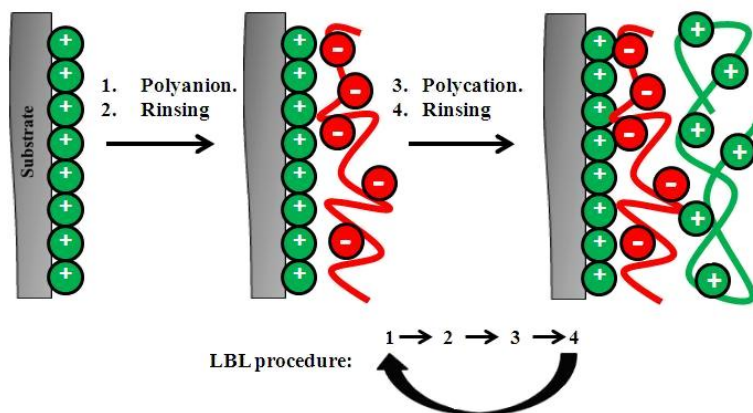
Figure 3.16: LbL mechanisms.

The added material has an opposite charge to that one on colloids (another polyelectrolyte or adhesion promoter - often deposited directly on particles as the first shell layer). Adsorption of each layer results from charge overcompensation and the particle surface charge is reversed at this stage. This process can be easily monitored via zeta potential measurement after deposition of each layer [51]. Such

polyelectrolyte multilayers influence also the colloidal stability of the coated particles via electrostatic (Sec. 3.2.1.1) and steric contribution (Sec. 3.2.1.3). Following parameters are crucial for the final multilayer structure during the LbL deposition: particle concentration, size and length distribution, concentration and polymer type as well as ionic strength of the bulk solution. The main problem in the LbL application from macro (planar surfaces) to micro scale (colloids) is the effective separation of the remaining unadsorbed charged polyelectrolytes from the particle dispersion prior to the next deposition cycle.

The LbL assembly can be performed in two ways onto colloid particles:

1) The polyelectrolyte is added at each step in sufficient concentration to form a saturated layer [52]. Recharging of the particle surface takes place with increasing bulk concentration of the adsorbing polyelectrolyte [53]. At a certain concentration, the zeta potential levels off (there is no more reversion of charge after each deposition step). The polyelectrolyte is adsorbed on the particles below this concentration. Further increase of the bulk electrolyte concentration does not influence zeta potential anymore. That is why, LbL method should be performed with optimised polyelectrolyte to particle concentration in order to form multilayers on particles by repetition.

2) The LbL process can be also held at excess concentration of polyelectrolyte [52]. Here, the unabsorbed polyelectrolyte is removed prior the addition of the next oppositely charged polyelectrolyte in order to avoid the formation of polyelectrolyte complexes in the bulk solution. An efficient rinsing can be done via several repeated centrifuging/washing cycles in pure water, followed with re-suspension of the particles, or by filtration (polyelectrolyte complexes are small enough to pass through the pores of the filter).

Particle concentration of a few - up to 10 wt. % is usually used, despite of the method. Such concentration is sufficient to avoid particle aggregation upon addition of the shell species (polyelectrolyte, nanoparticles etc...).

Zeta-potential:

Change of the zeta potential after each layer deposition gives an overview about the reproducibility of the surface properties in case of electrostatic interactions between polymers. The zeta potential sign is opposite after each polyelectrolyte layer, confirming a reversal surface charge (counter ions are taken into account). The surface potential remains the same after a complete bilayer (polyanion/polycation) deposition [54] during the first few cycles.

Zone Model for multilayers:

A shell made of polyelectrolyte multilayer film consists of three zones [55] (Fig. 3.17).The first one is influence by substrate surface properties as it is made of first layer/layers. Second region forms the bulk of the shell and it is independent of the substrate and bulk environment. The third zone consists of layer/layers close to the coating surface, which structure depends on interface with the environment.
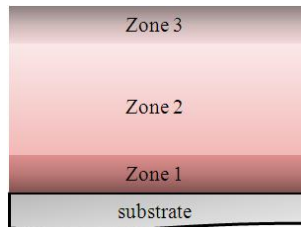
Figure 3.17: Polyelectrolyte zones.

These three zones differ from each other in both chemical composition and structure. Generally, second region is neutral, whereas two others are charged. It can be very well expressed via determination of the counter ions amount in each zone. Small amounts are present in the layer close to the substrate. Their concentration increases as the distance to the shell interface with the environment decreases. It was confirmed via construction principle (LbL) and by measurement of surface potential [56]. Since the adsorption of every layer leads to the original surface charge overcompensation, the freshly formed excess charge brings on the presence of small

counter ions. It does not mean that the excess charge is associated with polymer layers deposited as the last ones. Individual polymer layers are strongly mixed with neighbouring materials. That is why, layers far away from the surface can contribute to the surface charge excess as well.

The borders between these zones are gradual. The actual amount of layers that contribute to each region is not known. It depends on the substrate, the chemical structure of used polycation and polyanion as well as on the deposition conditions.

Mechanism of competitive Ion Pairing:

Electrostatic theory forms the basis for understanding the respond of PE system to salt [57,58]. Poisson equation determines the local electrostatic potential, caused by the local charge density. Local ionic concentration is described as Boltzmann distribution, using a mean-field approximation (Sec. 3.2.1.1). The Poisson-Boltzmann equation is then linearised by assuming low charge density in the Debye-Hückel approximation. In the elaborate D-H approximation, non-linear solution are sought. Electrostatic interactions are not specific, so their energy does not depend on the chemical identity of the charges. This energy (between same and opposite charges) is modified by screening. Thus, the Debye length decreases with higher salt concentration of the bulk solution. The electrostatic theory does not consider the polarizability of functional groups or their degree of hydration.

The overall complexation free energy change can be derivered mainly from the release of counter ions ('escaping tendency', i.e. increase in entropy [59]). Polyelectrolyte consists of segments with small free energy each. As a sum, strong association can be yielded for the whole molecule [60]. The release of hydratation water molecules should also be considered in the net energy equation since ions within polymers (and their segments) are well hydrated. In this case the term 'hydrophobicity' stands for the relative number of released hydratation water molecules.

The equilibrium is considered here as variation of place-exchange or ion- exchange reactions. Fig. 3.18 presents a standard form of interactions between charged poly-

mer segments.
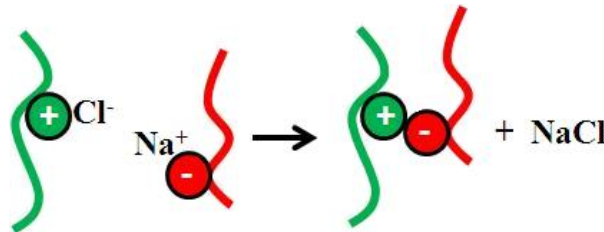
Figure 3.18: Complexation between positive and negative polyelectrolyte segments, where counterions are released.

PE segments create ion pairs and let go their counterions. The electrostatic neutrality is maintained and no chemical bonds are formed in the charged species reconstruction. 'Ion pairing' can be described as energetically favourable pairing of polymer segments, driven by the loss of water and counterions.

There are two possibilities of how the net charge neutrality is maintained via selection of polymer repeat segments and salt ions, within the as-made film. In the first method, called intrinsic compensation (Fig. 3.19), polymer positive charge unit is balance by a polymer negative charge unit [61]. Whereas, in the extrinsic charge compensation polymer charge is balanced by salt counter ions, that are provided by bulk solution used to from multilayers.
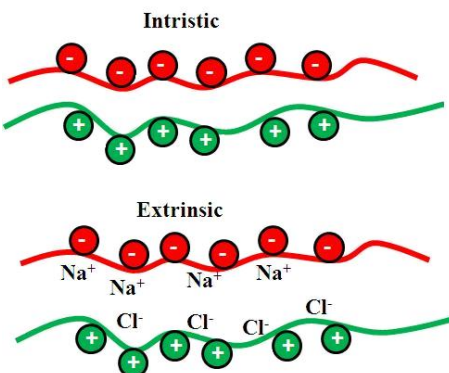
Figure 3.19: Comparison of intrinsic and extrinsic charge compensation in polyelectrolyte multilayers.

Distribution of Surface Charge in Layer-by-Layer Buildup Mechanism:

During addition of oppositely-charged polyelectrolytes, the surface excess polymer charge is firstly compensated, then overcompensated. The accumulation per deposition cycle is influenced by the magnitude of this excess surface charge. The experimental studies [62] have shown that the film thickness linearly increases with the salt concentration of deposition solution. Hence the surface excess charge is also proportional to ionic strength.

Several equivalent monolayers of polymer are built up during a single deposition step when deposition is held at concentrated salt solutions. This large polymer excess charge is accumulated in the substrate-perpendicular direction at the length equal to several 'layer thicknesses'. An explanation can be based on the fact that all the layers interpenetrate each other so all (usually two) kinds of polymers are present at all points of multilayer. This coexistence is also present on the surface, where it allows for a smooth distribution of excess polymer to occur.

When a polyelectrolyte system is controlled rapidly and reversibly by salt concentration (NaCl), the control process involves transport of small ions with minimal displacement of polyelectrolyte segment (positive: Pol^+, negative: Pol^- units). A general mechanism is represented by the following reaction:

$$Pol^+Pol_m^- + Na_{aq}^+ + Cl_{aq}^- \longleftrightarrow Pol^+Cl_m^- + Pol^-Na_m^+ \tag{3.69}$$

'm' refers to the segments in the multilayer phase. The equilibrium constant may be written as:

$$K' = \frac{\gamma^2}{(1-\gamma)[NaCl]_{aq}^2} = \left(\frac{\gamma^2}{[NaCl]_{aq}^2}\right)_{\gamma \to 0} , \tag{3.70}$$

where γ is the fraction of the multilayer in the extrinsic form and $1-\gamma$ is the intrinsic fraction [63]. Salt concentration directly controls the degree of association and interaction between polymer segments. Therefore, the higher external salt concentration, the easier separation of polymer units and enable overcompensation to penetrate further into the multilayer. The overall energy balance is based on enhanced entropy from overcompensation against decreasing available volume and

50

separation of polyelectrolyte ion pairs.

Swelling - Estimating Interaction Energies:

Swelling of the polyelectrolytes multilayers depends directly on the relative degree of association of oppositely charge polyelectrolyte segments [64]. The polymer pairs with hydrophobic complexes associate stronger when they are put into contact with water solution. Thus they are less subjected to swelling by salt (smaller K'). Sorption of both salt and hydration waters contribute to swelling process, when polyelectrolyte units coupled with salt counterions are more hydrophilic.

The free energies of association of polymer segments can be calculated via the reverse of last reaction (3.69), using: $\Delta G = RT \ln K'$. The free energy is a measure of the affinity or 'interaction energy' of polyelectrolyte unit pairs under standard conditions. Interaction energies under non-standard conditions (salt concentration other then 1 M) are given by:

$$\Delta G = \Delta G^o + RT \ln [\text{NaCl}]^2_{\text{aq}} .$$ (3.71)

The multilayer undergoes cyclic swelling and shrinking (during the repetition of multilayer formation, where the substrate is alternately immersed in salt solutions and salt-free rinse water) as ions go in and out of the film under variable bulk conditions of solution salt concentration [65].

Multilayers of weak polyelectrolytes in various pH of dipping solutions:

Analysis of PAH and PAA multilayers swelling behaviour was performed by Shiratori et al. [65]. Application of these two very popular macromolecules enabled investigation of multilayers structure modification triggered by changes of PE dipping solutions pH. Dramatic alteration in the thickness of polyelectrolyte multilayers was observed within very small shift in pH (samples had minimum 10 bilayers, no drying step in the multilayer formation process). It was observed that individual weak polycation and polyanion layers are highly sensitive to bulk environment of

their dipping solutions.

Following PAH/PAA multilayer systems were prepared:

a) dipping solutions of both polyelectrolytes had the same pH,

b) the pH of PAA dipping solution was kept constant and the one of PAH was varied,

c) the pH of PAH dipping solution was kept constant and the one of PAA was varied.

For the system 'a' at the pH within 2.5 - 4.5 the thickness of PAH adsorbed layer increases with increasing pH whereas the thickness of an adsorbed layer of PAA decreases with increasing pH. These changes are related to the increase in charge density of the PAA chains with increasing bulk pH. According to the authors, when the polyanion chains become more charged, segmental population of loops and tails decreases. At the same time, swelling of the PAH layer results from that surface charge density increase of previously adsorbed PAA (oppositely charged polycation has to neutralise the higher surface charge of highly ionised PAA surface chains). Generally at low pH (2.5 - 4.5), the thickness of adsorbed polyelectrolyte layers depends mainly on the charge density of the already adsorbed polyelectrolyte layer and of the surface. Thickness, conformation (segmental population of loops, tails and trains) and free ionic bindings sites of previously adsorbed polymer layer are not relevant in this pH range.

In the pH range between 4.5 - 6 a significant thickness transition for the system 'a' was observed. Thickness of both polyelectrolytes increased rapidly at the pH of 5. Further change of pH up to 6 led to significant shrinking of the whole multilayer down to few Å. In this range the PAH chains are fully ionised whereas PAA chains are closed to be fully ionised. Such alternate deposition of fully charged chain onto nearly full charged chain results in unusually thick adsorbed layers.

Further increase of pH up to 6 - 7.5 caused full ionisation of both macromolecules, therefore the multilayer thickness was measured to be still just few Å.

Full ionisation of PAA chains and decrease of PAH ionisation degree occurs at the pH of 7.5 - 9. The system again consists of fully ionised and nearly fully ionised

PE. Such interactions lead to significant swelling with increased pH.

In the system 'b' the pH of PAA dipping solution was kept constant at 3.5 and 4.5 and the pH of PAH was varied from 2.5 up to 8.5. PAA has relatively constant thickness (about 20 Å for both cases of dipping solution pH: 3.5 and 4.5) in the pH range 2.5 - 4.5 (dipping solution of PAH). In this conditions thickness of PAH polyelectrolyte increases (10 - 45 Å) with increasing pH. Situation changed when the PAH solution has pH above 4.5. PAA layer thickness increases up to over 40 Å (5.0 of PAH solution) for both 3.5 and 4.5 cases and further increased with increasing pH of PAH. The last measured thicknesses for both PAA layers reached 60 Å at pH 8.5 of PAH dipping solution. PAH at the same time continues to swell with pH till pH 6.0. Thereafter it stays at the similar value (PAA pH 3.5) or drop to lower values (PAA pH 4.5).

The authors give a following explanation for this behaviour: in the pH range of 2.5 - 4.5 the fully charged PAH chain is adsorbed onto a PAA surface. The PAH solution pH determines how many of the remaining acid groups within PAA loops become ionised. With increasing pH the more of PAA loops become charged, the more PAH is needed to neutralise this charge. As an overall result PAH layer thickness increases with pH until the PAA chains become fully ionised at the pH of about 6.5. The thickness of these two polyelectrolyte layers at the pH> 5.0 increases to the extent that the surface contains mainly segments of only the outermost polymer layer. When PAA is the outermost layer, it contains a large number of free carboxylic groups. In the case of PAH as the outermost layer, these free acid groups become ionised during PAH deposition and form ion pairs with cationic groups of PAH. The surface layers are enriched with segments from outermost layer. Once the next layer is deposited, it can interpenetrate into previously adsorbed layer and overall thickness remains similar.

In the case of the last system 'c' the pH of PAH dipping solution was kept constant - 2.5 and the pH of PAA solution was varied from 2.5 up to 8.5. The thickness change in the range of 2.5 - 4.5 (PAA dipping solution pH) has similar trend as in

the previous system 'b'. Above pH 4.5 it was shown that the deposition process stops after deposition of few layers of polyelectrolytes. In these conditions PAA layer is adsorbed as highly charged chain. The pH is dropped to lower values as PAH is deposited (constant pH value: 2.5). Under such conditions, the negative surface charge of PAA layer is decreased to the point that the surface takes on a net positive charge from previously adsorbed PAH layer. Since a positive charged PAH chain is attempting to adsorb onto positively charged surface, the sequential adsorption is not possible.

Hollow Polymer Shells:

The interactions between PE in multilayer shells are strong enough to create hollow shells made just of polyanions and polycations. In the preparation method, soluble cores are used as templates for step-wise deposition. Donath et al. [66] reported a colloid-template consecutive polyelectrolyte adsorption followed by decomposition of the templating core. PSS and PAH polyelectrolytes were used to create micron-sized shells with the thickness of few to tens of nanometer. The template for shells was made of monodisperse weakly cross-linked melamine formaldehyde colloidal particles that were decomposed in 100 mM solution of HCl after the LbL procedure. These shells have numerous advantages. Their composition and thickness can be easily controlled as well as their physical and chemical properties can be adjusted during the production. Moreover, they are extremely stable against chemical and physical influences giving opportunity for a wide range of application. These hollow polyelectrolyte shells can be used as micro and nanocarriers for various molecules and nanoparticles or as nucleation centres for subsequent crystal growth in constrained environment.

Polymer Shells with incorporated functional molecules:

As mentioned in this chapter LbL polyelectrolyte shells are promising answer to the need of a control ('smart') release of functional agent (like inhibitor molecules

realised to the corroding area) triggered by environment properties change (pH, mechanical deformation of bulk material-self-healing coatings, Chap. 5.2). Incorporation of these functional molecules can be performed in two ways. Firstly it can be stored in the pores of the solid colloid and covered with polyelectrolyte shell [TiO_2 - mesoporous material , Sec. 5.2]. Secondly it can be incorporated as one of the layers in polyelectrolyte shells.

The LbL deposition procedure by Shchukin et al. [53]was followed for both large polyelectrolytes and small benzotrialzole molecules on SiO_2 nanoparticles in order to produce an inhibitor loaded polyelectrolyte shell. The layer build up was monitored via zeta potential. It was shown that large multicharge chains of adhesion promoter PEI (polyethyleneimine) and PSS have strong negative electrostatic forces that enable sufficient adsorption to recharge the colloid surface. In case of small positively charged inhibitor molecules, only compensation of the excess charge was achieved. Change of the surface charge was large enough to cover the inhibitor layer with PSS shell as the outermost polymer to enable smart release on functional molecules, triggered by pH change.

3.2.2.2   Monolayer formation on particles

Monolayer adsorption on a flat surface differs from its deposition on nanoparticles due to the fact that these structures have much higher percentage of interfacial atoms within total number of atoms in comparison to bulk materials. The smaller particle diameter the higher the number of atoms located at the interface between the particle and the surrounding environment, a 2 nm particle has 58% surface atoms, whereas a 100 nm 1.2% [67]. As a result a strong interplay between SAM and nanoparticles occurs. The self assembly process is govern by chemical reactions, thus it is independent of particle size. The SAM structure however, is strongly influenced by curvature and defect rate of a given surface. SAM spontaneously stabilises the reactive surface of the particle as well as introduces new functionality at the particle- solvent interface. Tailoring of organic surfaces on particles is a useful

application in nanotechnology. Chain density of a SAM decreases with the distance from core on substrate with high radius of curvature. The decreasing density is indicated by higher mobility of terminal methyl groups in case of n-alkenothiols. A cone shape can be a representative of the available space for a long chain thiol molecule (Fig. 3.20). The alkyl chain fills almost completely the volume of the cone at the surface of nanoparticles but it is unable to fill the larger end of the cone, providing enhanced mobility of the molecule part.
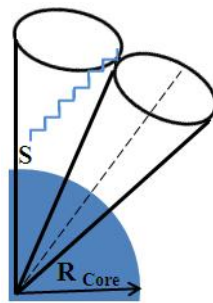
Figure 3.20: Schematics of long chain thiols on a particles with a R_{Core} radius. A cone shape as available space for a thiol is highlighted.

The hypothesis that outer part of thiol layer is loosely packed was proven by measurements of the hydrodynamic radii on monolayer protected gold nanoparticles [68]. Theoretically, a nanoparticle coated with well-packed SAM was supposed to have a hydrodynamic radius equal to the sum of the radius of the gold core and the fully extended alkanethiolate, but it was never confirmed experimentally [69]. Measured hydrodynamic radii of SAM coated gold particles are smaller than theoretic values, indicating that the monolayer is not well packed along the outer edge. IR and NMR spectroscopy provided information about the packing density of the alkyl chains on nanoparticles [70–73]. These studies showed that the number of gauche defects in chains (for any chain length) is much higher in SAMs on nanoparticles then on planar surfaces [71,74]. It was also proven that SAM on nanoparticles have a lot of near surface and internal kink defects like in flat monolayers of alkanethiols with similar chain lengths. With increasing particle size, the monolayer

properties become similar to planar structures. Particles larger than 4.4 nm, coated with a SAM of dodecanethiol have spectroscopic and physical properties like planar monolayers [75]. Flat (111) terraces occur in majority on particles surface with such diameter. These areas are sources of well packed SAMs.

3.2.2.3 Particle incorporation in polyelectrolyte growing films on metal

Development of self healing polyelectrolyte coatings (Sec. 5.2) on metal surfaces requires functional (inhibitor loaded) particle incorporation into the coating matrix, along layer growth. These particles have to be compatible with the coating matrix in order to avoid distortion due to their presence. The capsules should be in nanometre scale size, uniformly distributed within the protective layer. That is why, particle surface chemistry is essential. It is influenced by bulk coating material, particle core and inhibitor solvent (it is important when nanocontainers are e.g. hydrophobic outside and hydrophilic inside-halloysites [76]). The LbL approach (Sec. 3.2.2.1) seems to be the most appropriate as the surface properties can be easily controlled and adjusted. Study on direct incorporation of the active agent have been performed. Non-capsulated inhibitor occluded in the sol-gel matrix decrease substantially its stability and adhesion to the metal substrate [77]. That is why, functional material has to be stored in nano reservoirs to isolate the substance within the matrix and prevent its direct interaction with the bulk material.

Storage of corrosion inhibitors in polyelectrolyte multilayers gives a lot advantages as PE reveal controlled permeability properties (Sec. 3.2.2.1). They can be adjusted by changing pH [65], ionic strength, temperature and humidity on the level of nanoreservoir shell. Such system provides intelligent release of the agent around damaged area. Corrosion activity leads to local changes of pH [78]. The phenomenon causes polyelectrolytes to swell and open multilayers pores, where inhibitor is stored.

Kinetics of uniform particle film formation between polymer layers is crucial when it comes to production application. Lvov et al. [79] performed QCM studies on finding the minimum time for producing good quality films of 45 nm SiO_2 particles

within linear quaternary ammonium polymer (PDDA). Conformational changes of silica particles upon adsorption probably influence the time needed to make uniform monolayers. The mechanism of PDDA relaxation is not clear, but sample drying after adsorption of each particles/polymer bilayer speeds up the process even 100 times.

3.3 Monolayer formation on metals and metal oxides

3.3.1 Self-assembled monolayers (SAM)

Self organisation of molecules occurs on an interface. The resulting phase is considered as a fourth state of matter in nanometer scale [67]. This assumption is made due to high percentage of constituent atoms of nanometer-scale structures at a surface, where gradients of properties are the greatest. It is known that atoms or molecules at the material surface have free energies, electronic states, reactivities, mobilities and structures [80,81], that differ from the bulk quantities. That is why, the physical properties of nanostructures depend mostly on their surface and interfacial environment. Organic materials tend to adsorb spontaneously on metal and metal oxide surfaces in order to lower the free energy of the interface between the metal or metal oxide and medium. These adsorbates have strong effect on nanostructures stability. They can act against aggregation or e.g. decrease reactivity of the surface atoms [82–85].

Self organisation of bi-functional molecules at the metal and metal oxidel surfaces has attracted a great attention. It provides a simple way to tailor interfacial properties of a substrate according to desired application. Basic study on self-assembly mechanism of organic monolayers at metallic surfaces has focused on the alkanethiolate/noble metals system, where thiol molecules adsorb spontaneously onto the metal surface to form a highly ordered array [67].Other known systems are SAMs made

of organophosphonates and organosilanes on oxide/hydroxide covered aluminium alloys, zinc covered and bare steel surfaces [3–5].

SAMs have a thickness of 1-3 nm, which makes them the most elementary form of nanometer-scale organic thin-film material. It is possible to control this organic structure in a range on 0.1 nm by choosing the proper molecule (chain length, chain structure, functional head/tail group, Fig. 3.21). SAMs can be applied to the surface by means of micro contact printing technique (μCP) providing a surface with desired pattern. It can posses different properties then the rest of the sample (e.g. hydrophobicity or surface charge). It is a perfect substrate to study adsorption selectivity of nano or micro-scale particles.
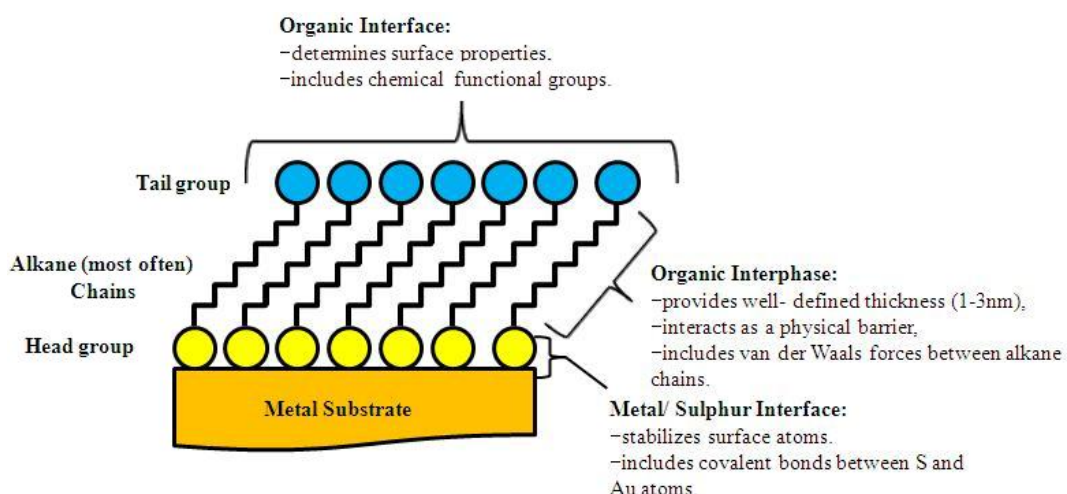
Figure 3.21: Schematics of a perfect SAM of alkanethiolates adsorbed on a gold surface with a (111) texture. The structure and characteristics of each layer are highlighted.

SAM consists of bi- or mono-functional molecules. Such a molecule has a chemical group with a high affinity of the substrate, providing chemisorption of the monolayer. Moreover, the molecule has to have chain made of e.g. methylene groups (alkyl chain) with a proper length. Van der Waals (Sec. 3.2.1.1) forces between those molecule chains govern self organisation process. It is known [86] that the longer the chain, the higher organisation of molecules inside SAM. The last part is the second functional group. The tail group interacts with the bulk environment

as well as with neighbouring molecules. The most typical configuration for SAM is gold substrate and thiol molecules. Thiol group has a very high affinity to gold with a free energy of adsorption $\sim$ -5 kcal/mol [87]. This value depends slightly on the aliphatic chain length of the alkanethiol adsorbate.

Au-S covalent bond is strong enough (ca. $\sim$50 kcal/mol) to anchor SAM [88].
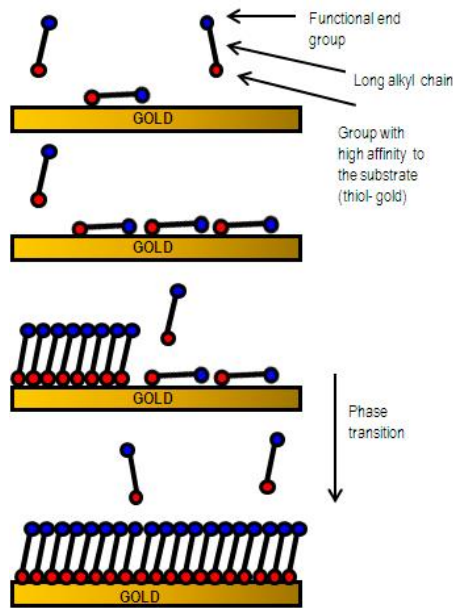
Figure 3.22: Self assembly mechanism of alanethiol molecules on a gold substrate.

Thiol SAMs form on substrates by spontaneous adsorption from either liquid or vapour phase. The assembly of SAM from solution follows the Langmuir adsorption model. The structural phase transition is believed to be similar for the assembly from solvent and gas phase [67]. There are many factors that can influence this process, such as: solvent, temperature, adsorbate concentration, immersion time, substrate purity and structure and most importantly thiol construction: chain length, head group etc.

SAM are usually prepared in organic (1-10 mM) freshly prepared solution by dip-coating of a clean substrate for several hours at the room temperature. Milimolar solutions provide fast dense coverage of adsorbates within first minutes from dipping. Much longer time is required in order to form SAM with maximum molecule

density and minimum defects. A general SAM mechanism can be described as follows (Fig. 3.22): in the first few minutes the process begins with adsorption of e.g. alkanethiol onto gold with their molecular axis parallel to the surface [89]. The first phase is called low density or 'lying down' phase. Continued exposure to alkanothiol solution leads to saturation by increase of surface coverage. A two-dimensional phase transition occurs, where thiols stand up and tilt their axis $\sim 30^o$ from the surface normal to reach equilibrium space between chains [90]. The alkyl chains orient themselves in a so called 'standing up' phase. It can take hours up to a day for a complete formation of SAM.

The process can be monitored by means of Infrared Spectroscopy technique (Sec. 4.3.2). Position of methylene group stretching modes (alkyl chains: n -CH$_2$-) in the IR spectrum is the most precise confirmation of chain order [91]. It has been published that an ordered aliphatic monolayer contains chains in the 'standing up' phase ('crystalline' state, all-trans configuration) characterised by: CH$_2$ vibrations in stretching mode with position $\nu_{\text{CH}_2\text{asym}} < 2920$ cm^{-1} and $\nu_{\text{CH}_2\text{sym}} < 2850$ cm^{-1} [92]. A not perfectly formed SAM (e.g. still in the transition phase- 'liquid' state) CH$_2$ vibration peaks are claimed to be at higher wavenumbers in the IR spectrum. Moreover, comparison of the peaks intensity can provide information about the monolayer structure [93]. For a mono-functional molecule, with a -CH$_3$ group (2858 cm^{-1}) as the tail group, the peak intensity ratio: CH$_3$/CH$_2$ is significantly increased (in comparison to bulk spectrum) when the molecule is well ordered on the surface. What is more, the mean tilt angle (α) can be calculated from the peak ratio:

$$\frac{I_{\text{CH}_2}}{I_{\text{CH}_3}} = \frac{n2\cos(90^o - \alpha)^2}{3\cos(35^o - \alpha)^2} \tag{3.72}$$

Chain tilting provides accurate separation distance between the chains. SAM molecules adopt confirmations that allow high degrees of vdW interactions [90,94] with neighbouring molecules in order to minimise the free energy. These reorganisations promote a secondary level of assembly that is present in the long phase transition (standing up phase).

Interplay between covalent strong bond layer of metal-sulphur interaction and noncovalent lateral interaction among organic groups has influence on the self-organisation as well. The specific ordering of sulphur molecules on the metal lattice defines the free available space for organic components. The organic layer assembly results from maximising the attractive lateral interactions (vdW) within geometric limitations imposed by the structure of the adlayer. On the other hand, the organic groups can also confine the density of coverage by steric crowding [67].

Solvent is an important factor, which influences dynamic equilibrium. It governs the molecule adsorption. Additional interactions (solvent-substrate, solvent-adsorbate) contribute to thermodynamics and kinetics of assembly. Solvent-substrate interactions can hamper thiol adsorption rate from solution. The solvent molecules must be replaced by adsorbate, it happens only when substrate-adsorbate interaction are stronger then solvent-substrate interactions. What is more, it was shown that lower molecular solubility promotes their segregation at the metal surface, driving the assembly process more efficiently [95]. (Solvent polarity influence: Sec. 5.3).

As written before, usual SAM formation procedure does not require any special temperature control, but it was shown that temperatures above 25^oC can improve the formation kinetics and reduce the defects number [96].

The formation of SAM is accompanied by variation in the Gibbs free energy at the modified solid surface [97, 98]. In order to design a desired SAM surface, one has to understand the interfacial energy variation as well as the self-assembly process itself. It was already proven that the chain length of alkanethiol molecule and the substrate structure may influence the surface stress (induced by self-assembly) that is crucial for the variation of surface energy [97, 99–101]. Surface-energy variation can be expressed as generation of surface stress [102]. At the molecular level, there are three main contributions to the surface energy change: the interfacial energy variation at the Au-head group interface (Au-S bonding), chain-to-chain interactions and interactions between the tail-group and the bulk environment. The entire surface-

energy variation during the self-assembly process can be expressed as:

$$\Delta G = (\Delta G_{\text{Au}-\text{initial}} + \Delta G_{\text{Au}-\text{S}}) + \Delta G_C + \Delta G_t \,, \tag{3.73}$$

where, $\Delta G_{\text{Au}-\text{initial}}$ is the disparity between the surface-energy of gold in the self assembled medium and that of initially neat gold, $\Delta G_{\text{Au}-\text{S}}$ is the energy change at the interface of Au-S bonds, ΔG_C represents chain to chain interactions and ΔG_t is the contribution from the SAM tail groups interactions with the medium (interaction energy unit is: Jm^{-2}).

Each of three mentioned SAM layers/contributions has individual function to overall monolayer properties. Mobile Au-S bonds give thiol SAM initial connection to surface. The bond is slightly polar because of a shift in electron density from gold towards the sulphur atom [67, 103, 104]. The electron shift has been calculated as about 0.30 e [105]. Coulomb repulsion between adjacent dipolar Au-S bonds might be the source of surface stress induced by self assembly. The strong repulsion at the gold surface can cause lattice relaxation and even surface reconstruction [106, 107]. Chain to chain interactions contribute to the surface stress generation in the next layer of SAM. The surface energy variation was evaluated as a function of the molecular separation between two parallel alkanethiol molecules, using the universal force field (UFF) approach [108]. According to Godin's calculations [109] the equilibrium separation between two alkyl chains should be 0.44 nm. Gold substrate (111) has a $\sqrt{3} \times \sqrt{3}R30$ lattice with a 30° tilt angle [90]. It results is an effective chain separation of 0.43 nm. It indicates that the longer alkyl chain, the higher compressive surface stress, generated during the self-assembly. The last layer of SAM consists of tail group that interacts with the surrounding environment. This contribution to overall surface energy variation is relatively smaller than the previous ones [102], but it can have a profound influence on the SAM structure (further details in the next chapter). The substitution of the terminating methyl-group by other functions can have a strong influence on the molecular orientation and the structure of SAMs [110].

3.3.2 Functional monolayers

SAM most interesting application is adjusting of physical (wettability) and chemical (reactivity) properties of a surface via choosing an appropriate tail/end group of a molecule. Orientation of molecules is the quality factor of a SAM since well ordered monolayer provides a homogeneous surface [111]. Expanded studies have shown that functionalization of long alkyl chain molecules leads to a different behaviour in comparison to methyl-terminated alkanethiols [110]. The molecular orientation within the SAMs is strongly influenced by the type of tail groups and by their mutual interactions.

X-ray photoelectron spectroscopy have shown that OH-terminated alkenothiols display minor variations in the tilt-angle in comparison to methyl terminated molecules [110]. In the same studies highly oriented films could not be obtained for COOH-terminated thiols. The phenomenon is explained by formation of hydrogen bonds between initially adsorbed molecules (in 'lying down' phase) that prevents further transition into 'standing up' phase (Sec. 3.3.1). The hydrogen bonds are three times stronger in carboxylic - than in the hydroxyl-group. Therefore, layers made of bi-functional molecules may not exhibit the structure for methyl terminated SAM by standard preparation methods.

The structural quality and chemical composition of carboxy-thiol SAMs were found to be highly sensitive to preparation conditions during immersion of gold substrate in ethanolic solution [112]. SAMs contained a significant amount of deprotonated acid groups (proven by a characteristic carboxylate vibration in IR spectra) in ethanol with the highest available purity. Moreover it was shown that monolayer prepared from diluted solutions had a significantly higher degree of crystallinity and molecular orientation than films formed from concentrated solutions. Those less oriented films display a high density of carboxylic acid cyclic dimmers, suggesting that these dimmers already exist in solution and are not dissociated upon adsorption onto gold substrate. Fully protonated carboxy-terminated SAMs were obtained either by

adsorption from acidified solutions or by a sequent immersion into solution of an organic acid in ethanol. This improved preparation of carboxy-terminated SAM was presented by H. Wang [113]. Small amount of CF_3COOH was added into ethanolic solution of alkanethiols during SAM formation followed rinsing in ethanolic solution of NH_4OH. Amine terminated SAM also exhibits disorder by standard preparation from an ethanolic solution. In the same studies, an alternative preparation method for NH_2-terminated SAM is introduced. Correspondingly, $N(CH_2CH_3)_3$ is added during monolayer formation, followed by rinsing in CH_3COOH. Hydrogen bonds between tail-groups are damaged for both kinds of molecules. SAMs prepared in such a way have higher quality than the ones from pure ethanol. M. Wallwork et al. [114] have introduced another method to obtain high-quality amine-terminated SAMs. Their self-organisation can be adjusted by proper pH and ionic strength. An electrostatic repulsion between two SAM electric double layers (modified AFM tip vs. substrate) is the reason for the zero adhesion at low pH. The large adhesion at intermediate pH is attributed to a hydrophobic interaction between exposed alkyl chains due to disorder in the SAMs. This hydrophobic force is very much reduced in low ionic strength conditions. It was suggested that this phenomenon is due to increased ordering in the SAM caused by strong in-plane ionic hydrogen bonds formed between ionised acid groups and neutral amines.

3.4   ZnO nanocrystallines films.

Zinc oxide nanocrystalline film is a material with wide spectrum of applications. It can be used as surface pre-treatment to homogenise engineering materials for better adhesion of protective layers [12]. Furthermore, ZnO nanorods films are employed as selective biosensors with enhanced active surface area [11]. Functionalization of those nanocrystalline layers brings on better performance of the material in both application aspects. Hence, the studies on nanocrystals surface modification via organic acids SAM were conducted in the frame of this work [5.3, 5.4]. ZnO

nanocrystalline films have excellent chemical and thermal stability as well as wide band-gap. Thus, it is an attractive material for high-technology applications (production of photodetectors, sensors, photonic crystals etc.). It was recently recognised that only highly orientated nanorod ZnO arrays are essential for performance of the future devices, therefore preparation procedure must deliver such crystal assembly.

ZnO crystals grow in wurtzite structure with well-defined crystallographic mixed faces: polar zinc terminated top (0001, 000 -1) and non-polar oxygen terminated side walls (10 -10, 11 -20). The ZnO face 10 -10 is energetically most favourable surface among all orientations [115]. The polar surface is generally energetically unfavourable unless the surface charges are compensated by passivating agents. The anisotropic growth of ZnO nanocrystals along the c-axis allows the deposition of high aspect ratio (height to width) crystallites, resulting in their final crystal form: nanorods (NR). The crystalline films were prepared by means of hydrothermal synthesis directly on quartz crystal gold electrode [4.2]. The deposition from aqueous solution of zinc oxide thin films involves controlled precipitation on a substrate (i.e. galvanised steel or gold layer covered with zinc seed layer) via hydrolysis and condensation reactions of metal ions complexes from aqueous solution [116, 117]. This procedure delivers nanorods with density of even 70 billion rods per square centimetre. The geometric parameters are adjustable by changing the growth time, suspension composition as well as Zn seed density. Quartz crystal electrode surface was modified according to method described in the experimental section. Zn seed layer made with 5mM Zinc Acetate ethanolic solution was heated up to 350C for several hours in order to achieve uniform coverage of zinc acetate crystallites. Annealing lower then 100C causes seeding itself to fail due to dissolution of zinc acetate crystallites during subsequent step in nanorod growth bath. Temperature between 150 - 200C is needed for seed assembly, whereas higher temperatures promote mainly seed crystalline and growth. The morphology of ZnO nanorods in terms of size distribution are significantly affected by the regularity and crystal size of the seed, which acts as initial sites for the crystal nucleation [118]. In the hy-

drothermal synthesis, the seed modified substrates are dipped into aqueous solution of zinc nitrate and methenamine. The controlled fabrication and direct growth on seed crystallines is govern by thermal decomposition of those two salts. Adjustment of temperature, dipping time as well as ingredients concentration enables control of the NRs width and height. By proper tuning of those experimental parameters, production of two-dimensional highly oriented nanorod arrays of ZnO is within reach. Zinc cations Zn^{2+} are solvated by water giving rise to aqua-ions $[Zn(OH_2)_n]^{2+}$ in aqueous solution. A range of monomeric structures: $[Zn(OH_2)_{n-p}(OH)_p]^{(2-p)+}$ and other hydroxyl species $[Zn(OH)_n]$ are formed in dilute solutions [116]. Subsequently condensation reaction must take place in order to form the polynuclear arrangement, which develops into metal oxide particles. Therefore, chemical complexation is necessary to generate zinc oxide from zinc salts [15]. The equilibrium of aqua complex of Zn^{2+} is poorly affected by pH and ionic strength due to inherent lack of ligand-field stabilisation energy. Moreover, water is not able to deprotonate hydrated divalent Zinc cations at ambient pressure. As a result electrostatic control of interfacial tension and nucleation free energy cannot be efficient. The easiest way to obtain anisotropic nanostructures of ZnO is to lower the overall reagents concentrations and keep them in 1:1 ratio. Decreasing the concentration of precursors by one order of magnitude led to respective decrease of nanorods's size due to the critical diffusion of the monomers and the subsequent limited growth. Concentration, in the range of 1-5 mM, delivers nanorods with 100-200 nm width [Fig. 5.15a)]. Tuning of crystals morphology is important for incorporation of ZnO nanocrystalline layers into various techniques as substrates, where films with lower mean roughness are needed. Addition of a growth promoter (sodium citrate dehydrate) into aqueous solution of zinc salts results in modified ZnO nanocrystalline films [5.4]. The obtained layer has more dense packing of nanocrystals and continuous crystalline film of hexagonal plates is formed. By adjustment of growth promoter concentration, ratio of crystalline orientation can be controlled. The standard nanorod shape (Fig. 5.15a) presents a high proportion of non polar side surface to polar tip. In the case

of continuous films the aspect ratio is much lower since polar tip area is increased and the non polar sides faces are decreased as seen in the Fig. 5.23a. Such change in morphology can lead to different surface stability along functionalization with alkyl phosphonic acids molecules (chapter: 5.4).

68

Chapter 4

Experimental

4.1 Materials

4.1.1 Preparation of polyelectrolyte covered TiO$_2$ nanocontainers

Mesoporous Titania was synthesised by oxidation of titanium carbide with 5 M HNO$_3$ (Sigma-Aldrich). The obtained particles were approximately 250 nm in size and contained 10 nm diameter pores. According to XRD analysis [119], the titania network comprises of anatase crystallites with an average size of $\sim$6 nm. Surface modification was conducted by polyelectrolyte shell formation of the nanoparticles, using the LbL assembly approach [120], (Sec. 3.2.2.1). Since the TiO$_2$ nanoparticles themselves are negatively charged, the layer of positively charged polyelectrolyte (poly (allylamine hydrochloride) - PAH, Sigma-Aldrich) was applied first from 2 mg/ml PAH aqueous solution. Production of the negatively charged NCs with a polysodium 4-styrenesulfonate (PSS, Sigma-Aldrich) or polyacrylic acid (PAA, Sigma-Aldrich) monolayer was achieved by deposition from the appropriate polyelectrolyte aqueous solution (2 mg/ml) after carrying out thorough centrifugal washing of the PAH treated NC's. The thickness of polyelectrolyte shells obtained by this process was in the region of 10 nm.

Once prepared the NC suspension was allowed to precipitate for few hours (to avoid the presence of very large NC agglomerates), after which 6 ml of the upper layer was decanted and diluted either with 400 mL of distilled water (Sections: 5.1, 5.2) or a pH adjusted solution containing different KCl (99.5 %, Merck, Darmstadt, Germany) concentrations. Additionally, the zeta potential (ζ potential) and particle size in all TiO_2 NCs suspensions (Sec. 5.2) were measured using a Zetasizer (Nano series, Malvern Instruments, UK).

4.1.2 Self-assembled monolayers (SAM) on Au-quartz crystal surfaces

The gold coated quartz crystal substrates (AT-cut 5 MHz, Fil-Tech Inc, Boston MA) were cleaned in an amino-peroxy solution (NH3 25%, H_2O_2 35%, 1:1) at 80º C for 1 hour. A SAM layer was then deposited from either a 1 mM 15-mercaptopentadecanoic acid (MUA, 99%, Sigma-Aldrich, Germany) or 1 mM 11-Amino-1-undecanethiol hydrochloride (AUT, 99%, Sigma-Aldrich, Germany) solution in ethanol by immersing the sample in the solution for several hours. Presence of the SAM layer was determined for each sample surface by means of Polarisation Modulated Infrared Reflection Absorption Spectroscopy (PM-IRRAS-Photoelastic Modulator-PMA 50 Bruker, FTIR-Spectrometer Vertex 70-Bruker Optics).

4.2 Preparation and characterisation of ZnO nanorod and continuous crystalline films on quartz crystals

In the first step, the quartz crystal gold electrode was modified with Zinc seed layer. The substrate was dipped into 5 mM ethanolic solution of Zinc Acetate (shortly after cleaning with RCA solution-H_2O: H_2O_2: NH_3, 1:1:1, for 1h at 75ºC. A liquid

drop was left on the gold electrode surface for 10 s, while the crystal was slowly moved from one side to the other for a homogeneous seed layer deposition. The sample was afterwards dried with pure nitrogen. The procedure was conducted four further times, with short ethanol rinsing step before drying. Crystals were then heated up to 350°C for 8 hours. The whole process was performed twice to ensure uniform Zinc seed layer coverage, which is the crucial factor for a well formed NR film growth. The morphology of ZnO nanorods in terms of size distribution are significantly affected by the regularity and crystal size of the seed, which act as initial sites for the crystal nucleation [118].

ZnO NR film growth was performed in an 0.05M aqueous solution of zinc nitrate, $Zn(NO_3)2 \times 6H_2O$ (99% Puratonic, Alfa Aesar) and hexamethylenetetramine (HTMA) C6H12N4 (99%, Alfa Aesar). The crystals with Zn seed layer were dipped in the stirred solution for 30 min. The growth temperature was set up to 90°C. Deposition of continuous film was achieved with the same method by addition of growth promoter Sodium Citrate to the aqueous solution (6mg/ 100mL). Samples were stored in desiccator prior all experiments.

Before each experiment, the sample surface topography was examined via FE-SEM. These images gave an indication of the final shape of nanocrystalline films (Fig. 5.23a). The substrates were imaged again after QCM experiments. The measurements were performed at an accelerating voltage of 1.0 or 2.0 kV in order to display the organic layer on top of metal oxide film.

Surface energy change was measured with water contact angle (WCA) apparatus before and after experiments.

The surface chemistry was measured with FT-IR Nicolet reflection cell (by 78°) after each experiment with pure ZnO (nanorod or continuous) nanocrystalline film as a reference.

4.3   Analytical Techniques

4.3.1   In-situ adsorption experiments via QCM

In order to monitor adsorption processes in-situ, a quartz crystal microbalance (QCM) operated via impedance analysis was employed. The software determines the crystal's conductance spectrum in a range around the resonance frequency and fits resonance curves to these spectra with the centre frequency and the bandwidth used as the main fit parameters (Sec. 3.1). The term 'bandwidth' or energy dissipation used here always refers to the half-width at half maximum (HBHW, $\Delta\Gamma$, Fig. 3.4). These values can be determined on a number of different overtones, which provides redundancy and the possibility of data cross checking. The comparison of the shifts in frequency and dissipation at various harmonics can be used for detailed modelling of the adsorbate acoustic and viscoelastic properties.

Prior to each experiment, six harmonics between 5 and 55 MHz were identified from the conductance spectra and pure solvent (with the same parameters as the adsorbate solution) was pumped through the cell to achieve a stable baseline. Once the resonance frequency was stabilised, the adsorbate solution (stirred water dispersion of the NCs or ethanolic solutions of alkylphosphonic acid was pumped through the sample compartment at a rate of 0.04 mL/min. Adsorption was considered to have stopped when a stationary state was reached for all established harmonics. The cell was then purged with pure solvent.

The QCM results are presented as parameter shifts at the normalised 5th overtone as a function of time in sections 5.3 and 5.4. Such display enables an easy presentation and comparison of the data on adsorption kinetics with higher sensitivity. The results are compared for various liquid systems. All the experiments were carried out with the same device using the same parameters above the same kind of substrate (nanorods - 5.3, continuous film - 5.4). Thus, any variations have origin in interface phenomena. The following molecules were used: decanphosphonic acid (DPA), tetradecanphosphonic acid (TDPA) and octadecanphosphonic acid

(ODPA) (Sigma-Aldrich, Alfa Aesar Germany). All alkyl phosphonic acid solutions were prepared in ethanol with concentration of 1 mM.

The impact of the medium polarity on ODPA deposition was monitored in the chapter: 5.3. Two additional QCM experiments were performed with 1 mM ODPA solution in isopropanol and mixture of chloroform with ethanol (1:1).

In the section 5.4 modified ethanolic solutions of ODPA were also used. The mechanism of the adsorbate layer deposition was verified by QCM experiments where additional amount of Zn^{2+} ions (1 and 0.1 mM Zn Acetate) was added into the standard 1mM ODPA ethanolic solutions.

Subsequently the quartz crystals surfaces were examined by means of PM-IRRAS-/FT-IR (Sec. 4.3.2), Water Contact Angle (WCA) (Sec. 4.3.3) or Field Emission Scanning Electron Microscopy (FE-SEM) (Sec. 4.3.4). These data give an indication of the final coverage.

4.3.2   Infrared spectroscopy

Infrared spectroscopy provides information about molecular structure by inducing vibrational excitation of covalently bonded atoms and groups via subjection to electromagnetic radiation with frequencies between 4000 and 400 cm^{-1} (wavenumbers-the number of electromagnetic waves per centimetre) the infra red (IR) region [121]. The absorption takes place when the IR energy is in the range of the rotation or vibration mode of a dipole moment (interatomic bond) inside a molecule. Vibrations of the dipole moment induce an alternating electric field that interacts with the electric field of IR. Selection rules for this method, state that a vibrational mode is IR active when there is a change in the molecular dipole moment during the vibration ($\Delta n = \pm 1$). Antisymmetric vibrational modes exhibit significant IR adsorption due to polar groups. Numerous chemical bonds, inside a molecule, absorb altering intensities and frequencies. The IR spectroscopy involves collecting adsorption intensity as a function of wavenumber in the form of a spectrum. The frequencies signals

with higher absorption intensity can be directly associated to a specific bond within the analysed molecule. Region 1450 to 600 cm^{-1} is called the 'fingerprint' region since it provides characteristic absorption bands for most of the molecule bonds. Individual bonds can absorb at more than one IR frequency since it may vibrate in several different motions (e.g. stretching or bending) with various overtones of the resonance frequency. Thus, presence of a molecule can be confirmed in the group frequency region (4000 to 1450 cm^{-1}). Absorbency peaks are shifted to higher or lower frequencies when molecules are subjected to alternate environment (e.g. by changing solvent pH, by changing nearby atoms in a molecule or by self-organisation on a substrate).

The wavenumber is the reciprocal of wavelength: $\lambda = \nu/c$ (ν- frequency, c-speed of light $\approx 3 \times 10^8$ m/s). During the exposure to IR radiation, a molecule is excited to a higher vibrational state by direct absorption of the light. The transmittance (T) at a given wavenumber can be calculated as follows:

$$T = \frac{I}{I_0}\,, \tag{4.1}$$

where I_0 is the intensity of the entering radiation, I is the intensity of the transmitted light (after partial adsorption by a sample). Spectra can be also displayed as the absorbance (A) at a given wavenumber. The parameter A can be calculated with Beer-Lambert equation:

$$A = \log\left(\frac{I}{I_0}\right) = abc\,, \tag{4.2}$$

where a is absorptivity, b is the cell thickness and c is the concentration (used in the case of liquid samples).

FT-IR (Fourier Transform Infrared) Spectroscopy is a method where all frequencies are collected from the source simultaneously for pre-set period of time or given number of scans with predetermined durations. The infrared beam intensity is measured after it has passed through or was reflected from a sample. The resulting signal is called Interferogram. It possess the information about intensity for all frequencies present in the infrared beam. Interferogram is converted from a time domain to a

frequency domain signal by applying a Fourier transform, giving the Single Beam Spectrum. The signal from deposited layer is obtained with difference spectrum. It is ratio of modified sample to a reference spectrum of an untreated substrate.

In order to study molecules at the interface more precisely the Polarisation Modulated Infra-red Absorption Reflection Spectroscopy (PM-IRRAS) is used. This method uses parallel p- (Ep) and s-polarised (Es) light (Fig. 4.1).
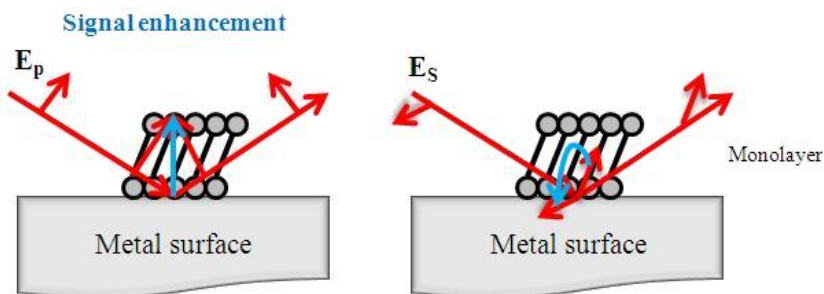
Figure 4.1: Reflection of p- and s-polarized IR light on the modified metal surface

At high angle of incidence, the p-polarised light absorbance is enhanced, while nearly no absorbance is observed from the s-polarised light. The former is used to obtain signal of the adsorbate layer, the latter as reference and a difference spectrum is extracted without a separate measurement of a reference sample.

In this work FT-IR and PM-IRRAS spectroscopy were used to analyse the adsorption of alkylthiols on gold as well as phosphonic acid on ZnO nanocrystalline surfaces. Measurements were performed with a Bruker Vertes 70 interferometer (Bruker, Germany) (PM-IRRAS) and FT-IR Nicolet 5700 (Thermo Fisher Scientific GmbH, Germany) at 78 reflection angle (VeeMAX II reflection cell, Pike Technologies, USA) at a resolution of 4 cm^{-1} with 512 scans.

4.3.3 Water contact angle studies

Water Contact Angle (WCA) is a method used to indicate hydrophilicity or hydrophobicity of the surface. The contact angle (θ) of a liquid droplet on substrate

depends on the surface tension at the solid/liquid (γ_{sl}), solid/air (γ_{sg}) and liquid/air (γ_{lg}) interfaces (Fig. 4.2).
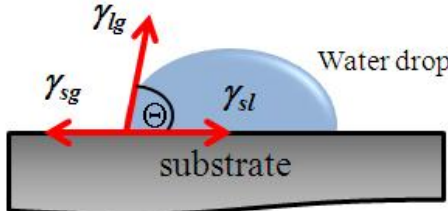
Figure 4.2: Water Contact Angle measurement.

The surface tension [mN/m] is equivalent to the surface energy, that needs to by supplied when a new surface is generated. Correlation between the contact angle (Θ) and the solid/air interface tension (γ_{sg}) is given by the Young's equation:

$$\gamma_{sg} = \gamma_{sl} + \gamma_{lg} \cos \Theta \,. \tag{4.3}$$

In this work WCA was measured on ZnO nanocrystalline films modified with alkylphosphonic acids. Measurements were performed with OCA 15 Plus (Dataphysics, Germany) before and after experiments (every resulted angle, in Tables 5.3 and 5.4, is a mean from 3 measurements in three different places on a sample surface).

4.3.4 Scanning Electron Microscopy (SEM)

The device enables precise surface analysis of condensed materials, by focusing electron beam on the sample. The beam interacts with a surface. Secondary and back-scattered electrons are used to scan sample features and their imaging. Based on the electron formation methods, two main classes of SEM can be distinguished. The most basic approach to generate an electron flux is to employ a hot cathode. In the more advanced Field Emission devices, cold or Schottky Field Emission are used [122] as electron generators. The electrons are thereafter accelerated with up to 50 kV through the vacuum column of the SEM and focused by means of electromagnetic lenses. The acceleration voltage influences the interaction area and depth

with the sample. These features depend also on the atomic number of the sample material.

The beam electrons interact with the sample surface. Electrons, which are emitted from the surface, are called secondary electrons. They are caused by inelastic interactions of electrons with the surface atoms. Other interactions lead to formation of Auger electrons and X-rays, which are not used by standard SEM.

Detection of the secondary electrons can be performed in chamber and in-lens detector. Chamber detectors have an Everthart-Thornley detector, where a grid with an applied voltage of -200 V to + 200 V is used to collect the electrons. The electrons hit scintillate counter and generate photons. Thereafter, the photons are amplified via a photomultiplier and the signal is converted into an electrical signal and is used to process the image. That is why, electrons with high and low energy yield lighter and darker (respectively) pixels in the image.

The other type of detector, the in-lens detector collects the electrons by an applied voltage as well. In this case, the electron detection is governed by a semi conductor. An electron-hole pair is formed as an electron hits the detector and an electric signal is generated. In lens detectors require a much smaller working distance and collect the electrons at the point of impact which leads to higher resolution in comparison to chamber detectors.

4.4 Calculation of interaction energy between poly-electrolyte modified TiO$_2$ nanocontainers and SAM covered gold substrate by means of DLVO Theory

A theoretical understanding of the interaction between the NCs and the SAM layer on gold surface can provide an insight into the mechanisms of the deposition behaviour. This can be achieved by the application of the DLVO theory [123–125] which allows the determination of the total interaction force between the PAH terminated NC particles and the carboxy terminated gold substrate surface as a function of the separation distance. These particular NC and monolayer types were chosen in Sec. 5.2 for QCM experiments with various values of ionic strength and pH.

In coagulation and/or deposition processes, the forces have origin in electrical double layer around the particle and surface (repulsive) and London - van der Waals forces (attractive) (Sec. 3.2.1.2). Total interaction energy (V_T) was determined by treating the quartz crystal-NC system as a sphere-plate interaction as has been previously outlined by a number of researchers [126–129]. Under this approach the London van der Waals interaction (V$_A$) can be determined from Hamakers integration [32, 130]:

$$V_A = \frac{A_H}{6} \left[\frac{R_{NC}}{D} + \frac{r_{NC}}{D + 2r_{NC}} + \ln \left(\frac{D}{D + 2r_{NC}} \right) \right], \qquad (4.4)$$

where A_H is the calculated Hamaker constant (in this case 2.2×10^{-21} F/m) for the Au-SAM PAH-NC system; r_{NC} average radius of the NC nanoparticles and D the distance of closest approach (both in meters).

The electrostatic double layer contribution (V$_R$) to the overall interaction energy can be calculated from the following equation [128]:

$$V_R = \pi \varepsilon_r \varepsilon_0 r_{NC} \left[(\psi_s^2 + \psi_p^2) \ln \left(\frac{\exp(2\kappa H_0) - 1}{\exp(2\kappa H_0)} \right) + 2\psi_s \psi_p \ln \left(\frac{\exp(2\kappa H_0) + 1}{\exp(2\kappa H_0) - 1} \right) \right],$$
$$(4.5)$$

where ε_r is the relative dielectric constant of water (80.1), ε_0 is the permittivity in vacuum (8.85×10^{-12}), r_{NC} average radius of the NC nanoparticles, κ the Debye-Hückel parameter, ψ_s and ψ_p the surface potentials for the nanocontainers (sphere) and QCM Au-SAM layer (plate) respectively. In this situation zeta potential values were used as the surface potential. The Debye-Hückel parameter κ is the inverse of the effective diffuse double layer thickness of Debye length [131]. It can be determined from (Sec. 3.2.1.1):

$$\kappa^{-1} = \left[\frac{\varepsilon_0 \varepsilon_r R T}{F^2 (\Sigma_i c_b^i z_i^2)} \right] , \tag{4.6}$$

where R is the universal gas constant, T temperature, F Faraday's constant, c_b bulk concentration of ion i and z_i charge number of ion i. The results of this calculations are presented in section: 5.2.2.3.

Chapter 5

Results and Discussion

5.1 QCM analysis of particle adsorption

5.1.1 Introduction

By specifically binding of colloidal particles to the surface of the QCM, positive shifts of frequency were observed, the Sauerbrey relation does not hold for this situation. A comparison of frequencies shifts and energy dissipation parameter on different overtones reveals a coupled resonance: at low overtones, Δf is negative, whereas it is positive at high overtones, with maximal resonance bandwidth observed at the cross over point. As predicted by the Dybwad model [28], the spheres bound to the surface form resonating systems on their own. A composite resonator is formed (Sec. 3.1.2.1), consisting of a large crystal with resonance frequency ω and the adsorbed spheres with resonance frequency ω_s (Fig. 3.6). In the case in which resonance frequency of the small spheres (firmly attached to crystal), ω_s, is higher than the resonance frequency of the crystal, ω, Δf of the composite system is negative (leading to the Sauerbrey limit). In the opposite limit (that is, in the case of large adsorbed particles bound to the sensor surface via a sufficiently weak bridge) Δf is positive. Such behaviour is known from sphere-plate contacts in the dry state. Finite element calculation demonstrates [23] that this phenomenon is

also plausible in liquid phase media, with Δf critically dependent on the strength of the sphere-plate contact. Operated in this mode, the QCM most likely probes the contact strength, rather than the mass of the particle.

5.1.2 Results and discussion

The quartz crystal microbalance worked in a non-gravimetric mode, by adsorption of TiO_2 particle agglomerates on SAM modified gold electrode, as frequency shift depend on overtone order. For that reasons it was impossible to convert the frequency shift, Δf, to adsorbed mass via the Sauerbrey equation. This was demonstrated by the fact that Δf frequently is positive on higher harmonics. Positive frequency shifts are characteristic of point-contacts between the resonator and the sample. If the particles under investigation are sufficiently large and rigid, they do not follow the motion of the crystal but rather, they are clamped in space by inertia and exert a restoring force onto the crystal via the contact. This restoring force increases the effective stiffness of the composite resonator, thereby increasing the resonance frequency, which is recorded as a positive frequency shift. The details of this point-contact type interaction are complicated and quantitative analysis of the frequency shift is unreliable unless the sample is well-characterised by other means. It has been demonstrated in other contexts, [132] that the bandwidth (energy dissipation) and its changes upon deposition is a more robust parameter in these situations. For instance, it always increases upon deposition (frequency may increase or decrease). Further, its positive shift is proportional to the number of adsorbed spheres. That is why, it is an empirical parameter, used to determine the progress of adsorption.

Fig. 5.1 shows results of an adsorption experiment on an amine-terminated gold surface and negatively charged aggregates of TiO_2 NCs (PSS-terminated, sec: 4.1).

Within the adsorption process, all values steadily increase in magnitude. At $t = 90$ min adsorption was stopped. Fig. 5.2a shows time-averaged values from Fig. 5.1
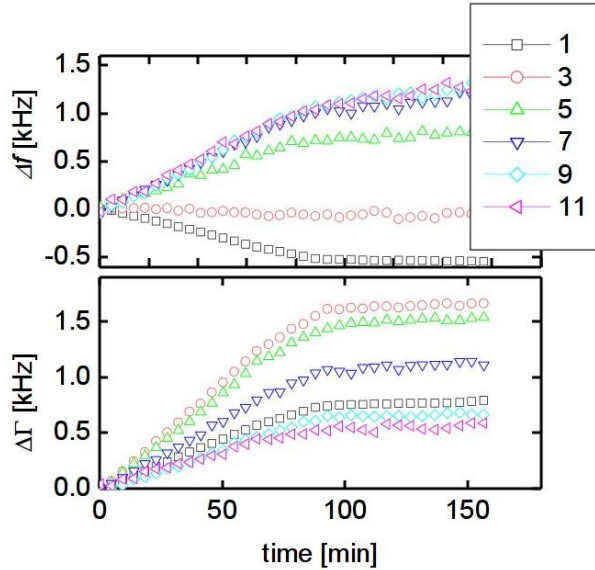
Figure 5.1: QCM data on adsorption of PSS-terminated NCs on SAM of aminothiol.

for $t > 90$ min versus overtone order n (that is, versus the operating frequency of the crystal).

Clearly, there is a coupled resonance (Sec. 3.1.2.1). Δf is negative at $n = 1$ and positive at $n > 3$. At the cross-over, the bandwidth shows a pronounced maximum. Fig. 5.2b shows analogous data for adsorption of a positively charged (PAH-terminated) TiO_2 NCs to a negatively charged surface (raw data: fig. 5.4a). The phenomenology is similar. As seen on the FE-SEM images (Figs. 3.5, 5.6 a, and c) the NCs always aggregated into larger units. The aggregates had a size in the micron range, which turned out to have tremendous effect on the set-up performance: the occurrence of positive Δf.

5.1.3 Conclusions

Adsorbing large diameter ($> 1\ \mu$m) colloidal objects to the surface of a quartz crystal microbalance, one can observe positive frequency shifts. As evidenced by a finite element calculation [23], these most likely arise from point contacts between the adsorbate particles and the sensor surface. The general phenomenology is similar as
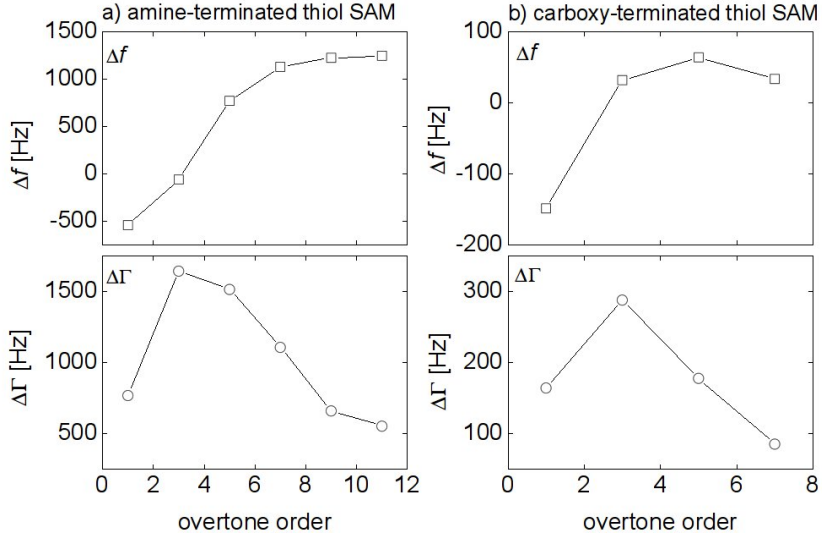
Figure 5.2: Time-averaged values of Δf and $\Delta \Gamma$, a)from Fig. 5.1 for $t > 90$ min (stationary state after end of the adsorption experiments). b) Second example of a coupled resonance for a similar system - adsorption of PAH-terminated NCs on carboxy terminated surface material.

for spheres in air, even though liquid leads to a strong coupling between the sphere and the plate. For such situations, the frequency shift depends on the stiffness of the contact, rather than on the size of the adsorbed object.

5.2 Adsorption of polyelectrolyte covered particles on SAM modified surfaces

5.2.1 Introduction

Self-healing coatings is a perspective method to protect metal against corrosion by means of incorporation of environmentally friendly inhibitors into a coating. These smart coatings should ideally release the inhibitor on demand and over prolonged time periods [133, 134]. Previous studies [77, 135–137] have shown that the direct introduction of a healing agent, particularly into a solgel matrix, leads to its deacti-

vation and the degradation of a polymer coating. In order to overcome this problem the inhibitor needs to be homogeneously isolated and entrapped within a coating matrix so that the release is only triggered by local changes in polymer medium (e.g. pH increases due to the corrosion processes) for a perfect self-healing performance. One of the possible solutions is to employ nanocontainers (NCs) covered with polyelectrolyte multilayers [120, 138] as inhibitor nano-reservoirs.

Layer-by-layer (LbL) deposition of oppositely charged weak polyelectrolytes on a desired substrate creates a well-defined system with regulated storage/release properties [53] in which the permeability of the container shell is determined by the balance of electrostatic interactions within the multilayer (Sec. 3.2.2.1). The pH changes due to the corrosion process are followed by ionisation of the weak polyelectrolytes of the functional groups, which results in increased repulsion between uncompensated charges [139]. To balance these charges small counter ions penetrate the layer structure and the resulting higher ionic concentration inside polyelectrolyte multilayers (i.e. inside the nanocontainer as compared to the surrounding solution) increases the osmotic pressure over the nanocontainer shell (extrinsic charge compensation: Sec. 3.2.2.1). The associated ingress of water into the polyelectrolyte multilayers causes swelling and leads to an opening of the pores releasing the inhibitor from NCs into the surrounding area [140]. Recently developed polymer coatings with NCs are usually adsorbed on self-assembled monolayer (SAM, Sec. 3.3) modified metal surfaces for a better adhesion [141].

These kinds of self-healing coatings have been studied intensively during the last decade and the research has mainly concentrated on coating and nanocontainer development. For example, Toohey et al. [142, 143] have studied bio-inspired microvascular coatings whilst several other methods, such as the use of self-organising block co-polymers [144], polypeptides [145], and nanodroplets [146], have also been investigated to entrap active materials. A review by Shchukin and Moewald [2] summarises the development of different nanocapsule components (via self-assembly, LbL), as well as self-healing polymers and pre-treatments. However, there is no full

understanding of the exact deposition mechanism of the nanocontainers within a coating even if the deposition of NCs is an essential step in the layer development: this step basically guides the nanocontainer distribution inside the matrix and thus it is directly related to the functionality of the coating. As such there is a clear need for studies with both experimental and theoretical aspects.

The purpose of this part of the work is to study the deposition of mesoporous TiO$_2$ nanocontainers on SAM-modified gold surfaces to gain more knowledge of the exact deposition methods of the coatings. QCM studies have been accompanied with DLVO theory calculations. This way, the control over the deposition process as a function of pH and salt concentration (ionic strength) of the solution is achieved. The adsorption process was followed in-situ by means of QCM and the morphology of the adsorbate was investigated by means of FE-SEM images taken of the substrates after each adsorption process. Deposition could be achieved if either the particles and the surface had opposite charge, or if the salt concentration was sufficiently high, reducing the repulsion between the spheres and the surface. In the latter case the adsorption kinetics could be explained in the context of the DLVO-theory. Using conditions of like charges, one has a tool to control the speed of deposition by means of ionic strength. However, interparticle aggregation and cluster deposition on the surface were observed at high ionic strength. Such conditions have to be avoided to obtain a uniform deposition of separated nanocontainers on the surface

5.2.2   Results and discussion

5.2.2.1   Effect of surface treatment on nanocontainer deposition

Homogeneous and well defined alkanethiol SAM can be easily prepared on gold (111) substrates due to a high affinity of thiol functional groups to the Au metal ([147], Sec. 3.3.1), hence bifunctional thiol molecules were used to modify the gold electrode surface on a quartz crystal to produce the desired surface charges. Treatment of the gold quartz crystals with SAM layers of either 1,11-aminoundecanethiol (AUT) or

15-mercaptopentadecanoic acid (MUA) gave rise to amino (-NH$_2$/NH$_3^+$) or carboxy (-COOH/-COO$^-$) terminated surfaces, respectively, the presence of which was confirmed by PM-IRRAS (Fig. 5.3). As can be seen from the results the characteristic peaks of functional groups of molecules can be observed in the range of 3000 to 3600 cm^{-1} for amine group (together with C-N-H deformation peak at 1615 cm^{-1}) and 1705 cm^{-1} for carboxylic group. In addition, peaks from the CH$_2$ symmetric and asymmetric stretching vibrations are seen in both the AUT and MUA treated surfaces, clearly demonstrating adsorption of organothiol molecules on the gold surface.
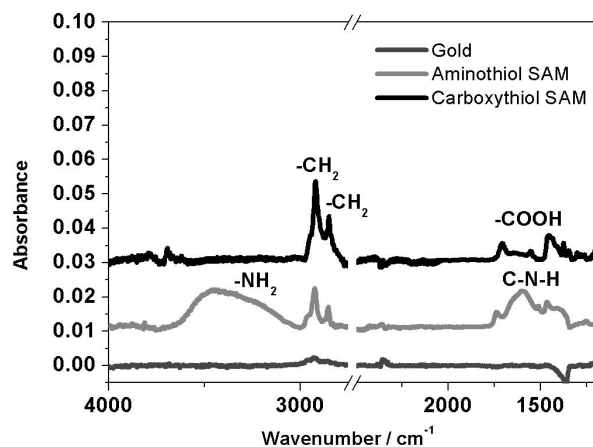
Figure 5.3: Infra-red spectra of gold surfaces with aminothiol and carboxythiol SAM, measured with PM-IRRAS.

Results on NCs adsorption monitored via QCM are displayed as energy dissipation parameter shift with time on several overtones. The meaning of the function $\Delta\Gamma$ versus overtone order is explained for this system in the previous chapter.

The results from Au surfaces coated with MUA on NCs adsorption are shown in Fig. 5.4(a,b). MUA coated surfaces are negatively charged at these experimental conditions (pH = 6) due to COOH/COO$^-$ equilibrium (carboxylic acid: pKa =$\sim$5.7 [148]). Poly(allyamine) hydrochloride (PAH-, Sec. 3.2.2.1) polyelectrolyte as the outer layer of the particles gives rise to positively charged NCs at pH of 6 and the QCM responded with significant positive shifts for all overtones measured

(from 1000 to 4500 Hz) with a stationary state reached after approx. 110 min (Fig. 5.4a). No further shifts were observed by rinsing confirming that the NCs layer formed during the adsorption process was stable. In contrast, the experiments involving polysodium 4-styrenesulfonate (PSS, Sec. 3.2.2.1) terminated NCs (negatively charged outer layer) displayed no discernable change in the measured $\Delta\Gamma$ even after 2 hours of measurement; indicating that no deposition had taken place (Fig. 5.4b).
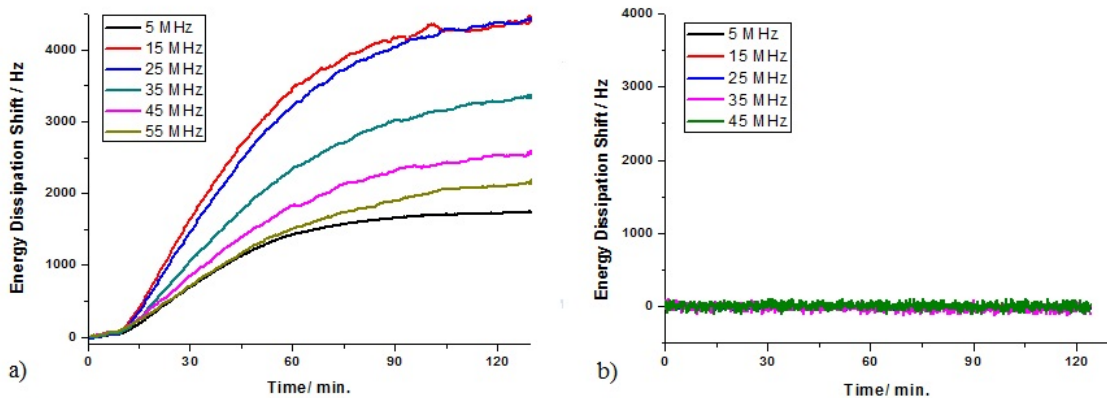
Figure 5.4: Energy dissipation shifts for adsorption process of PAH (part a) and PSS (part b) terminated NCs on gold surface with MUA SAM as a function of time (pH = 6).

QCM results for the second type of substrate - AUT on gold surface of quartz crystal i.e. positively charged substrate ($NH2/NH_3^+$) under the applied measurement conditions (pKa = 7.5 [23, 149]) - are displayed in Fig. 5.5 (a, b). In case of negatively charged PSS terminated NCs, positive bandwidth shifts were observed on all overtones from 400 to 1600 Hz and the adsorption process reached a stationary state within 90 min since the experiment starting (Fig. 5.5a). The final rinsing with water did not affect the bandwidth, once again showing the deposition of the NC layer was stable. In contrast, the repetition of the experiment with a positively charged PAH terminated NCs suspension had no measurable effect on any overtone even after 140 min (Fig. 5.5b).

From these results it can be clearly seen that after injection of the NCs, the band-
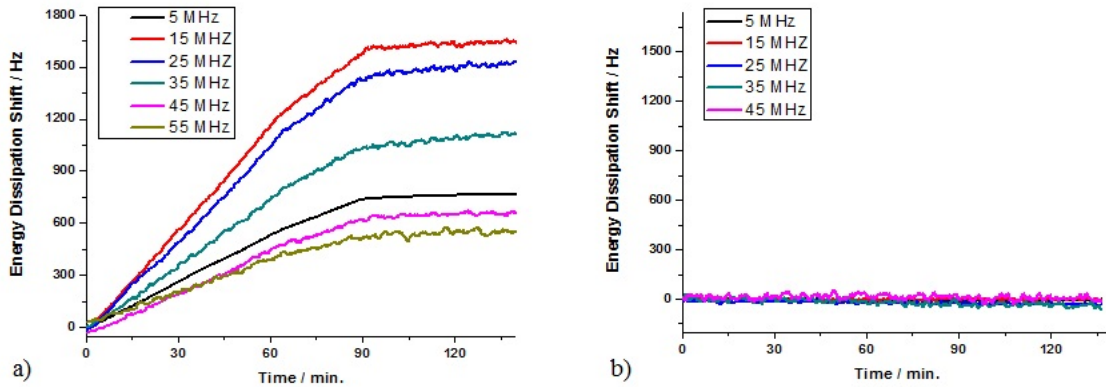
Figure 5.5: Energy dissipation shifts for adsorption process of PSS (part a) and PAH (part b) terminated NCs on gold surface with aminothiol SAM as a function of time (pH = 6).

width always increases if the substrate and particles have the opposite charge i.e. positively charged PAH terminated NCs on the MUA monolayer (COOH/COO$^-$) and negatively charged PSS-terminated NCs on AUT monolayer (NH$_2$/NH$_3^+$). When the monolayer on the Au surface and NCs have the same charge, as in the case of the PSS terminated NCs on MUA treated and PAH terminated NCs on AUT treated surfaces, no detectable shifts in bandwidth were observed. The level of frequency shifts measured was much more complicated, due to the coupled resonance ([23], Sec. 5.1). v

The results from the QCM experiments were confirmed by FE-SEM images of the quartz crystal surfaces taken after the experiments (Fig. 5.6 a-d) Both Figs. 5.6 a) and c) show surfaces after adsorption experiments, where NCs and substrate were oppositely charged; MUA on the substrate and PAH terminated NCs (Fig. 5.6 a), AUT treated substrate and PSS terminated NCs (Fig. 5.6 c). Both images show significant coverage of the quartz crystal surface by clusters of the respective NCs when compared to those in Fig. 5.6 b) and d) comprising of surfaces and NCs of the same charge (MUA surface and PSS terminated NCs, AUT surface and PAH terminated NCs). Moreover, there is a clear link between shifts in magnitude and
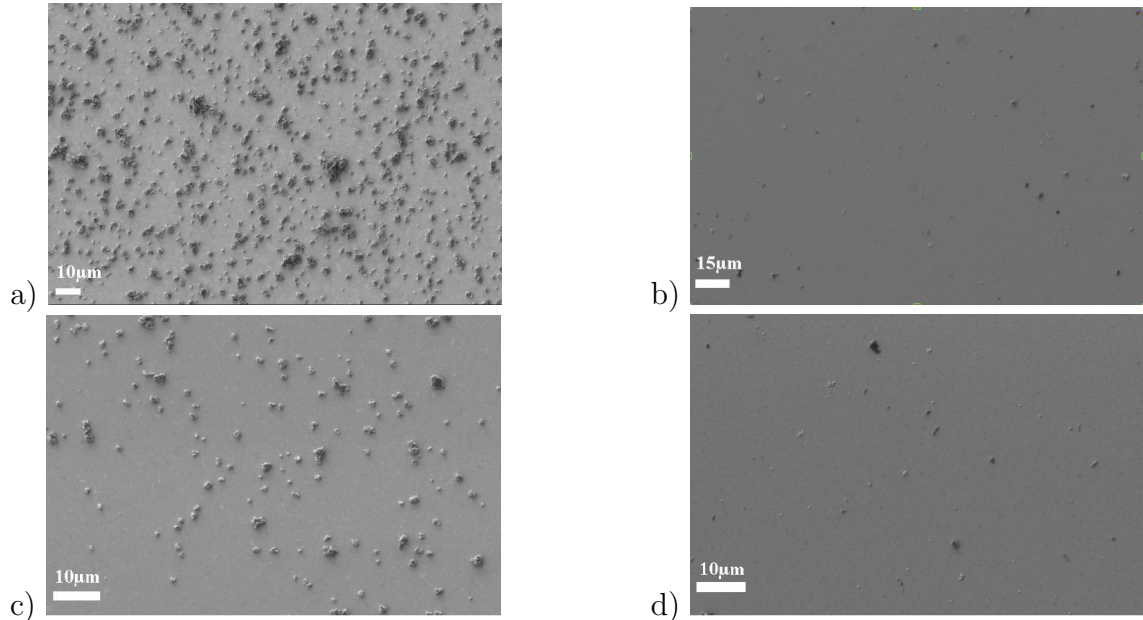
Figure 5.6: FE-SEM images of the quartz crystal active area with carboxythiol SAM +PAH terminated NCs (a), carboxythiol SAM + PSS-terminated NCs (b), aminothiol SAM + PSS-terminated NCs (c), aminothiol SAM+ PAH-terminated NCs (d) (pH = 6). Total experiment duration until QCM equilibrium $\sim$ two hours.

particle coverage: the larger shifts determined by QCM, the denser particle layer on the surface observed in FE-SEM.

5.2.2.2   Effect of salt concentration on nanocontainer deposition

For further investigation one model system was chosen to study of the influence of pH and ionic strength on adsorption process. The configuration composed of PAH terminated NCs and MUA treated substrate showed the best coverage in studied conditions (Fig. 5.6 a), i.e. positively charged particles (at near neutral conditions) on a negatively charged substrate. The underlying polyelctrolyte is negatively charged polyacrylic acid (PAA). This system was used for further studies (at pH = 9 and different salt concentrations).

The results are presented as energy dissipation shift of only one 3rd harmonic - 15 MHz for every value of KCl concentration at pH of 9 (Fig. 5.7) for simple
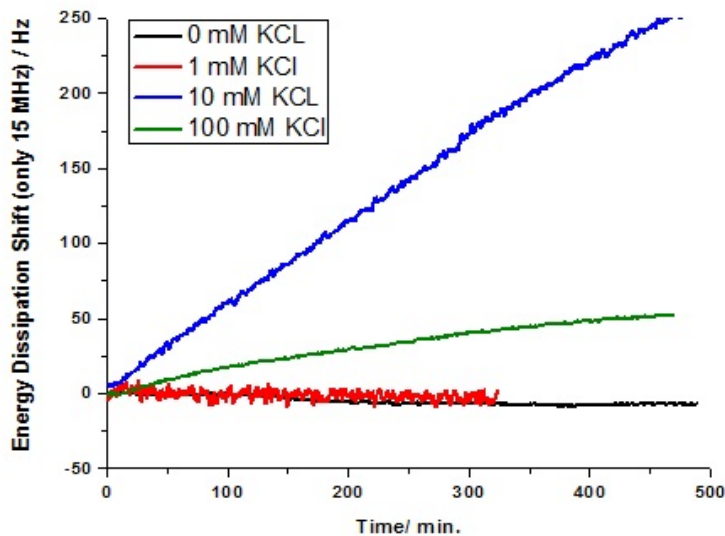
Figure 5.7: Energy dissipation shifts on 15 MHz overtone for adsorption process of PAH terminated NCs on gold surface with carboxythiol SAM as a function of time with different KCl concentrations (pH = 9).

comparison. FE-SEM images of the quartz crystal after the experiments are shown in Figs. 5.8 (a-e). The measured bandwidth shifts were very low (Fig. 5.7) for these 0 mM and 1 mM concentrations throughout the experiment indicating a lack of deposition, which was subsequently confirmed by FE-SEM images of the samples surfaces (Figs. 5.8 a, b). Further increase of KCl concentration led to far different behaviour with strong deposition observed at 10 mM KCl concentration (Fig. 5.7) and FE-SEM images of the sample revealed very dense particle coverage (Fig. 5.8 c, d). At the highest KCl concentration (100 mM) the adsorption process (Fig. 5.8 e) yielded an inhomogeneous layer of NCs agglomerates on the quartz crystal surface. At the beginning of each experiment the zeta potential of NCs was measured and the values are presented in Table 5.1, together with average size of the colloids. The zeta potential decreased with increasing ionic strength. PAH terminated particles had a strong negative charge at pH of 9. The charge was especially high at low salt concentration, where it reached:$\sim$ -50 mV (Table 5.1).

NCs surface is covered with two weak polyelectrolytes: PAA and PAH (Sec. 3.2.2.1),
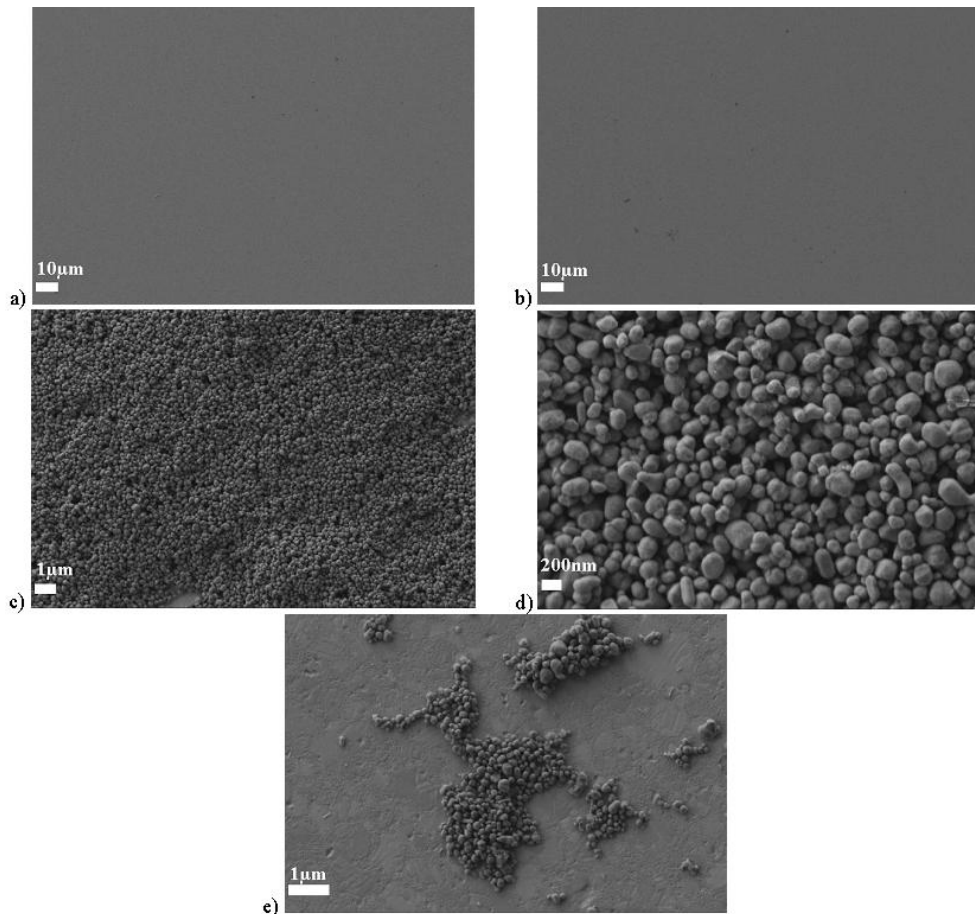
Figure 5.8: FE-SEM images of the quartz crystal active area with carboxythiol SAM +PAH terminated NCs (pH = 9) at the KCl concentration of: a) 0mM, b) 1mM, c), d) 10 mM, e) 100 mM. Total experiment duration until QCM equilibrium $\sim$ eight hours.

	pH 8.5 - 9; concentration of KCl			[mM]
	0	1	10	100
ζ_{pot} [mV]	-50.6	-51.3	-40.8	-24.0
NCs Size [nm]	220	320	580 (+ag.$\sim 5\mu$m)	480 (+ag. $\sim 5\mu$m)

Table 5.1: Zeta potential and average size of NCs within the series of measurements (pH = 9).

whose degree of ionisation strongly depends on bulk pH. At pH = 9. The degree of PAH ionisation is less than 50% in a solution and the multilayer structure of PAA and PAH enhances this effect by favouring the ionisation of PAA [150]. Therefore, the underlying PAA layer might effect the overall particle surface charge at high pH values. It could be the reason of the fact that the measured zeta potentials of PAH terminated NCs have such strong negative charge.

Complementary experiments at the pH = 6 were performed for the same configuration of NCs and substrate. The results are presented in Figs. 5.9 - 5.10 and Table 5.2.
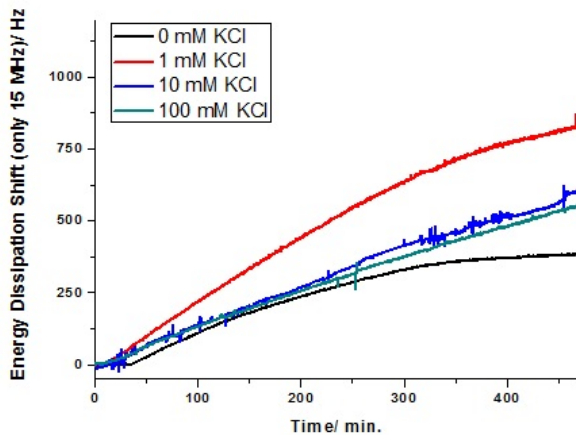
Figure 5.9: Energy dissipation shifts on 15 MHz overtone for adsorption process of PAH terminated NCs on gold surface with carboxythiol SAM as a function of time with different KCl concentration (pH = 6).

PAH terminated nanocontainers were positively charged within the whole measurement series. The Au surface (MUA modified) had rather stable negative charge within following values of I.

Adsorption process was detected by QCM (Fig. 5.9) and confirmed by FE-SEM (Fig. 5.10) showing that the deposition took place in a similar fashion at all salt concentrations (0 mM, 1 mM, 10 mM and 100 mM KCl).
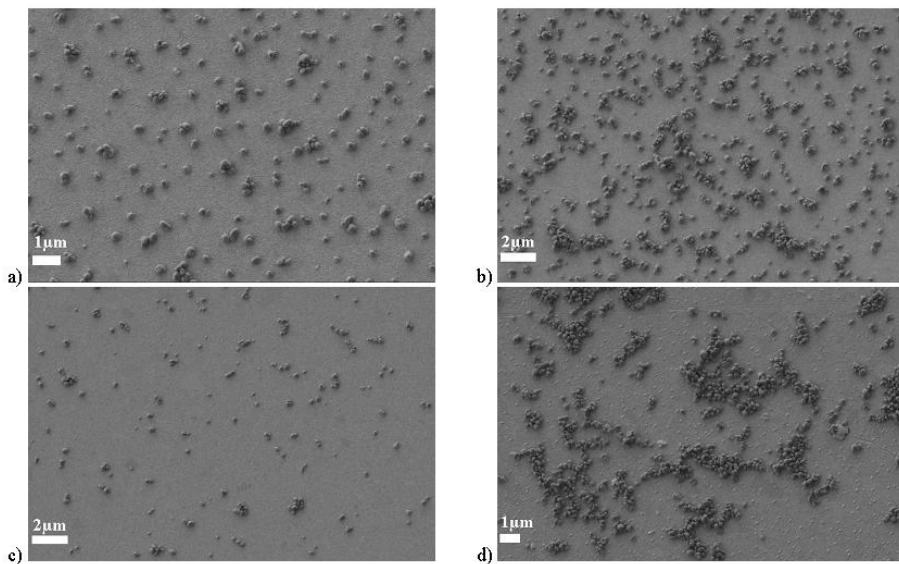
Figure 5.10: FE-SEM images of the quartz crystal active area with carboxythiol SAM +PAH terminated NCs (pH = 6) at the and KCl concentration of: a) 0 mM, b) 1 mM, c) 10 mM, d) 100 mM. Total experiment duration until QCM equilibrium ∼ eight hours.

	pH 6; concentration of KCl			[mM]
	0	1	10	100
ζ_{pot} [mV]	-36.3	-33.6	-29.5	7.47
Size [nm]	260	360	405 (+ag. ∼ 5μm)	730

Table 5.2: Zeta potential and average size of NCs within the series of measurements (pH = 6).

5.2.2.3 Application of DLVO theory: effect of pH and ionic strength

The experimental results of the effect of ionic strength and pH can be explained by using DLVO theory. The interaction forces between the PAH terminated NCs (positively charged at near neutral solutions) and MUA treated substrate (negatively charged) were calculated according to Eqs. (4.4-4.6, 4.4) for the 1 mM, 10 mM and 100 mM KCl solutions (pH = 9) and the results are introduced in Fig. 5.11. The surface potentials of NCs were assumed to be equal to the measured zeta potentials

while the surface potentials of the MUA treated Au substrate had been approximated by using literature values. For 1 mM KCl solution the zeta potential is -0.07 V at pH =9 [149]. For higher concentrations (i.e. 10 mM and 100 mM) the zeta potential values were not available in literature so they had to be approximated from the literature values at other concentrations [149]. Values -0.02 V and -0.001 V for 10 and 100 mM solutions (pH = 9), respectively, were considered as reasonable estimations. As a consequence, DLVO was utilised here as a method to analyse the relative changes in interaction energy and provide qualitative understanding of the deposition process rather than exact values for activation energy or deposition rates which are related to the interaction energy, therefore the results were plotted as dimensionless total interaction forces.
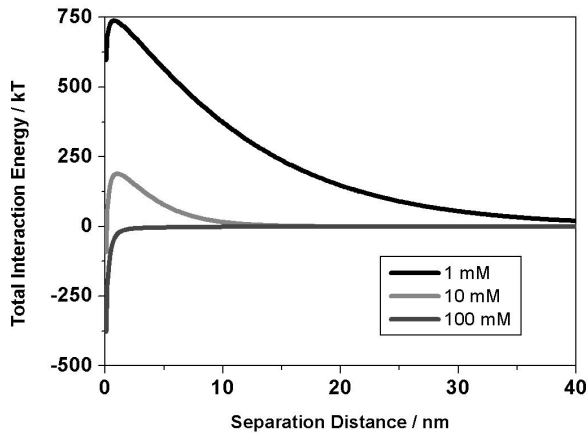
Figure 5.11: Dimensionless total interaction energy between the MUA coated gold quartz crystal and PAH terminated NCs at different concentrations of KCl solution (pH = 9).

The experiments at pH = 9 showed that no deposition is observed at low concentrations (0 mM and 1 mM KCl) while a relatively high amount is deposited at higher concentrations (Figs. 5.7 and 5.8) and this behaviour is also clear in the DLVO calculations (Fig. 5.11). The dimensionless interaction forces are positive over the whole separation distance (between the NC and Au surface) at the 1 mM salt concentration and it can be seen (qualitatively) that there is a high activation energy barrier to be overcome, i.e. the forces are repulsive and deposition cannot take place. In

the case of 100 mM KCl concentration, however, the forces are attractive over the whole separation distance, i.e. the deposition can take place. Different behaviour is observed for the 10 mM solution; the repulsive interaction forces are seen at high separation distances but when the separation distance is small the interaction forces become attractive. Additionally, the peak related to the activation energy is clearly smaller than in the case of 1 mM. Thus DLVO calculations are in good agreement with the experiments as the difference between the systems of 10 mM and the other concentrations can be observed both experimentally and theoretically (Figs. 5.7, 5.8). Hence it can be concluded that the activation energy results in the optimum deposition rate leading to more controlled deposition at 10 mM KCl solution at pH = 9.

In contrast when the system is at pH = 6, the DLVO calculations (Fig. 5.12) showed no repulsive forces over the whole separation distance as expected. Therefore, FE-SEM and QCM data are in the good agreement with these calculations (Figs. 5.9,5.10).
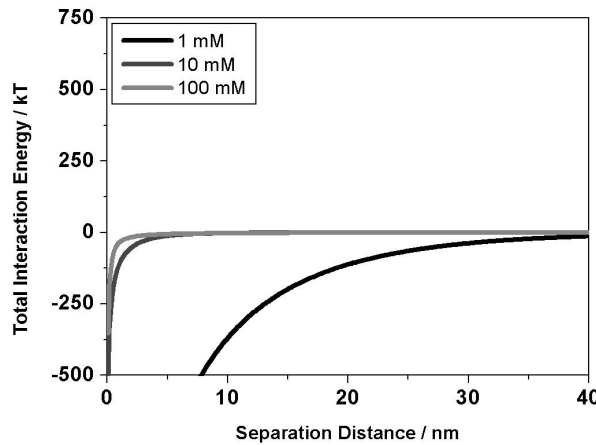
Figure 5.12: Dimensionless total interaction forces between the MUA coated gold quartz crystal and PAH terminated NCs at different concentrations of KCl solution (pH = 6).

Essentially, the effect of concentration on deposition process can be explained by the size of electrical double layer: when the ionic strength increases, the Debye length becomes smaller (Eq. 4.6), i.e. the double layer is thinner, and thus the

particle can approach the surface close enough that attractive van der Waals forces predominate and deposition can take place.

5.2.3 Conclusions

Studies on adsorption process of TiO_2 nancontainers covered with different polyelectrolyte multilayers could be performed in various pH and ionic strength values on SAM modified gold substrates by means of QCM. It was clearly demonstrated that the polyelectrolyte termination layer has a profound influence on the surface charge of the NCs and their subsequent adsorption kinetics on SAM modified gold coated quartz substrates. Containers with a positively charged surface (PAH terminated at neutral and acidic pH values) are seen to preferentially adsorb on a negatively charged carboxythiol SAM surfaces and not to adsorb on positively charged aminothiol SAM treated surfaces (that situation is repeated at pH of 9 and low ionic strength for the carboxythiol SAM surfaces). In contrast, the second type of investigated negatively charged (PSS terminated) NCs display opposite response at pH close to neutral. Moreover, it was shown that by adjustment of ionic strength, pH and zeta potential of NC suspensions, particle distribution can be controlled to achieve a desirable coverage. Monitoring the shift of bandwidth at different overtones enabled us to follow the adsorption kinetics and by combining these in-situ studies with ex-situ FE-SEM measurements after the deposition process even an estimation of the quantity of deposited nanocontainers became possible. Therefore, the application of QCM in a non-gravimetric mode proves to be of high value for the characterisation of particle adsorption processes on surfaces.

5.3 Modification of ZnO nanorods with organophosphonic acids: The effect of molecule alkyl chain length and solvent polarity.

5.3.1 Introduction

The synthesis and functionalization of ZnO based nanostructured materials has attracted a great amount of scientific and technical interest due to wide application possibilities in the fields of solar energy conversion, catalysis, microelectronics and anti-corrosion protection [13, 15, 151–154]. The anisotropic growth of ZnO nanocrystals along the c-axis of the hexagonal wurtzite structure allows the deposition of high aspect ratio crystallites, resulting in a significant increase of the active substrate surface area, which makes nanocrystalline ZnO films an ideal material for sensor applications [11, 155–158]. Furthermore, this substance is inert in corrosive environment and can be used as uniform oxide layer as an alternative to natural porous metal alloy cover [13]. Various low-temperature growth methods of nanocrystalline ZnO with excellent morphology control have been demonstrated on silicon, gold and other metal, metal oxide and polymer substrates [159–164].

Surface chemistry of ZnO nanorod films can be tuned by means of UV light irradiation or chemical modifications to improve their wetting properties or chemical sensitivity. Zhang et al., has demonstrated that UV illumination of ZnO films results in superhydrophilic sensing layers with high sensitivity and stability along with the reduction of the necessary sample volume for analysis due to improved wetting properties [165]. The chemical functionalization of ZnO films has been investigated with the aim of bio-sensing and biomolecular immobilisation by employing bi-functional linkers, where one functional group attaches to the metal oxide nanocrystals leaving a second one available for specific binding of bio-molecules [158, 166–170]. The immobilisation of uricase enzyme on ZnO nanorod films has been recently reported demonstrating a novel low-cost sensor device for the detection of uric acid with high

thermal stability and biocompatibility. The electrical properties of nanocrystalline ZnO film allowed a direct electron transfer between the uricase and the ZnO electrode, which enables an excellent selectivity and precision. Hydrothermally grown ZnO nanorods have been modified with glucose oxidase (GOx) by Wei et al. [167]. A great stabilisation of biological activity was observed due to the high specific surface area, as well as biomimetic and electrical properties of the ZnO substrate enabling a very fast response and high and reproducible selectivity as a glucose sensor.

Organophosphonic acids are promising candidates for chemical functionalization of ZnO nanorods and have been reported to form stable monolayers on various metal oxides [16, 141, 171–174]. In general, the main factors affecting the quality of an adsorbed monolayer are defined as the length of the alkyl chain, the concentration of the monomer and the polarity of the solvent [87, 175–177]. Zhang and coworkers have investigated the chemical surface functionalization of ZnO nanowires and ZnO (0001) single crystalline wafers with 3-Phosphonopropionic acid (3-PPA) and 10-Phosphonodecanoic acid (10-PDA). An increase of surface roughness was observed as well as inhomogeneous film formation in case of 3-PPA, which was attributed to the acidic etching of the ZnO wafer surface during the adsorption process [16]. Moreover, the morphology changes on single ZnO nanowires was analysed after the adsorption process. Severe and mild surface etching occurred for modification with 3-PPA and 10-PDA, respectively.

This chapter involves results on the investigation of molecule alkyl chain length and solvent polarity impact on the adsorption kinetics of monofunctional organophosphonic acid molecules (as primary work for adsorption of bi- functional molecules as adhesion promoters and bio-sensors) on ZnO nanorod surfaces, monitored by means of Quartz Crystal Microbalance (QCM). The structure and chemistry of the formed films has been characterised by means of Field Emission - Scanning Electron Microscopy (FE-SEM) and Fourier Transform - Infra Red Reflection Absorption Spectroscopy (FT-IRRAS), respectively. Water contact angle (WCA) measurements were performed supplementary to assess the quality of the surface functionalization.

5.3.2 Results and discussion

5.3.2.1 The effect of the chain length on the adsorption kinetics and the structure of the deposited films.

QCM experiments were performed to investigate the adsorption kinetics of methylalkylphosphonic acids $(CH_3\text{-}(CH_2)_n PO(OH)_2$, DPA:n=9, TDPA:n=13 and ODPA: n=17) on ZnO nanorod films. The interpretation of the QCM data acquired on such nanocrystalline surfaces cannot be performed based on the Sauerbrey equation [18] due to viscoelastic effects in the experiments. Thus, the frequency shifts observed during the adsorption process cannot be converted to the mass uptake. Therefore the discussion of the QCM data will be based on the time required for film completion and magnitude of the observed parameter shifts in 1 mM ethanolic solutions of DPA, TDPA and ODPA presented in figure 5.13 and table 5.3.
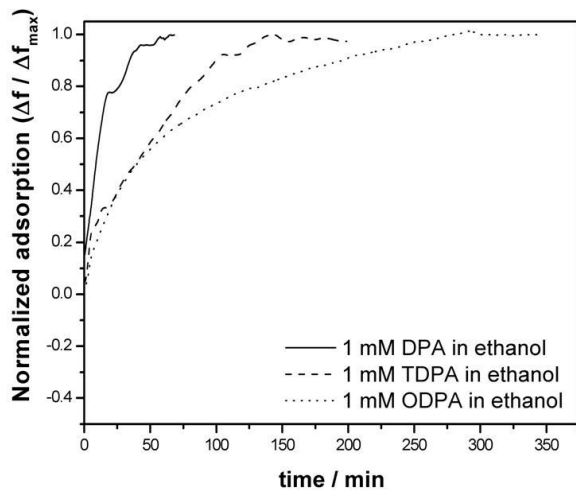
Figure 5.13: Normalized frequency shifts for adsorption process in 1 mM ethanolic solutions of: DPA, TDPA and ODPA on ZnO NR film.

The adsorption of DPA, TDPA and ODPA has resulted in frequency shifts of -22 Hz, -75 Hz and -150 Hz, respectively (Table 5.3). Frequency shifts of -22 to -28 Hz have been reported for n-octadecylthiol (ODT) adsorption on flat gold substrates using monomer solutions with different concentrations [87, 178]. Giza et al. [179]

reported a frequency shift of -5 Hz after adsorption of ODPA on plasma deposited aluminium surface. Even considering the increase in the surface area due to the nanorod morphology, the high negative frequency shifts observed with all three molecules indicate a complex film formation mechanism instead of a self assembly process. Comparison of normalised frequency shifts brings on deposition reaction kinetics as a function of chain length. The longer the chain the longer time is needed to reach equilibrium of the system
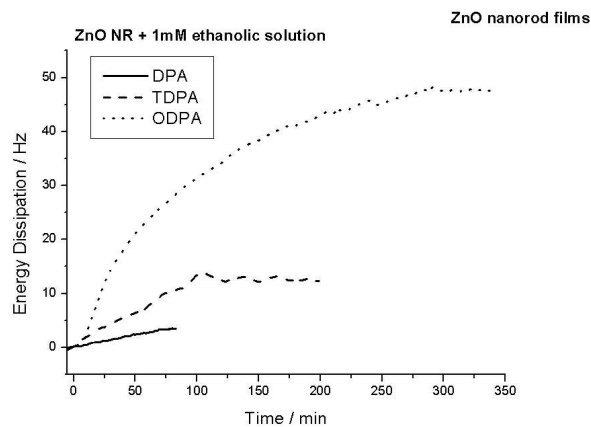
Figure 5.14: Energy Dissipation shifts for adsorption process from 1 mM ethanolic solutions of: DPA, TDPA and ODPA on ZnO NR film.

Energy dissipation shifts of 4 Hz, 13 Hz and 48 Hz were observed after adsorption of DPA, TDPA and ODPA on the ZnO nanorod film surface, respectively (Figure: 5.14, Table 5.3). In the literature, a high positive shift of the energy dissipation parameter is attributed to major viscoelastic deformations on the crystal surface [22, 24]. The FE-SEM images of the as-prepared substrate and adsorbed films are presented in figure 5.15 a-d, where the formation of a web-like adsorbate film was observed.

A solvent with a high dielectric constant, such as ethanol, provides a suitable environment for strong interaction between phosphonic acid and the ZnO nanorod substrate [180]. As described by Zhang and coworkers, the phosphonic acid moiety, can cause dissolution of ZnO due to its high acidity, even in non aqueous sol-
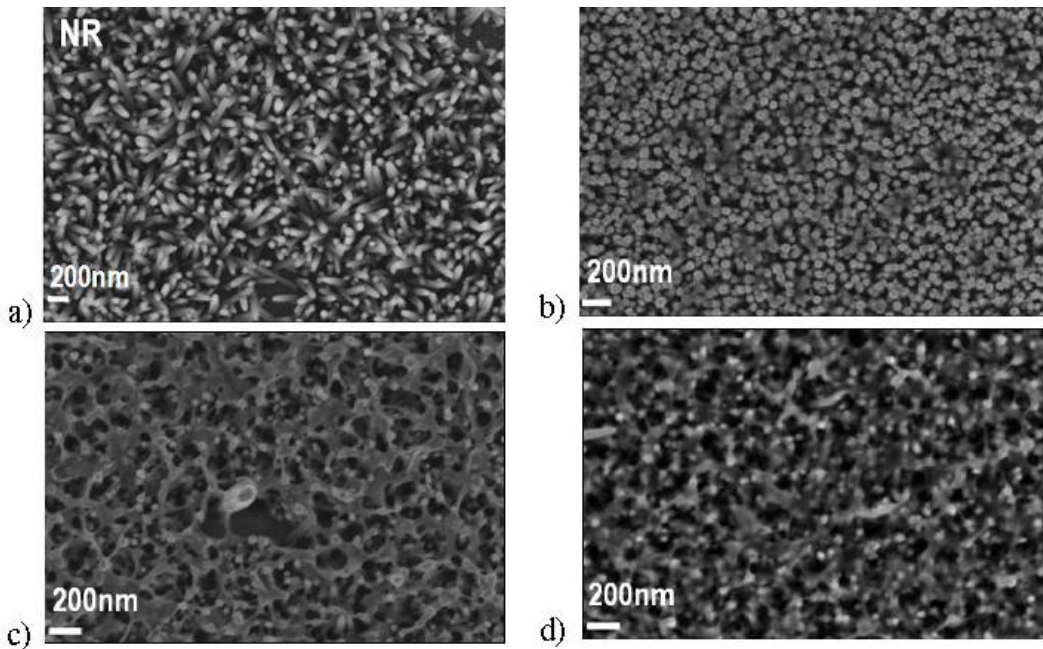
Figure 5.15: FE-SEM images of quartz crystal sensors modified with ZnO NR film a) and after QCM experiments with 1mM ethanolic solutions of b) DPA, c) TDPA and d) ODPA.

vents [16]. In the work of Taratula et al., less acidic phenylcarboxylic acids were compared with phenylphosphonic acids. A severe etching and formation of a white patina was observed with the latter [170]. Thus, the formation of the web-like structures can be explained by complex formation of the organophosphonic acid molecules and dissolved Zn^{2+} ions. Both dissolution and complexation reactions should have proceeded simultaneously leading to the deposition of thick adsorbate layers. This would cause the kinetic data obtained by means of QCM to be the combination of a positive shift due to the ZnO dissolution and a negative shift caused by the deposition of the complexed film. Observed aggregate formation of molecules (including a polar functional group and long non polar chain - typical surfactant structure) can be attributed to the reduction of the contact area of hydrophobic chains with surrounding polar solvent [182, 183]. The phenomenon is more severe with alkylchain length. FE-SEM images clearly show higher adsorbate agglomeration on TDPA and

ODPA modified surfaces (figure 5.15 c, d) in comparison to DPA (figure 5.15 b) coverage. Thick web-like structures accumulation is a source of deposition kinetics change. DPA molecule creates a smooth film on NR in less than one hour (figure 5.13). Time required for complete layer deposition is around three and five hours in the case of TDPA and ODPA, respectively.

FT-IRRAS and WCA measurements were performed to assess the surface chemistry of the organophosphonic acid treated ZnO nanorod films. The WCA of the as-prepared ZnO nanorod film was 64° and after adsorption of organophosphonic acids the contact angle increased to values above 120° for all three molecules (Table 5.3).

Substrate:	ZnO NR	ZnO NR+ DPA	ZnO NR+ TDPA	ZnO NR+ ODPA
Δf_{max} (Hz)	-	-22	-75	-150
$\Delta \Gamma f_{max}$ (Hz)	-	4	13	48
WCA (^{o})	64	126	125	129

Table 5.3: Shifts of frequency, dissipation and Water Contact Angle on quartz crystal sensors modified with ZnO NR film after QCM adsorption experiments with 1mM akylphosphonic acids ethanolic solutions.

Figure 5.16 presents FT-IR spectra of quartz crystal sensors modified with ZnO NR film after QCM experiment with 1mM ethanolic solution: of DPA, TDPA and ODPA (as-prepared ZnO NR film was used as reference for the computation of the absorbance spectrum).

Peaks assigned to asymmetric and symmetric $-CH_2$ vibrations were observed at 2917 and 2849 cm^{-1}, respectively. The peak at the 2958 cm^{-1} can be attributed to the asymmetric $-CH_3$ vibration peak. The peak belonging to the symmetric stretching of $-CH_3$ was under the shoulder of the $-CH_2$ asymmetric stretching peak and could not be resolved. A proper analysis of peak ratio concerning a self-assembly process was not possible due to the morphology of the ZnO substrates as
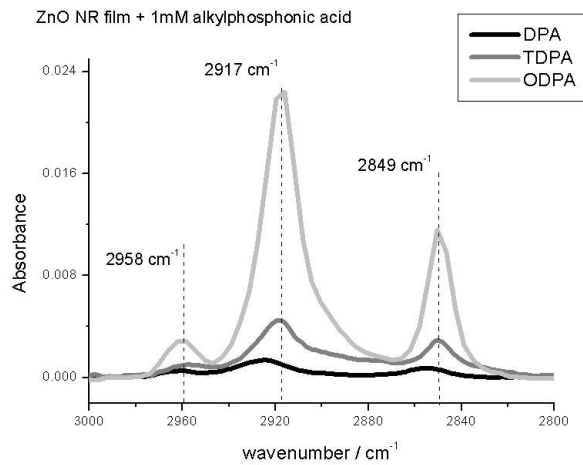
Figure 5.16: FT-IR spectra of quartz crystal sensors modified with ZnO NR film after QCM experiment with 1mM ethanolic solution: of DPA, TDPA and ODPA. (as-prepared ZnO NR film was used as reference for the computation of the absorbance spectrum).

well as complexity of the adsorbed films. However, the increase in the intensities as well as slight shift of the peak position to lower wavenumber values confirmed the formation of thicker adsorbate layers and higher molecular organisation [92] with longer chain length as observed in the QCM and FE-SEM results.

5.3.2.2 Influence of solvent polarity on ODPA adsorption.

Three different solvents have been employed to investigate the adsorption of ODPA molecules on ZnO nanorod films as a function of dielectric constant of the solvent. Adsorption experiments were performed from 1 mM solution of ODPA in ethanol (ε = 24.55), isopropanol ($\varepsilon = 18$) and from a mixture of ethanol and chloroform (1:1, $\varepsilon \approx 14.7$) [181].

As seen in figures 5.17, 5.18, the QCM data revealed a correlation between solvent polarity and adsorption kinetics. The mixture of chloroform and ethanol (1:1) provided a rather fast equilibrium, as plateau was reached within approximately one hour after the introduction of ODPA. The adsorption process was completed after nearly two hours in isopropanol and after more than three hours in ethanol.
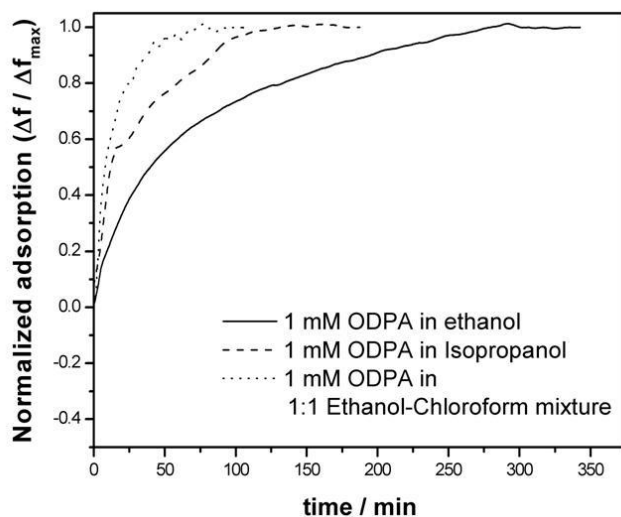
Figure 5.17: Normalized frequency shifts for adsorption process from 1mM solution of ODPA on ZnO NR film in ethanol, isopropanol and mixture of ethanol with chloroform.

As discussed before, the QCM adsorption data contains the contributions of simultaneous ZnO dissolution and film formation processes. The adsorption of an ODPA layer or the complex Zn-ODPA film should form a protective barrier on the substrate and hinder the ZnO dissolution. The kinetic data presented in figure 5.17, indicates that such a protective film was achieved in the 1:1 ethanol-chloroform mixture in a much faster way and further dissolution of ZnO was prevented leading to the formation of a stable protective film. FE-SEM images of the adsorbates formed in isopropanol and 1:1 ethanol-chloroform mixture 5.19 have indicated creation of the much thinner web-like precipitation films (single "webs" are indicated with white ellipse on the figure 5.19) in contrary to adsorption experiments from ethanolic solution 5.15 d. The reports on the self-assembly of organothiol monolayers on gold surfaces have demonstrated that the order of SAMs formed on gold depends strongly on the selection of the solvent employed in the adsorption experiments [184, 185]. Similarly, numerous articles have shown that a equivalent effect was observed on oxide surfaces [180, 186–189].

The FT-IR spectra of the adsorbate films deposited from solvents with different
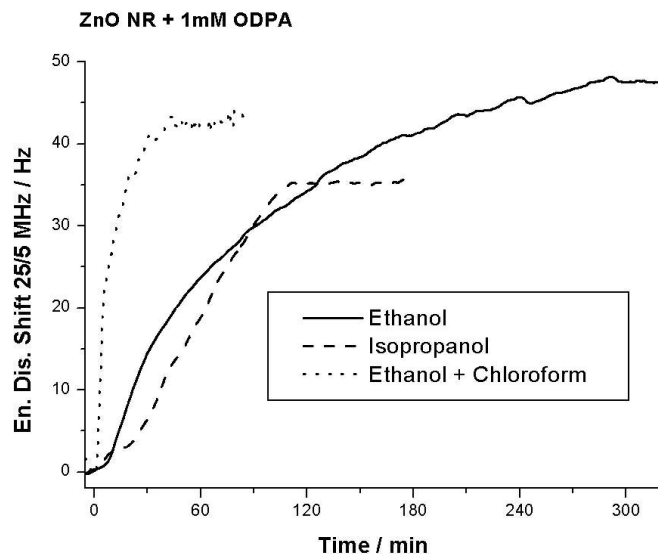
Figure 5.18: Energy Dissipation shifts for adsorption process from 1mM solution of ODPA on ZnO NR film in ethanol, isopropanol and mixture of ethanol with chloroform.

dielectric constants are presented in figure 5.20. The increase in the peak intensities of $-CH_2$ vibrations agreed well with the QCMdata.The higher solvent polarity, the thicker adsorbate layer. As discussed previously, an analysis of peak ratios was not performed due to the complex substrate morphology.

Static water contact angle measurements were performed on the ODPA modi-
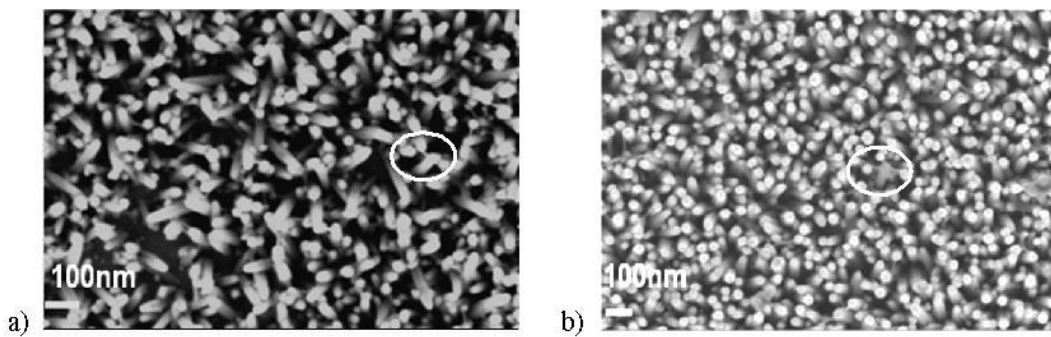
Figure 5.19: FE-SEM images of quartz crystal sensors modified with ZnO NR film and after QCM experiments with 1 mM ethanolic solution of ODPA in a) isopropanol, b) ethanol/chloroform.
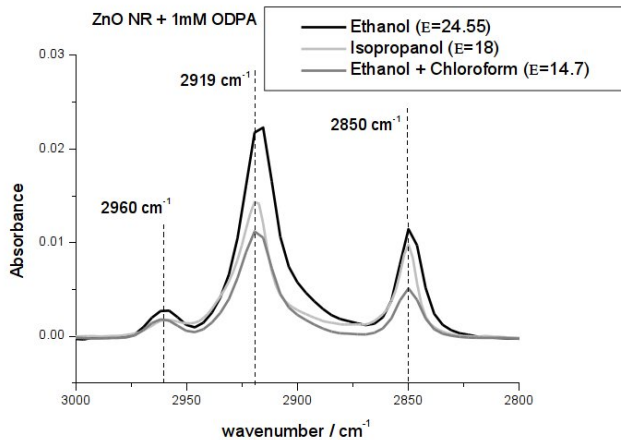
Figure 5.20: FT-IR spectra of quartz crystal sensors modified with ZnO NR film after QCM experiment with 1mM solution of ODPA film in ethanol, isopropanol and mixture of ethanol with chloroform(1:1).

fied ZnO nanorod substrates (table 5.4). Adsorption of ODPA films from all three solvents resulted in hydrophobization of the ZnO nanorod film surface.

Solvent:	Ethanol/Chloroform (1:1)	Isopropanol	Ethanol
Dielectric Const. (ε)	~ 14.7	18	24.55
Δf_{max} (Hz)	-98	-84	-144
$\Delta\Gamma f_{max}$ (Hz)	42	35	48
WCA (^{o})	174	150	129

Table 5.4: Water Contact Angle (WCA) on quartz crystal sensors modified with ZnO NR film after QCM adsorption experiments with 1 mM ODPA solutions.

A direct correlation was observed between the dielectric constant of the adsorption medium and the hydrophobicity of the ODPA modified ZnO nanrod substrate. The static WCA increased to 150° for films formed in isopropanol and an ultrahydrophobic surface with a WCA of 174° was obtained after ODPA adsorption from

1:1 ethanol-chloroform mixture. This effect could be explained with the formation of ordered ODPA monolayers with an excellent coverage from solvents of lower polarity due to the strengthening of the intramolecular chain-chain interactions and suppression of the acidity of the phosphonic acid moiety preventing the ZnO dissolution.

5.3.3 Conclusions

The effect of molecule chain length and solvent polarity on the adsorption kinetics of monofunctional phosphonic acids on ZnO nanorod films was investigated by means of quartz crystal microbalance measurements. Complementary FE-SEM, FT-IRRAS and static contact angle measurements were performed to investigate the chemistry and structure of the adsorbate films. Alkyl chain length of the monofunctional phosphonic acid molecule has a profound impact on quality of the adsorbate film in ethanol. Significant aggregate formation between nanorods was observed only by molecules with long non polar chain- species (> 10 methyl groups). The phenomena can be explained by reduction of the contact area of non polar hydrophobic chains with surrounding polar solvent. Adsorption of organophosphonic acids from ethanolic solutions led to film precipitation due to the ZnO dissolution and the complex formation of phosphonic acids with zinc ions. By the use of solvents of lower dielectric constant, the ZnO dissolution was hindered and formation of agglomerate layers was prevented, resulting in the deposition of ordered mololayer films. After the adsorption of ODPA from 1:1 mixture of ethanol and chloroform the surface became ultrahydrophobic indicating the assembly of an excellent protective barrier film.

5.4 Functionalization of ZnO continuous nanocrystalline films with alkylphosphonic acids: The effect of substrate morphology and bulk Zn^{2+} ion concentration.

5.4.1 Introduction

The influence of surface morphology as well as additional bulk zinc ions were investigated as complementary work to the previously presented data on functionalization process of ZnO nanorod films by means of alkyl phosphonic acids (section: 5.3). The impact of surface stability, changed via crystal morphology, was examined by means of QCM adsorption experiments on ZnO continuous nanocrystalline films. The new form of metal oxide layers was obtained via addition of growth promoter along hydrothermal synthesis. The substance changes the crystal growth direction, leading to formation of hexagonal nanoplates instead of nanorods. In such surface topography, the aspect ratio of the exposed crystallographic surfaces is changed in the favour of the polar and less stable (0001) orientation. This substrate modification appeared to have significant effect on interface phenomena along alkylphosphonic acids adsorption. ZnO nanoplates seemed to be more sensitive to organic phosphonic acids in comparison to nanorods leading to enhancement of reactions described in the previous section: deposition of precipitation films due to the ZnO dissolution and the complex formation between zinc ion and phosphonic acid. Therefore, continuous nanocrystalline films were chosen as substrates for studying reaction mechanism of functionalization via alkylphosphonic acid. Increased ZnO dissolution was simulated via implementation of zinc ions into 1mM ethanolic ODPA solution. QCM, FE- SEM and FT-IR data obtained from experiments with various amount of additional Zn^{2+} ions suggested that creation of complexes with phosphonic acid in the bulk medium generates possible inhibition of agglomerate accumulation in the

interface area. The results provided a better insight into ZnO nanocrystalline surface modification reaction via alkyl phosphonic acids. The data are promising since uniform functionalization of ZnO crystals (nanorod and continuous films) appeared to be possible via addition of bulk zinc ions.

5.4.2 Results and discussion

5.4.2.1 Effect of substrate morphology.

Adsorption of organophosphonic acids with two different chain lengths was performed on ZnO continuous nanocrystalline films as complementary data to experiments on ZnO nanorods, presented in subchapter 5.3.2.1. The following molecules $CH_3(CH_2)_n PO(OH)_2$: TDPA: n=13 and ODPA: n=17 were deposited on substrates made of hexagonal ZnO nanoplates from 1mM ethanolic solutions.

It is reported in the literature that the free surfaces of the deposited ZnO nanocrystals have the polar ZnO and non polar ZnO orientations [15] (chapter: 3.4). The low-symmetry non polar face is stable with threefold-coordinated atoms, whereas the polar plane is energetically unfavourable [190]. The fastest growth rate of ZnO is along the c axis due to the higher surface energy under thermodynamic equilibrium conditions leading to the formation of nanorods (with polar tip (0001) and non polar (10-10) walls). The growth promoter sodium citrate, added to hydrothermal synthesis solution, changes the growth direction. Citrate ions adsorb preferentially on the (0001) polar surface [191]. Hence, crystal growth is inhibited along c axis, but metal oxide is still able to grow in the form of thin polar plates with non polar (10-10) rims. The ZnO morphology evolves from a one-dimensional nanorod to a two-dimensional nanoplate. The aspect ratio (height to width) decrease is directly related to the citrate ion concentration, providing simple approach of morphology control [191]. The ZnO nanorods become shorter in length and larger in diameter with small addition of citrate ions to the hydrothermal synthesis solution. In the frame of this work concentration of added growth promoter was 6mg/ 100

mL (for hydrothermal synthesis bath with zinc nitrate and hexamethylenetetramine at the concentration 1: 1 of 0.05M) delivering crystals as seen on the figure: 5.23 a. Deposition of nanoplates induces change in the ratio of the exposed crystallographic surfaces in the favour of the (0001) orientation. Hence, morphological modification can affect the surface functionalization process. Adsorption of alkylphosphonic acids from ethanolic solutions resulted in the formation of web-like precipitation films on NR substrates due to the ZnO dissolution and the complex formation of organic acids with zinc ions (chapter 5.3). The phenomenon gets more severe with increasing alkyl chain length. The longer the molecule, the longer the time required for the completion of adsorbate film owing to accumulation of hydrophobic agglomerates between NR tips. In this section, impact of surface stability (changed via crystal morphology) on those interfacial phenomena is investigated.
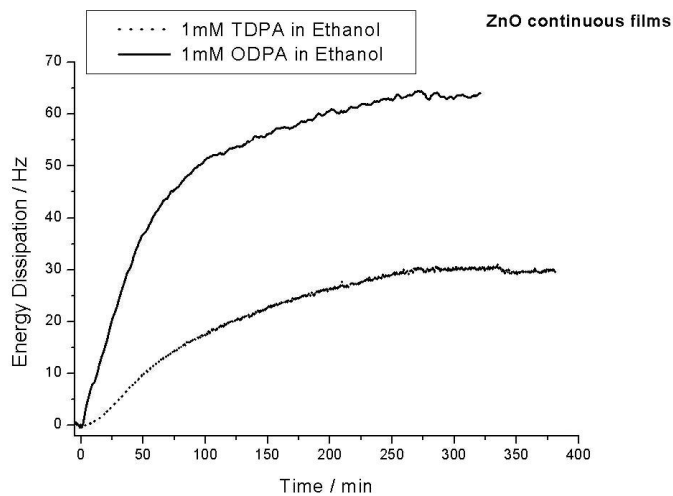
Figure 5.21: Energy Dissipation shifts for adsorption process from 1mM ethanolic solutions of: TDPA and ODPA on ZnO continuous film.

Complex film formation caused significant shifts of frequency and energy dissipation parameters (table 5.5) during organic phosphonic acids adsorption experiments on ZnO continuous nanocrystalline films (figure: 5.21). Therefore, QCM worked in a non-gravimetric mode providing information about reaction kinetics and viscoelastic damping but not actual adsorbate mass (chapter: 3.1)
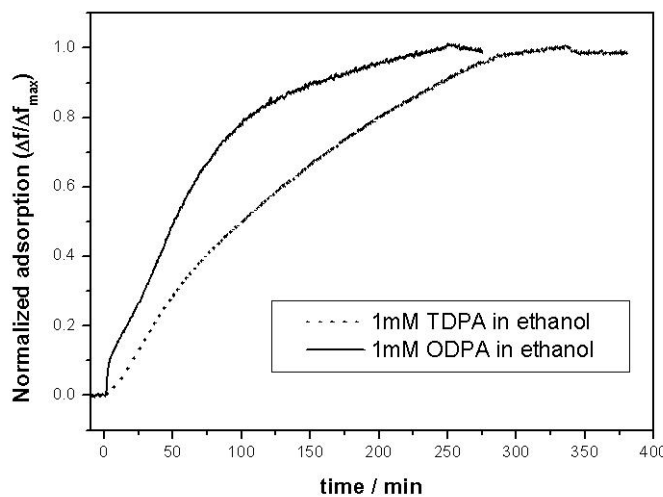
Figure 5.22: Normalized frequency shifts for adsorption process from 1mM ethanolic solutions of: TDPA and ODPA on ZnO continuous film.

[192,193]. Adsorption kinetics as a function of alkylphosphonic acid chain length in ethanol are displayed as frequency shift divided by maximum frequency change with reaction time [figure: 5.22]. Comparison of normalized frequency shifts on ZnO continuous films did not reveal the same correlation to molecular chain length as in the case of nanorods.

Deposition of organic species on ZnO continuous nanocrystalline films resulted in the following frequency and energy dissipation parameters: TDPA: Δf= -195 Hz, $\Delta\Gamma$= 30 Hz, ODPA: Δf= -290 Hz, $\Delta\Gamma$= 64 Hz (table: 5.5). Their magnitude increases with alkyl chain length, whereas the stabilisation was reached faster for the phosphonic acid with longer alkyl chain (6h-TDPA, 4h-ODPA).

The formation of the TDPA film required the longest period of time on continuous nanocrystalline substrate. The FE-SEM image of TDPA sample indicated major surface modification, strong crystal dissolution and complex film deposition [figure: 5.23 b]. The crystalline surface was homogenously affected by ODPA as well as crystals rims are not sharp and surface is visibly capped with adsorbate layer [figure: 5.23 c].

The QCM adsorption data contains contributions of simultaneous ZnO dissolu-

Substrate:	ZnO cont.+ TDPA	ZnO cont.+ ODPA
Δf_{max} (Hz)	-195	-290
$\Delta \Gamma f_{max}$ (Hz)	30	64

Table 5.5: Shifts of frequency and dissipation on quartz crystal sensors modified with ZnO cont. film after QCM adsorption experiments with 1mM akylphosphonic acids ethanolic solutions.
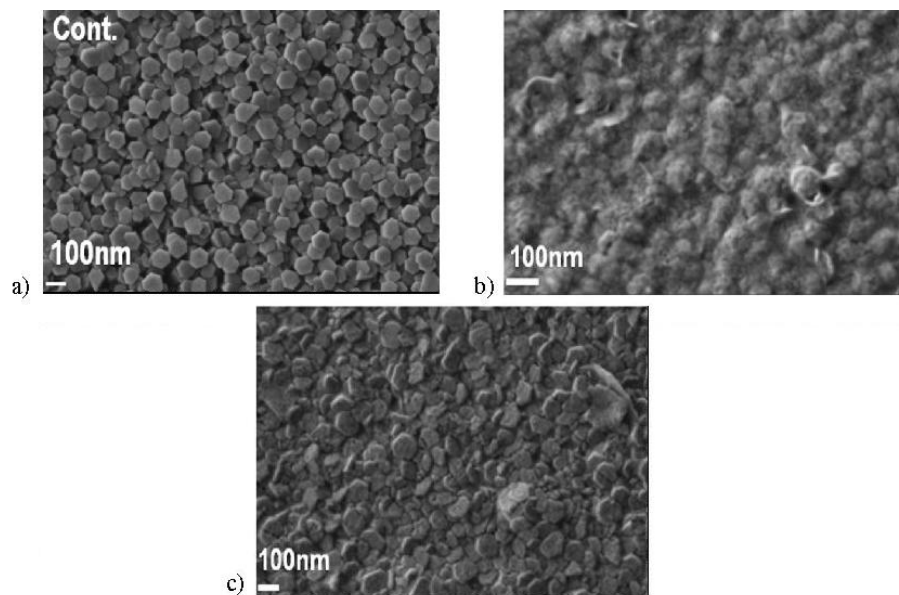

Figure 5.23: FE-SEM images of quartz crystal sensors modified with ZnO continuous film a) and after QCM experiments with 1mM ethanolic solutions of b) TDPA, c) ODPA.

tion and Zinc-phosphonic acid complex precipitation. Zinc ions are believed to be released from less stable polar planes. In the case of high aspect ratio NR films, the substrate dissolution could have occurred mostly on the rod tips and thus agglomerates were formed in between them (figure 5.15 c, d). The reaction kinetics was influenced by molecular chain length. Such relation is no longer valid for continuous films, where metal oxide dissolution appears nearly on the whole surface, since only non polar nanoplate rims are stable [190, 191]. Furthermore, the general trend is that the acid strength diminish with the alkyl chain length [194]. Shorter TDPA

as stronger acid could have induced much more severe crystal dissolution in comparison to ODPA. FE-SEM images support this explanation. Interactions of ZnO continuous nanocrystalline film with TDPA resulted in almost complete surface flattening [**??** b]. QCM data for that system generated shifts of frequency and energy dissipation smaller than for the longer molecule, suggesting some mass increase but not high viscoelastic damping since formed soft complex adsorbate did not increase the sample thickness (due to major substrate dissolution). ODPA as weaker acid (due to longer alkyl chain length) could have prevented partially the dissolution and contributed to accelerated detection of the plateau. Adsorbate film appears to form a complete coverage layer, inhibiting further metal oxide dissolution. Therefore, it can be assumed that the molecule adsorption brought on higher parameters shifts (then TDPA) probably as a result of lower ZnO dissolution.

Figure 5.24 presents FT-IR spectra of quartz crystal sensors modified with ZnO nanocrystalline continuous film after QCM experiments with 1mM ethanolic solution of TDPA and ODPA (as-prepared ZnO nanocrystalline films were used as reference for the absorbance spectrum calculations). The following bands could be resolved in the spectra: peaks at 2917 and 2848 cm^{-1} attributed to asymmetric and symmetric $-CH_2$ vibrations, respectively and the assymetric $-CH_3$ vibrations at the 2958 cm^{-1}. Molecular chain self-assembly detection was not possible by means of peak position analysis due to the morphology of the ZnO substrates as well as complexity of the deposited films. Comparison of band intensities confirmed thicker coverage in the case of ODPA which is in agreement with the QCM and FE-SEM data.

The results indicate that the mechanism of surface functionalization via alkylphosphonic acids of ZnO nanocrystalline films depends on substrate morphology and stability. ZnO continuous films with larger exposed (0001) planes are more sensitive to organic phosphonic acid in comparison to nanorod films, where favourable non polar phase has larger surface area. The mechanism of interaction between phosphonic acid and nanocrystalline ZnO will be deeper investigated in the next section.
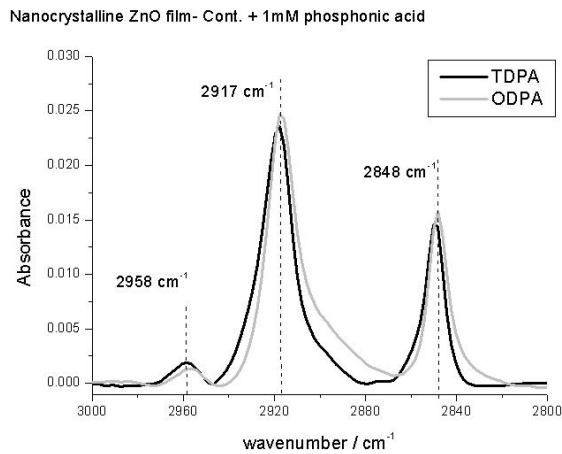
Figure 5.24: FT-IR spectra of quartz crystal sensors modified with ZnO continuous film after QCM experiment with 1mM ethanolic solution of TDPA and ODPA.

5.4.2.2 Influence of bulk Zn^{2+} ions concentration on ODPA adsorption.

According to numerous reports, zinc ions create complexes with phosphonic acid functional molecules. The phenomenon was used in liquid-liquid Zn^{2+} extraction technology by means of bi-functional organophosphorus species [195] as well as to slow down the growth rate of ZnO nanoparticles, by adsorbing on their surface and providing a barrier for further precipitation [196].

The partial dissolution of Zn^{2+} ions from the substrate (especially from the less stable polar(0001) ZnO orientation) triggered by phosphonic acid could be the reason for formation of significant adsorbate layer on ZnO continuous nanocrystalline films [figure: 5.23]. Dissolved metal ions are believed to create complexes along deposition of phosphonic acid molecules. Thus, the metal ions stay in the interfacial area as a part of precipitation films. In order to verify this assumption, two ODPA adsorption experiments with additional amount of Zn^{2+} ions (1 mM and 0.1 mM) in the bulk were performed. Zn Acetate was added in appropriate amounts to 1 mM ODPA ethanolic solutions. The QCM experiments were conduct in the same conditions as in the previous sections.

Figure 5.25 display comparison of the QCM output for 1 mM ODPA adsorption
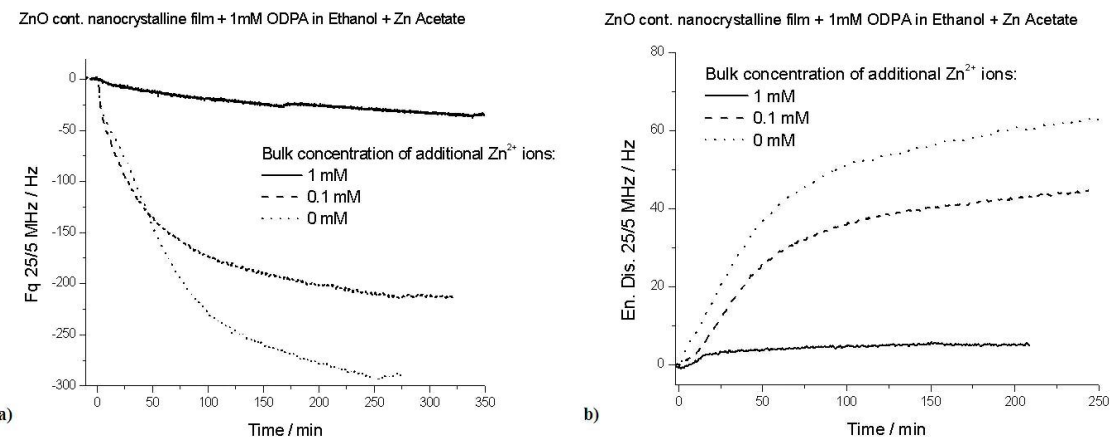
Figure 5.25: QCM data for adsorption process from 1 mM ethanolic solution of ODPA on ZnO continuous nanocrystalline film, with additional amount of Zinc Acetate a) Δf, b) $\Delta\Gamma$.

with Zinc Acetate addition in : 1, 0.1 and 0 mM concentration in ethanol. Shifts of frequency and energy dissipation were very small in the system with higher (1 mM) amount of Zinc Acetate: Δf= -36 Hz, $\Delta\Gamma$=5 Hz, whereas for the suspension with salt concentration of 0.1 mM shifts of: Δf= -215 Hz, $\Delta\Gamma$ =44 Hz were reached. The experiment with smaller load of additional zinc ions had a response, resemble to the system with pure ODPA ethanolic solution (Δf= -290 Hz, $\Delta\Gamma$= 58 Hz). The obtained results gave an indication of bulk zinc ion influence on interface phenomena. High Zinc Acetate concentration seemed to hinder phosphonic acid adsorption on ZnO nanocrystalline films.

The FT-IR (figure 5.27) and FE-SEM (figure. 5.26) data support conclusions from adsorption experiments. Significant change in adsorbate coverage is observable within the two systems inclusing 1 and 0.1 mM addition of zinc ions into ODPA solution.

The surface topography was not visibly affected in the case of the sample treated with ODPA ethanolic solution with 1mM Zinc Acetate (figure 5.26a). Ten times smaller concentration of additional zinc ions led to significant surface structure modification (figure 5.26b). Similar coverage was seen in the case of the sample in contact
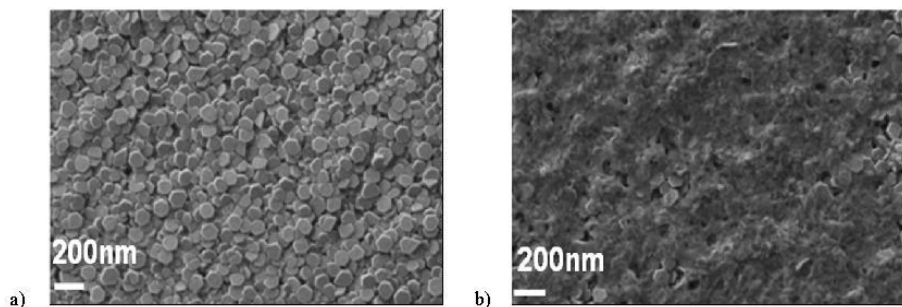
Figure 5.26: FE-SEM images of quartz crystal sensors with ZnO continuous film and after QCM experiments with 1 mM ethanolic solution of ODPA and Zinc Acetate (a)1mM ZnAc, b) 0.1mM ZnAc).

with pure ethanolic alkylphosphonic acid solution (figure 5.23).

The presence of alkyl chains on both surfaces was detected by means of FT-IR spectroscopy (figure 5.27, as-prepared ZnO nanocrystalline continuous films were used as reference). Peaks observed at around 2916 and 2847 cm^{-}1 could be attributed to asymmetric and symmetric -CH$_2$ vibrations, respectively. Band at 2958 cm^{-}1 is assigned to asymmetric -CH$_3$ vibrations. Complex structure of precipitation films and ZnO crystals prevent verification of alkyl chains self assembly, but peaks intensities support QCM and FE-SEM data, suggesting higher adsorbate coverage in the case of the sample with smaller addition amount of zinc ions. WCA of both samples surfaces reached 120° (pure substrate has WCA of 63°).

Furthermore, a drop of each ODPA combined with Zinc Acetate suspension was put onto mica stripped gold surfaces and was dried with nitrogen in order to examin bulk medium state of the experiments. FE-SEM images of those samples are shown in the figure 5.28.

The FE-SEM images of the dried drops on gold surfaces revealed (figure 5.28) similar structure of formed agglomerates to precipitation films seen on previous images of modified quartz crystals after QCM experiments (Fig. 5.23, 5.26b). The drop of suspension with 1mM concentration of ZnAc contained larger aggregates in comparision the one including zinc salt in the amount of 0.1 mM. These data sug-
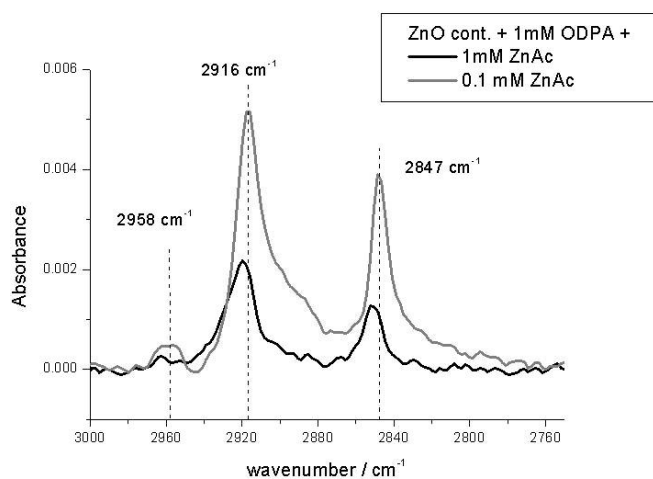
Figure 5.27: FT-IR spectra of quartz crystal sensors with ZnO continuous film after QCM experiment, modified 1 mM ethanolic solution of ODPA with Zinc Acetate.
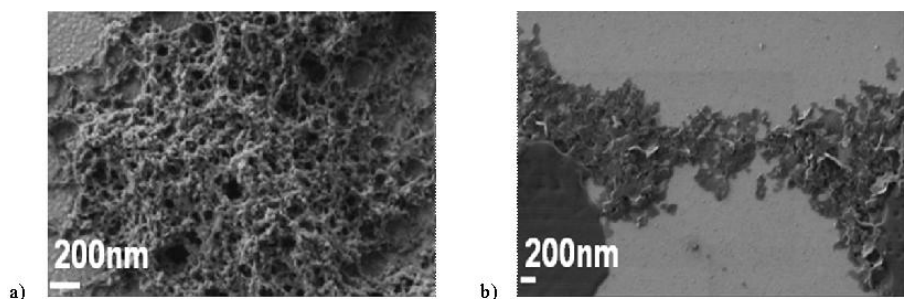
Figure 5.28: FE-SEM images of mica stripped gold surfaces with dried drops of 1 mM ethanolic solution of ODPA and Zinc Acetate: a)1mM, b)0.1mM.

gested that formation of precipitation films (observed on ZnO nanocrystalline films after interaction with alkyl phosphonic acid solution) was the result of complexation reaction between zinc ions (dissoluted from the substrate) with alkylphosphonic acid species.

The presence of additional Zn^{2+} appeared to be crucial for the adsorption process of alkylphosphonic acid on ZnO continuous nanocrystalline films. Along the QCM experiments with implementation of zinc salt, ODPA molecules formed complexes with Zn^{2+} ions in the bulk liquid environment (figure 5.28). This phenomenon seemed to inhibit surface reactions when the amount of Zn^{2+} was high enough

(figure 5.26). Decreased shifts of frequency and energy dissipation parameters occurred along the QCM experiments when the extent of additional metal ions was 1mM in comparison to 0.1 mM concetration as well as pure ethanolic system (figure 5.25).

5.4.3 Conclusions

Based on experimental data a following reaction mechanism was suggested: Alkylphosphonic acid molecules promoted Zn^{2+} dissolution at the liquid/metal oxide interface, mostly from the less stable polar ZnO (0001) orientation, when brought into contact with the ZnO crystals. The QCM, FE-SEM, FT-IR results gave indication that metal ions interacted with phosphonic acid functional groups and were brought back to the surface as a complex, forming an adsorbate layer on partially dissolved ZnO crystals. This interfacial phenomenon seemed to be hindered by introducing large amount of additional Zn^{2+} ions into the system. These ions binded organic molecules in the bulk and therefore prevented substrate dissolution and excess adsorbate deposition at the interface.

ZnO continuous films with larger exposed (0001) planes appeared to be more sensitive to organic phosphonic acid in comparison to nanorod films, where favourable non polar phase had larger surface area.

These results help to understand the mechanism of akylphosphonic acid adsorption on ZnO nanocrystalline surfaces. Comprehension of this phenomenon is crucial for functionalization of such surfaces, giving them even wider spectrum of possible applications.

Chapter 6

Overall Conclusions and Outlook

QCM experiments gave opportunity to better understand fundamental surface phenomena, critical for future application and performance of the used materials. The device provided deeper comprehension of surface reactions mechanisms along in-situ adsorption processes. The results were evaluated as a function of bulk experimental parameters like e.g. pH or solvent polarity. QCM data were additionally supported by FT-IR spectroscopy, FE-SEM surface images and Water Contact Angle measurements.

Unusual QCM response to adsorption of rather large colloid agglomerates in liquid helped to explain surface behaviour of those species, even though the fundamental rule for the device did not hold. A comparison of frequencies shifts and energy dissipation parameter on different overtones revealed a coupled resonance between colloids and quartz crystal. Therefore, QCM most likely probed the contact strength, instead of the particle mass, when adsorbate agglomerates were larger than 1 μm.

The used colloids were made of mesoporous TiO_2 covered with polyelectrolyte multilayers for the future application as nanocontainers (NCs) in self-healing coatings. Further QCM experiments were performed at various experimental conditions on SAM modified gold substrates. It was clearly demonstrated that the polyelectrolyte cover layer had a major impact on the surface charge of the NCs, state of

agglomeration and their adsorption kinetics. Desirable particle distribution could be controlled by adjustment of ionic strength, pH and zeta potential of NCs suspensions. Combination of these data with ex-situ FE-SEM crystal images delivered a "recipe" for proper NCs coverage. The proposed mechanism could also be supported by means of DLVO theory. PAH covered NCs strongly adsorbed on carboxythiol monolayer at the pH of 9 when solution ionic strength was rather high (10 mM), whereas adsorption did not take place at I= 1 mM or less. This effect of salt concentration on deposition process was explained in terms of electrical double layer thickness: when the ionic strength increased, the Debye length became smaller. Thus, the particle could approach the surface close enough that attractive van der Waals forces predominated and deposition took place. Such interactions were calculated for pH of 9, as PAH terminated particles had a strong negative charge in those conditions. The same system was not that sensitive to salt at the pH of 6, where particles had weaker zeta potential. These studies promote further investigation in the scope of nanoconainer application as inhibitor nanoreservoirs in self-healing coatings. Incorporation and release control of active substance (corrosion inhibitor) from NC pores is one of the most challenging aspects of these layers effectiveness.

In last part of the work, surface functionalization via alkylphosphonic acid was analysed on ZnO nanocrystalline films with various molecular alkyl chain lengths and crystal morphologies (continuous and nanorod crystalline films). Set of experiments as a function of metal ions content and solvent polarity helped to formulate a possible phosphonic acid deposition mechanism on such substrates. It was observed that the phosphonic acid group appeared to initiate partial dissolution of ZnO crystals. Addition of Zn^{2+} ions into bulk solution seemed to inhibit the process and monolayer with possibly better quality (self-organisation) could be formed. QCM data suggested that solvent polarity had an impact of molecular coverage on nanocrystalline films. It could be concluded that the lower solvent polarity provided appropriate environment for self-organisation of hydrophobic alkyl chains along deposition on polar ZnO nanocrystalline films. Experiments with mono-functional

alkylphosphonic acid molecules were performed as the first step to understand ZnO nanocrystals functionalization process via phosphonic acid group. Further measurements are necessary to verify the impact of the second polar group in bi-functional molecule on adsorption kinetics and self-organisation.

124

Bibliography

[1] D. G. Shchukin, H. Moehwald, Adv. Funct. Mater. 2007, **17**, 14511458

[2] D. G. Shchukin and H. Moewald, Small, 2007, **3**, 926.

[3] G. Grundmeier, M. Stratmann, Annual Reviews Materials Research, 2005,**35**, 571

[4] K. Wapner, G. Grundmeier, Advanced Engineering Materials, 2004, **6**, 163

[5] M. Maxisch, P. Thissen, M. Giza and G. Grundmeier, Langmuir 2011,**27**, 60426048

[6] X. Luo, A. Morrin, A.J. Killard, M.R. Smyth, Electroanalysis, 2006, **18**, 319326.

[7] J.M. Pingarron, P.Y. Sedeno, A.G. Cortes, Electrochimica Acta, 2008, **53**, 58485866.

[8] S. Prakash et al., Biosensors and Bioelectronics, 2013, **41**, 4353.

[9] C. Ankerfors, E. Jaohansson, T. Petterson and L. Wgberg, Col. and Int. Sc., 2013, **391**, 2835.

[10] M. Brynda, P. Chodakowski and S. Stoll, Colloid Polym Sci, 2002, **280**, 789797.

[11] P. I. Reyes, Zheng Zhang, Hanhong Chen, Ziqing Duan, Jian Zhong, G. Saraf, Lu Yicheng, O. Taratula, E. Galoppini, and N. N Boustany, IEEE Sensors Journal, 2009, **9**, 1302.

[12] O. Ozcan, PhD dissertation: *Sythesis, characterisation and Functionalization of ZnO Nanorods on Metals*, Rühr Universität Bochum , 2010.

[13] O. Ozcan, K. Pohl, G. Grundmeier, Electrochem. Commun., 2011, **13**, 8, 837-839.

[14] J. Joo, D. Lee and S. Jeon, Sensors and Actuators B, 2009, **138**, 485490.

[15] L. Vayssieres, Adv. Mater., 2003, **15**, 464.

[16] B. Zhang, T. Kong, W. Xu, R. Su, Y. Gao, and G. Cheng, Langmuir, 2010, **26**, 4514.

[17] D. A. Buttry et al., Chem. Rev., 1992, **92**, 1355.

[18] G. Sauerbrey, Z. Phys. 1959, **155**, 206.

[19] K. A. Melzak et al., Soft Matter, 2011, **7**, 332.

[20] S. Bhagavantam and D. Suryanarayana, Proc. Math. Scien., 1945, **21**, 19.

[21] D. Johannsmann, *Modeling of QCM Data - QTZ software*, Handbook, TU Clausthal, Germany.

[22] D. Johannsmann, Phys. Chem. Chem. Phys., 2008, **10**, 4516.

[23] A. Pomorska, D. Shchukin, R. Hammond, M. Cooper, G. Grundmeier, and D. Johannsmann, Anal. Chem., 2010, **82**, 2237-2242.

[24] D. D. Vogt et al., J. Phys. Chem. B, 2004, **108**, 12685.

[25] K. K. Kanazawa and J. G. Gordon II, Anal. Chem. Acta, 1985, **99**, 175.

[26] J. M. McDonnell, Curr. Opin. Chem. Biol. 2001, **5**, 572.

[27] W. Welsch et al., Anal. Chem. 1996, **68**, 2000.

[28] W. J. Dybwad, Appl. Phys. 1985, **58**, 2789.

[29] A. Laschitsch et al., J. Appl. Phys. 1999, **85**, 3759.

[30] S. Berg et al., Phys. Rev. Lett. 2003, **91**, 145505.

[31] D. Amour et al., D. Phys. Rev. Lett. 2006, **96**, 058301.

[32] H. C. Hamaker, Physica, 1937, **4**, 1058.

[33] D. Henderson et al., J. Colloid Interface Sci. 1997, **185**, 265.

[34] E. M. Lifshitz, Soviet Phys. JETP (Engl. Transl.) 1956, **2**, 73.

[35] I. E. Dzyaloshinskii et al., Adv. Phys. 1961, **10**, 165.

[36] J. Mahanty, B. W. Ninham, *Dispersion Forces*, Academic Press, New York, 1976.

[37] J. N. Israelachvili, Quart. Rev. Biophys. 1974, **6**, 341.

[38] R. Guidelli, W. Schmicler, Electrochimica Acta, 2000, **45**, 2317.

[39] H.-J. Butt, M. Kappl, and K. H. Graf, *Physics and Chemistry of Interfaces*, Wiley-VCH, 2006.

[40] B. V. Derjaguin and L. Landau, Acta Physicochim. URSS, 1941, **14**, 633.

[41] E. J. W. Verwey, J. Th. G. Overbeek, *Theory of the Stability of Lyophobic Colloids*, Elsevier, Amsterdam, 1948.

[42] J. Goodwin, *Colloids and Interfaces with Surfactants and Polymers*, Wiley & Sons, 2009.

[43] I. K. Snook et al., Phys. Letters, 1979, **74A**, 5.

[44] W. v. Megen and I. Snook, J. Chem. Soc. Faraday Trans. II, 1979, **7**, 1095.

[45] M. J. Stevens et al., Chem. Phys., 1995, **103**, 1669.

[46] S. Clark et al., Langmuir, 2000, **16**, 10206.

[47] A. Laguecir et al., European Polymer Journal, 2006, **42**, 1135.

[48] G. Decher et al., Makromol. Chem. Macromol. Symp. 1991, **46**, 321.

[49] S. S. Shiratori et al., Macromolecules 2002, **33**, 4213.

[50] J. D. Mendelsohn et al., Langmuir, 2000, **16**, 5017.

[51] H. Möhwald, J. Col. Surf. A: Physicochem. Eng. Aspects, 2000, **171**, 25.

[52] G. B. Sukhorukov et al., Polym. Adv. Technol, 1998, **9**, 759.

[53] D. G. Shchukin, M. Zheludkevich, K. Yasakau, S. Lamaka, M. G. S. Ferreirand, and H. Moewald, Adv. Mater., 2006, **18**, 1672.

[54] R. J. Hunter, *Foundations of Colloid Science*, Clarendon Press, Oxford, 1997.

[55] G. Dacher and J. B. Schlenoff (editors), *Multilayer Thin Films*, 2nd ed., Wiley-VCH, 2012.

[56] J. B. Schlenoff and S. T. Dubas, Macromolecules, 2001, **34**, 592.

[57] H. Dautzenberg and B. Philipp, *Polyelectrolytes: Formation, Characterization and Application*, Hanser, Munich, 1994.

[58] T. Radeva, *Physical Chemistry of Polyelectrolytes*, Marcel Dekker, New York, 2001.

[59] H. J. Bixler et al., *Encyclopedia of Polymer Science and Technology, Interscience*, Vol.10, p. 765, New York, 1969.

[60] E. Tsuchida et al., Makromol. Chem., 1974, **175**, 593.

[61] J. B. Schlenoff et al., J. Am. Chem. Soc., 1998, **120**, 7626.

[62] S. T. Dubas et al., Macromolecules, 1999, **32**, 8153.

[63] T. Farhat et al., Langmuir, 2001, **17**, 1184.

[64] J. B. Schlenoff et al., Langmuir, 2000, **16**, 9968.

[65] S. S. Shiratori et al., Macromolecules, 2000, **33**, 4213.

[66] E. Donath et al., Angew. Chem. Int. Ed., 1998, **37**, 2202.

[67] J. C. Love et al., Chem. Rev., 2005, **105**, 1103.

[68] W. P. Wuelfing et al. Anal. Chem., 1999, **71**, 4069.

[69] J. N. Israelachvili, *Intermolecular and Surface Forces*, 2nd ed., Academic Press, New York, 1992.

[70] R. H. Terrill et al., J. Am. Chem. Soc., 1995, **117**, 12537.

[71] M. J. Hostetler et al., Langmuir 1996, **12**, 3604.

[72] T. P. Ang et al., J. Phys. Chem. B, 2004, **108**, 11001.

[73] B. S. Zelakiewicz et al. J. Am. Chem. Soc., 2004, **126**, 10053.

[74] W. D. Luedtke et al., J. Phys. Chem. B, 1998, **102**, 6566.

[75] M. J. Hostetler et al., Langmuir, 1998, **14**, 17.

[76] E. Abdullayev et al., App. Mat. Int. Vol. 1, 2009, **7**, 1437.

[77] M. Garcia-Heras, A. Jimenez-Morales, B. Casal, J. C. Galvan, S. Radzki, and M. A. Villegas, J. Alloys Compd., 2004, **380**, 219.

[78] L. S. Kasten et al., Surf. Coat. Technol.,2001, **140**, 11.

[79] Y. M. Lvov et al., Chem. Commun., 1998, 1229.

[80] G. L. Gaines, *Insoluble Monolayers at Liquid-Gas Interfaces*, Interscience Publishers, New York, 1966.

130

[81] A. W. Adamson and A. P. Gast, *Physical Chemistry of Surfaces*, 6th ed., Wiley-Interscience, New York, 1997.

[82] J. Bao, A. V. Bragas, J. K. Furdyna, and R. Merlin, Nat. Mater., 2003, **2**, 175.

[83] A. N. Cleland, J. S. Aldridge, D. C. Driscoll, and A. C. Gossard, Appl. Phys. Lett., 2002, **81**, 1699.

[84] M. N. Leuenberger and D. Loss, Nature (London), 2001, **410**, 789.

[85] M. Bayer, P. Hawrylak, K. Hinzer, S. Fafard, M. Korkusinski, Z. R. Wasilewski, O. Stern, and A. Forchel, Science (Washington, D. C.), 2001, **291**, 451.

[86] L. H. Dubois et al., J. Chem. Phys. **98**, 678.

[87] D. S. Karpovich and G. J. Blanchard, Langmuir, 1994, **10**, 3315.

[88] R. G. Nuzzo et al., J. Am. Chem. Soc., 1987, **109**, 733.

[89] S. Xu et al., J. Chem. Phys. 1998, **108**, 12, 5002.

[90] A. Ulman, Chem. Rev. 1996, **96**, 1533.

[91] E. S. Gewalt et al., Langmuir, 2001, **17**, 5736.

[92] M. S. Lim et al., Langmuir, 2007, **23**, 2444.

[93] N. Tilman, J. Am. Chem. Soc., 1988, **110**, 6136.

[94] J. P. Bareman et al., J. Phys. Chem., 1990, **94**, 5202.

[95] T. Ishida et al., Langmuir, 2001, **17**, 7459.

[96] M. Kawasaki et al., Langmuir, 2000, **16**, 1719.

[97] R. Berger et al., Science, 1997, **276**, 2021.

[98] H.-J. Butt, J. Colloid Interface Sci., 1996, **180**, 251.

[99] M. Godin et al., Langmuir, 2004, **20**, 7090.

[100] R. Desikan et al., Ultramicroscopy, 2006, **106**, 795.

[101] M. Sepaniak et al., Anal. Chem. 2002, **74**, 568A.

[102] G. Zuo and X. Li, Nanotechnology, 2011, **22**, 045501.

[103] G. Poirier, Chem. Rev., 1997, **97**, 1117.

[104] D. Schwartz, Annu. Rev. Phys. Chem., 2001, **52**, 107.

[105] H. Groenbeck et al., J. Am. Chem. Soc., 2000, **122**, 3839.

[106] H. Ibach et al., J. Vac. Sci. Technol. A, 1994, **12**, 2240.

[107] M. C. Vargas et al., Rev. Mex. Fis., 2004, **50**, 536.

[108] A. K. Rapp'e et al, J. Am. Chem. Soc., 1992, **114**, 10024.

[109] M. Godin, *Surface stress, kinetics, and structure of alkanethiol self-assembled monolayers*, PhD Dissertation, McGill University, 2004, Canada.

[110] O. Dannenberger et al., Thin Solid Films, 1997, **307**, 183.

[111] R Desikan et al., Nanotechnology, 2007, **18**, 424028.

[112] R. Arnold et al., Langmuir, 2002, **18**, 3991.

[113] H. Wang, S. F. Chen, and L. Y. Li, Langmuir, 2005, **21**, 2633.

[114] M. Wallwork et al., Langmuir, 2001, **17**, 1126.

[115] T.M. Parker, N. G. Condon et al., Surf. Sci.1998,**415**, L1046-L1050.

[116] K. Govender, D. S. Boyle et al., J. Mater. Chem. 2004,**14**, 2575-2591.

[117] L. E. Greene et al., Nano Lett. 2005,**5**,7, 1231-1236.

132

[118] [K.W. Chae, Beilstein J. Nanotechnol. 2010, 1, 128134.]

[119] E. V. Skorb, D. Sviridov, H. Möhwald, D. G. Shchukin, Chem. Commun., 2009, **40**, 6041.

[120] G. Decher, Science, 1997, **277**, 1232.

[121] C. N. Banwell, *Fundamentals of molecular spectroscopy*, 3rd Edition, McGraw-Hill, 1983.

[122] H. Jaksch, J-P Vermeulen, *New developments in FESEM Technology*, Carl Zeiss SMT, Oberkochen, Germany (http://www.zeiss.de).

[123] R. Hogg, T. W. Healy, D. W. Fuerstenau, Trans. Faraday Soc. 1966, **62**, 1638.

[124] H.-J. Butt, K. Graf, M. Kappl, *Physics and Chemistry of Interfaces*, Wiley-VCH Verlag, Weinheim, Germany, 2003 (Chapter 6).

[125] P. Ghosh, *Colloid and Interface Science*, Phi Ltd, India, 2009 (Chapter 5).

[126] S. Bhattacharjee, M. Elimelech, J. Colloid Interface Sci. 1997, **193**, 273.

[127] E. Martines, L. Csaderova, H. Morgan, A. S. G. Curtis, M. O. Riehle, Colloids Surf., 2008, **A318**, 45.

[128] D. J. Voorn, W. Ming, J. Laven, J. Meuldijk, G. de With, A. M. van Herk, Colloids Surf., 2007, **A294**, 236.

[129] J. Fatisson, R. F. Domingos, K. J. Wilkinson, N. Tufenkji, Langmuir, 2009, **25**, 6062.

[130] H. Yildirim Erbil, *Surface chemistry of solid and liquid interfaces*, Oxford University Press, 2006, p. 250.

[131] K. Kontturi, L. Murtomäki, J. A. Manzanares, *Ionic Transport Processes in Electrochemistry and Membrane Science*, Oxford University Press, 2008, p. 162.

[132] W. Fritzsche and T. Taton, Nanotechnology, 2003, **14**, R63.

[133] V. Sauvant-Moynot, S. Gonzalez, and J. Kittel, Progress in Org. Coat., 2008, **63**, 307.

[134] D. V. Andreeva, and D. G. Shchukin, Materials Today, 2008, **11**(10), 24.

[135] M. L. Zheludkevich, D. G. Shchukin, K. A. Yasakau, H. Moewald, and M. G. S. Ferreira, Chem. Mater., 2007, **19**, 402.

[136] N. N. Voevodin, N. T. Grebasch, W. S. Soto, F. E. Arnold, and M. S. Donley, Surf. Coat. Technol., 2001, **140**, 24.

[137] V. Palanivel, Y. Huang, and W. J. van Ooij, Prog. Org. Coat., 2005, **53**, 153.

[138] D. G. Shchukin, D. O. Grigoriev, and H. Moewald, Soft. Matter, 2010, **6**, 720.

[139] D. V. Andreeva, E. V. Skorb, and D. G. Shchukin, Applied Mat. and Interf., 2010, **2**, 1954.

[140] V. Kozlovskaya, E. Kharlampieva, M. L. Mansfield, and S. A. Sukhishvili, Chem. Mater., 2006, **18**, 328.

[141] P. Thissen, M. Valtiner, and G. Grundmeier, Langmuir, 2010, **26**, 156.

[142] K. S. Toohey, C. J. Hansen, J. A. Lewis, S. R. White, and N. R. Sottos, Adv. Funct. Mater., 2009, **19**, 1399.

[143] C. J. Hansen, W. Wu, K. S. Toohey, N. R. Sottos, S. R. White, and J. A. Lewis, Adv. Mater., 2009, **21**, 4143.

[144] Y. Yoo, D.-C. Kim, and T.-Y. Kim, J. Appl. Polym. Sci., 1999, **74**, 2856.

[145] J-S. Jan, S. Lee, C. S. Carr, and D. F. Shantz, Chem. Mater., 2005, **17**, 4310.

[146] [17] A. M. Collins, C. Spickermann, and S. Mann, J. Mater. Chem., 2003, **13**, 1112.

134

[147] J. M. Campiña, A. Martins, and F. Silva, J. Phys. Chem. C, 2007, **111**, 5351.

[148] T. H. Degefa, P. Schön, D. Bongard, and L. Walder, J. Electroanal. Chem., 2004, **574**, 49.

[149] R. Schweiss, D. Pleul, F. Simon, A. Janke, P. B. Welzel, B. Voit, W. Knoll, and C. Werner, J. Phys. Chem. B, 2004, **108**, 2910.

[150] J. Choi and M. F. Rubner, Macromolecules, 2005, **38**, 116.

[151] J. Muller, G. Schope, O. Kluth et al.,Thin Solid Films 2003, **442**, 158-162.

[152] M. Huang, Y. Wu, H. Feick, N. Tran, E. Weber, P. Yang, Advanced Materials 2001, **13**, 113-116.

[153] M. Law, L. Greene, J. Johnson, R. Saykally, P. Yang, Nature Materials 2005, **4**, 455-459.

[154] J. Wu, C. Tseng, Applied Catalysis B-Environmental 2006, **66**, 51-57.

[155] X. Zhou et al., Sensors and Actuators A, 2007, **135**, 209.

[156] T. Gao, T. Wang, Applied Physics a-Materials Science & Processing 2005, **80**, 1451-1454.

[157] J. Wang, X. Sun, Y. Yang, H. Huang, Y. Lee, O. Tan, L. Vayssieres, Nanotechnology 2006, **17**, 4995-4998.

[158] F. Zhang et al., Analytica Chimica Acta 2004, **519**, 155-160.

[159] Y. Masuda, N. Kinoshita, K. Koumoto, Electrochimica Acta 2007, **53**, (1), 171-174.

[160] L. Vayssieres, K. Keis, S. Lindquist, A. Hagfeldt, Journal of Physical Chemistry B 2001, **105**, 3350-3352.

[161] L. Greene, M. Law, J. Goldberger, F. Kim, J. Johnson, Y. Zhang, et al. Angewandte Chemie-International Edition 2003, **42**, 3031-3034.

[162] L. Greene, M. Law, D. Tan et al., Nano Letters 2005, **5**, 1231-1236.

[163] Y. Cao, Langmuir, 2012, **28**, 7947.

[164] S. A. Morin, F. F. Amos, and S. Jin, J. Am. Chem. Soc., 2007, **129**, 13776.

[165] Z. Zhang et al., Conference Publication: *International Frequency Control Symposium and Exposition*, 2006 IEEE, 545.

[166] T. Kong, Y. Chen, Y. Ye, K. Zhang, Z. Wang, X. Wang, Sensors and Actuators B-Chemical 2009, **138**, 344-350.

[167] A. Wei, X. Sun, J. Wang, Y. Lei, X. Cai, C. Li, Z. Dong, W. Huang, Applied Physics Letters 2006, **89**, (12).

[168] T. Liu, H. Liao, C. Lin, S. Hu, S. Chen, Langmuir 2006,**22**,5804-5809.

[169] Z. Zhao, W. Lei, X. Zhang, B. Wang, H. Jiang, Sensors 2010, **10**, 1216-1231.

[170] O. Taratula, E. Galoppini, D. Wang, D. Chu, Z. Zhang, H. H. Chen, G. Saraf, and Y. C. Lu, J. Phys. Chem. B, 2006, **110**, 6506.

[171] C. Perkins, Journal of Physical Chemistry C 2009, **113**, 18276-18286.

[172] M. Voigt, M. Klaumunzer et al., Journal of Physical Chemistry C 2011, **115**, 5561-5565.

[173] N. Adden, L. Gamble, D. Castner, A. Hoffmann, G. Gross, H. Menzel, Langmuir 2006, **22**, 8197-8204.

[174] S. Koh, K. McDonald, D. Holt, C. Dulcey, J. Chaney, P. Pehrsson, Langmuir 2006, **22**22, 6249-6255.

136

[175] K. Fukuda, T. Hamamoto, T. Yokota, T. Sekitani, U. Zschieschang, H. Klauk, and T Someya, Appl. Phys. Lett., 2009, **95**, 203301.

[176] N. Lee, H. Kang, E. Ito, M. Hara, J. Noh, J., Bulletin of the Korean Chemical Society 2010, **31**, 2137.

[177] D. Schwartz, Annual Review of Physical Chemistry 2001, **52**, 107-137.

[178] Y. Kim, R. McCarley, A. Bard, Langmuir 1993, **9**,1941-1944.

[179] M. Giza, P. Thissen, G. Grundmeier, Langmuir 2008, **24**, 8688-8694.

[180] H.-Y. Nie et al. J. Phys. Chem. B, 2006, **110**, 21101.

[181] A. K. Amirjahed et al., J. Pharm. Scien., 1974/81, **63**, 81.

[182] X. Song et al., J. Col. Interf. Scien., 2003, **304**, 37.

[183] C. D. Bain, E. B. Troughton, Y.-T. Tao, J. Evall, and G. M. Whitesides, J. Am. Chem. Soc., 1989, **111**, 321.

[184] J. Dai, Z. Li, J. Jin, J. Cheng, J. Kong, S. Bi, Journal of Electroanalytical Chemistry 2008, **624**, (1-2), 315-322.

[185] J. Dai, J. Cheng, J. Jin, Z. Li, J. Kong, S. Bi, Electrochemistry Communications 2008, **10**, 587-591.

[186] T. Hauffman, O. Blajiev et al., Langmuir 2008, **24**, 13450-13456.

[187] X. Chen et al.,Langmuir, 2012, **28**, 9487.

[188] H.-Y. Nie et al., Langmuir, 2002, **18**, 2955.

[189] E. L. Hanson et al., J. Am. Chem. Soc., 2003, **125**, 16074.

[190] B. Cao and W. Cai, J. Phys. Chem. C 2008, **112**, 680-685.

[191] Z. R. Tian, J. A. Voigt et al., Nat. Mater. 2003, **2**, 821-826.

[192] A. Pomorska, K. Yliniemi, B. P. Wilson, D. Shchukin, D. Johannsmann, and G. Grundmeier, J. Col. Int. Sc., 2011, **362**, 180-187.

[193] Z. Feldötö et al., Langmuir, 2010, **26**, 17048.

[194] H. O. Jenkins and J. F. J. Dippy, J. Am. Chem. Soc., 1940, **62**, 483-484.

[195] A. Kousuke et al., Analytical Science, 1999, **15**, 651.

[196] E. M. Wong et al. Langmuir, 2001, **17**, 8362.

List of Acronyms

AUT - 11-Amino-1-undecanethiol hydrochloride

APPA - Aminopropylphosphonic Acid

DLVO - Particle Adsorption theory established by B.V. Derjaguin, L. Landau, E.L.W. Verwey, J.Th.G. Overbeek

EDL - Electric Double Layer

FE-SEM - Field Emission Scanning Electron Microscopy

FT-IR - Fourier Transform Infra-Red Spectroscopy

HBHW - Half-Band-Half-Width (QCM parameter related to Energy Dissipation)

LbL - Layer by Layer Technique

MUA - 15-mercaptopentadecanoic acid

NC - Nanocontainers

NR - ZnO nanorods

ODPA - Octadecylphosphonic Acid

PAA - Poly(acrylic) acid

PAH - Poly(allylamine) hydrochloride

PM-IRRAS - Polarisation Modulated Infra-Red Reflection Absorption Spectroscopy

PSS - Polysodium 4-styrenesulfonat

SAM - Self-Assembled Monolayer

QCM - Quartz Crystal Microbalance

UV - Ultra-Violet

WCA - Water Contact Angle

List of Figures

146

List of Tables

Curriculum Vitae of Agata Pomorska

Personal data:

Date and Place of Birth: February 10$^{\text{th}}$, 1984, Lublin, Poland

Citizenship: Polish

Marital Status: single

Professional Address:

University of Paderborn

Warburger Str. 100

33098 Paderborn, Germany

Phone: +49 5251-60-5746

Fax: +49 5251-60-3244

Email: pomorska@tc.upb.de

http://chemie.uni-paderborn.de/fachgebiete/tc/ak-grundmeier/mitarbeiter/agata-weronika-pomorska/

Education:

May 2013   PhD thesis *Studies of the adsorption of organic acids and nanoparticles on modified metal surfaces by means of QCM technique* written under supervision of Professor Dr. -Ing. Guido Grundmeier. Expected degree: Doctor rer. nat.

2008-2013   Postgraduate studies at the Faculty of Science, University of Paderborn, Germany,

2008   Graduate diploma *Master of Science in Chemistry* at the Maria Curie Skłodowska University, Faculty of Chemistry, Master Thesis title: *Study of surface properties of starch films by means of AFM and contact angle measurements*, under supervision of Professor Bronisław Jańczuk,

2003-2008   Chemistry studies with major in Physical Chemistry at the Maria Curie Skłodowska University in Lublin, Poland,

2003   Secondary School Graduation Diploma,

1999-2003   Jan III Sobieski Secondary School in Lublin, Poland,

1991-1999   Adam Mieckiewicz Primary School, in Lublin, Poland,

1990-1991   Camille Hirtz Primary School in Strasbourg, France.

Publications:

1. **QCM Study of the Adsorption of Polyelectrolyte Covered Mesoporous TiO$_2$ Nanocontainers on SAM Modified Au Surfaces**, A. Pomorska, K. Yliniemi, B.P. Wilson, D. Shchukin, D. Johannsmann, and G. Grundmeier, *Journal of Colloid and Interface Science*, **362**, 1, 180-187 (2011)

2. **Positive Frequency Shifts Observed Upon Adsorbing Micron-Sized Solid Objects to a Quartz Crystal Microbalance from the Liquid Phase**, A. Pomorska, D. Shchukin, R. Hammond, M. Cooper, G. Grundmeier, and D. Johannsmann, *Analytical Chemistry*, **82**, 2237-2242 (2010)

Conference contributions:

1. A. Pomorska, O. Ozcan, and G. Grundmeier, POSTER: **Study of SAM adsorption on ZnO nanocrystalline films as a function of crystal growth geometry by means of QCM and FT-IR Spectroscopy**, *Materials Research Society Fall Meeting 2012*, Boston, MA, USA, November 26, 2012.

2. A. Pomorska, O. Ozcan, and G. Grundmeier, ORAL PRESENTATION: **Investigation of Adsorption Process of Thiol Self-Assembled Monolayers on Gold via Monitoring Energy Dissipation Shifts by Means of Quartz Crystal Microbalance**, *Materials Research Society Fall Meeting 2011*, Boston, MA, USA, November 30, 2011.

3. A. Pomorska, B. Wilson, K. Yliniemi, D. Shchukin, D. Johannsmann, and G. Grundmeier, POSTER: **In-Situ Adsorption Study of Nanocontainers on SAM Modified Metal Surfaces at various values of pH and Ionic Strength Values by Means of QCM**, *2nd International Symposium on Functional Surfaces*, Aachen, DE, September 14-15, 2011.

4. A. Pomorska, B. Wilson, K. Yliniemi, D. Shchukin, D. Johannsmann,and G. Grundmeier, ORAL PRESENTATION: **In-Situ Adsorption Study of**

Nanocontainers on SAM Modified Metal Surfaces at various values of pH and Ionic Strength Values by Means of QCM, *7th Zsigmondy Colloquium*, Münster, Germany, Februar 22, 2011.

5. A. Pomorska, B. Wilson, K. Yliniemi, D. Shchukin, D. Johannsmann, and G. Grundmeier, ORAL PRESENTATION: **In-Situ Adsorption Study of Polyelectrolyte Covered Mesoporous TiO$_2$ Nanocontainers on SAM Modified Metal Surfaces by Means of QCM**, *Materials Research Society Fall Meeting 2010*, Boston, MA, USA, November 28, 2010.

6. A. Pomorska, W. Wijting, I. Dönch, D. Johannsmann, D. Shchukin, and G. Grundmeier, POSTER (Award): **QCM Study of the Adsorption of Polyelectrolytecovered Mesoporus TiO$_2$ Nanocontainers on SAM modified Au-surfaces**, *6th Zsigmondy Colloquium*, Chemnitz, Germany, March 22-24, 2010.

7. O. Ozcan, B. Ozkaya, A. Pomorska, and G.Grundmeier, **Scanning Kelvin Probe Force Microscopy Investigations on Barrier Properties of Organic Films on Patterned Zinc Oxide Nanorod Films**, *Material Research Society Fall Meeting 2009*, Boston, MA, USA, November 29 to December 4, 2009.

8. A. Pomorska, V. Möllmann, W.K. Wijting, and G. Grundmeier, POSTER: **Defect Preparation and Patterning for the Fundamental Analysis of Self-Repair Processes**, *1st MUST Workshop on Advanced Concepts in Corrosion Protection for Light-weight Alloys and Steel Using Cr(VI)-free Nanostructured Hybrid Coatings*, Munich, Germany, January 21-22, 2009.